# POROSITY AND PERMEABILITY CHARACTERIZATION WITHIN THE LITHOFACIES FRAMEWORK OF A MIOCENE DAM FORMATION OUTCROP, EASTERN SAUDI ARABIA

BY

ABDALLAH ABDELKARIM HASSAN ABDELKARIM

A Thesis Presented to the
DEANSHIP OF GRADUATE STUDIES

**KING FAHD UNIVERSITY OF PETROLEUM & MINERALS**

DHAHRAN, SAUDI ARABIA

In Partial Fulfillment of the
Requirements for the Degree of

# MASTER OF SCIENCE

**In**

GEOLOGY

MAY 2015

KING FAHD UNIVERSITY OF PETROLEUM & MINERALS

DHAHRAN- 31261, SAUDI ARABIA

**DEANSHIP OF GRADUATE STUDIES**

This thesis, written by **Abdallah Abdelkarim** under the direction his thesis advisor and approved by his thesis committee, has been presented and accepted by the Dean of Graduate Studies, in partial fulfillment of the requirements for the degree of **MASTER OF SCIENCE IN GEOLOGY.**

Dr. Osman Abdullatif
(Advisor)

Dr. Abdulaziz Al-Shaibani
Department Chairman

Prof. Gabor Korvin
(Member)

Dr. Salam A. Zummo
Dean of Graduate Studies

Dr. Lamidi Babalola
(Member)

12/9/15
Date

2015

*To the wise, the sincere, my father*

*Abdelkarim H. Abdelkarim*

*"may Allah bestow his glorious mercy and blessings on him"*

*To my beloved mother and family*

# ACKNOWLEDGMENTS

All praises and glory is to Allah, the most beneficent, the most compassionate, and the most merciful for his glory blessings and guidance.

I would like to express my sincere gratitude to King Fahd University of Petroleum & Minerals (KFUPM) for providing me the opportunity to pursue my master program, and supporting me throughout the program. I would like also to express my appreciation to the thesis committee, the chairman, Dr. Osman Abdullatif, and the committee members, Prof. Gabor Korvin, and Dr. Lamidi Babalola for their appreciated supervision of this work. Thanks is also to Dr. Hassan Eltom and Dr. Michael Kaminski for their valued participations to this work. I would like to thank the chairman, faculty, and staff of the Earth Sciences Department. I also would like to extend my sincere appreciation to the Center for Petroleum & Minerals (CPM) in the Research Institute of the KFUPM for giving me the opportunity to conduct the experimental works there. Through the center director, Dr. Abdullah Sultan, thanks is extended to the staff of the CPM who helped me during this work. Thanks also to my colleagues and friends in the Earth Sciences Department and KFUPM.

Finally, I would like to express my deep gratitude to my parents and family for their infinite support and sincere prayers throughout this work, and all the way.

# TABLE OF CONTENT

# LIST OF TABLES

# LIST OF FIGURES

# ABSTRACT

**Full Name** : Abdallah Abdelkarim Hassan Abdelkarim

**Thesis Title** : Porosity and Permeability Characterization within the Lithofacies Framework of A Miocene Dam Formation Outcrop, Eastern Saudi Arabia

**Major Field** : Geology

**Date of Degree** : May, 2015

Modeling of reservoir geology and properties is a highly demanded topic nowadays, for better understanding of reservoir heterogeneity particularly in the inter-well spacing. Outcrop studies represent one of the main targets to fill the limitations of subsurface data. In this context, an outcrop of Miocene Dam Formation was targeted for sedimentology and petrophysical analyses. Dam Formation is a Middle Miocene Formation, which is composed of mixed carbonate-siliciclastic sediments. Stratigraphically, Dam Formation is overlain by Hofuf Formation and underlain by Hadroukh Formation. The purpose of this research is to characterize the porosity and permeability of selected lithofacies, within the overall lithofacies framework of an outcrop of the Miocene Dam Formation in Al-Nasbiyah Area, Eastern Saudi Arabia. The Methodology that have been adopted to fulfill this work includes: 1- conducting detailed sedimentology logging and petrography in order to investigate the lithofacies pattern of Dam Formation, 2- sampling of the selected lithofacies for porosity and permeability analyses, and later selecting some of these samples for XRD, SEM, and Micro CT-Scan 3- geostatistical modeling of lithofacies framework, porosity, and permeability. The lithofacies investigation revealed that Dam Formation is composed of mixed carbonate-siliciclastic deposits, of tidal flat environment, with dominance of carbonate deposits. The lithofacies selected for petrophysical investigation are, from bottom to top, skeletal oolitic grainstone, sandy fossiliferous packstone, burrowed wackestone, and stromatolite grainstone in the top of the succession. The porosity-permeability relationship exhibits poor correlation for these lithofacies. Regarding the geostatistical modeling, several realizations were generated for lithofacies, porosity, and permeability models. These models were validated qualitatively and quantitatively on the basis of comparison with input data and present day lithofacies

setting. These models showed small scale heterogeneity in porosity and permeability even within the same lithofacies, these heterogeneities can be attributed to depositional and diagenetic controls on reservoir quality. The study showed that such models can be used as a guide for better understanding of the depositional setting, stacking pattern, and moreover property characterization and distribution, which might be used for prediction purposes if available subsurface models could be used for validation of such inter-well models.

# ملخص الرسالة

**الاسم الكامل**: عبدالله عبدالكريم حسن عبدالكريم

**عنوان الرسالة:** دراسة خصائص المساميه والنفاذيه في إطار السحنات الرسوبيه لمتكشف تكوين الدام الميوسيني في المنطقه الشرقيه للملكه العربيه السعوديه

**التخصص:** جيولوجيا

**تاريخ الدرجة العلمية**: رجب 1436

نمذجة المكامن الجيولوجيه و خصائصها تعتبر من المواضيع المهمه اليوم، نسبة لأهميتها في إثراء المعرفه والفهم فيما يخص عدم تجانس خصائص وجيولوجيا المكامن، بالأخص في نطاقات ما بين الآبار. دراسة المتكشفات الصخريه الجيولوجيه تعتبر من اهم الدراسات لتفادي محدوديه المعلومات تحت السطحيه في باطن الارض. وفي هذا السياق، تم اختيار أحد متكشفات تكوين الدام الميوسيني للدراسات الرسوبيه والبتروفيزيائيه. تكوين الدام هو تكوين من عمر الميوسين الأوسط ويتكون من خليط من رسوبيات الكربونات والرسوبيات السيليكيه، ويحده من الأعلي تكوين الهفوف ومن الأسفل تكوين الهدروخ. الغرض من هذا البحث هو دراسة خصائص المساميه والنفاذيه لبعض السحنات الرسوبيه المختاره ضمن الإطار الرسوبي العام لتكوين الدام، وذلك في أحد المتكشفات في منطقه النصبيه في المنطقه الشرقيه من المملكه العربيه السعوديه. المنهجيه المتبعه في هذا البحث تشمل: 1- تحقيق رسوبي تفصيلي لمنطقة الدراسه متضمنه الخصائص البتروجرافيه، 2- دراسة المساميه والنفاذيه لبعض السحنات الرسوبيه، ولاحقا اختيار بعض العينات بغرض دراسة حيود الأشعه السينيه، فحص المجهر الإلكتروني المسحي و التصوير المقطعي الدقيق، 3- النمذجه الجيوإحصائيه للسحنات الرسوبيه، المساميه، والنفاذيه. الدراسات الرسوبيه أوضحت ان تكوين الدام يتألف من طبقات من خليط من رواسب الكربونات والسحنات السيليكيه التي ترسبت ضمن بيئة مسطحات المد. السحنات التي تم إختيارها للدراسات البتروفيزيائيه هي، من الأسفل للأعلي، الجرينستون الأوليتي الهيكلي، الباكستون الرملي الهيكلي، الواكستون المحفّر، والجرينستون الاستروماتوليتي. الدراسه اوضحت علاقه ضعيفه بين المساميه والنفاذيه بالنسبه للسحنات الرسوبيه التي تم إختيارها.فيما يتعلق بالنمذجه الجيواحصائيه، تم انتاج عدة نماذج لكلٍ من السحنات الرسوبيه، المساميه، والنفاذيه. وقد تم التحقق من صلاحية هذه النماذج كمياً وكيفياً بالاستناد علي مقارنة هذه النماذج مع البيانات المعطاه من جهه، ومع الوضع الحالي لتوزيع السحنات الرسوبيه علي مستوي المتكشف. هذه النماذج أوضحت عدم تجانس علي مستوي المتكشف خاصةً في المساميه والنفاذيه حتي بالنسبه لنفس السحنه الرسوبيه. عدم التجانس هذا يمكن ان يعزي لأسباب تتعلق بالعمليات الترسيبيه وعمليات ما بعد الترسيب والتي تؤثر علي جودة المكمن في ظروف

مشـابهه. و بـذلك، فـإن هـذه الدراسـه قـد أوضـحت أنـه بالإمكـان الإسـتعانه بمثـل هـذه النمـاذج، واسـتخدامها كمؤشـر للوضـع الرسـوبي، وتوزيـع خصـائص المسـاميه والنفاذيـه للمكـامن اذا مـا تـم تأكيـد هـذه النمـاذج فيمـا يتعلـــــــق بقابليـــــــة تطبيقهـــــــا عـــــــي النمـــــــاذج تحـــــــت الســـــــطحيه.

# CHAPTER 1

# INTRODUCTION

## 1.1 Introduction

Increasing subsurface technical and geological difficulties require supporting techniques that can be used in both; the exploration and development stages of the reservoir units. One of the methods utilized in petroleum industry is the outcrop analogue which can provide a better understanding of the heterogeneity of reservoir properties, which has great importance in reservoir characterization and geological modeling (Al-Khaliah et al., 2004). In other words, the lateral facies changes over distances less than inter-well spacing can clearly result in challenges for trustworthy reservoir modeling (Felletti, 2004). Since the sedimentary facies represents the principal influencing factor for the porosity and permeability distribution (Sahin *et al.*, 1998), even over very short distances variations can be expected along the reservoir body. Outcrop analogs provide valuable information that could help in characterizing the facies boundaries, internal facies distribution, and their high-frequency cycles (Lindsay and Hughes, 2010).

The Saudi Arabian outcrop scenario represents the equivalents for subsurface geology of the whole Gulf petroleum producing formations. The outcrops which cover most of the Paleozoic, Mesozoic, and Cenozoic Eras, are considered as main targets for understanding and modelling their subsurface equivalents. The sedimentary rocks of the Arabian Peninsula crop out along a curved-shape belt extending from northwest to

southwest of Saudi Arabia, bordering the Arabian Shield in the west of Arabian Plate, the curved-shape sedimentary outcrop belts represent the exposed Paleozoic and Mesozoic formations, on the other hand, the Cenozoic assemblages are distributed in the eastern Arabian Plate and Tabuk Region in the Northwest (Figure 1-1).

Carbonate bodies show considerable vertical and lateral variations in their stratigraphic architecture as well as the values and distribution of porosity and permeability (Alnazghah et al., 2013). When considering these variations, it is important to construct and understand the conceptual models of these parameters which are vital for a better reservoir characterization, especially when these models include facts about depositional facies and spatial porosity and permeability patterns (Borgomano et al., 2008; Warrlich et al., 2008; Harris, 2010; Palermo et al., 2010). Geostatistical modeling of the outcrop bodies is important to show the variability of the geological and petrophysical parameters along and across the exposure, and indirectly to apprehend the possible effect of facies on porosity and permeability patterns at the scale of inter-well spacing. However in most cases of weak or no correlation between outcrop and subsurface petrophysical parameters (Meyer et al., 1996); real subsurface data can be superimposed on the outcrop model (Labourdette et al., 2008; Eltom et al., 2012).

The goal of this study on Dam Formation is to capture the heterogeneity that might affect the spatial continuity of porosity and permeability due to probable vertical and lateral depositional lithofacies variations of the outcrop exposure. This study also aims to provide facies, porosity and permeability models of one of the outcrops of Dam Formation in Eastern Saudi Arabia. Since subsurface data has inherent limitations determined by the techniques of data acquisition, the simulated view of the outcrop will

provide better understanding of how the aforementioned parameters change laterally along the outcrop body.

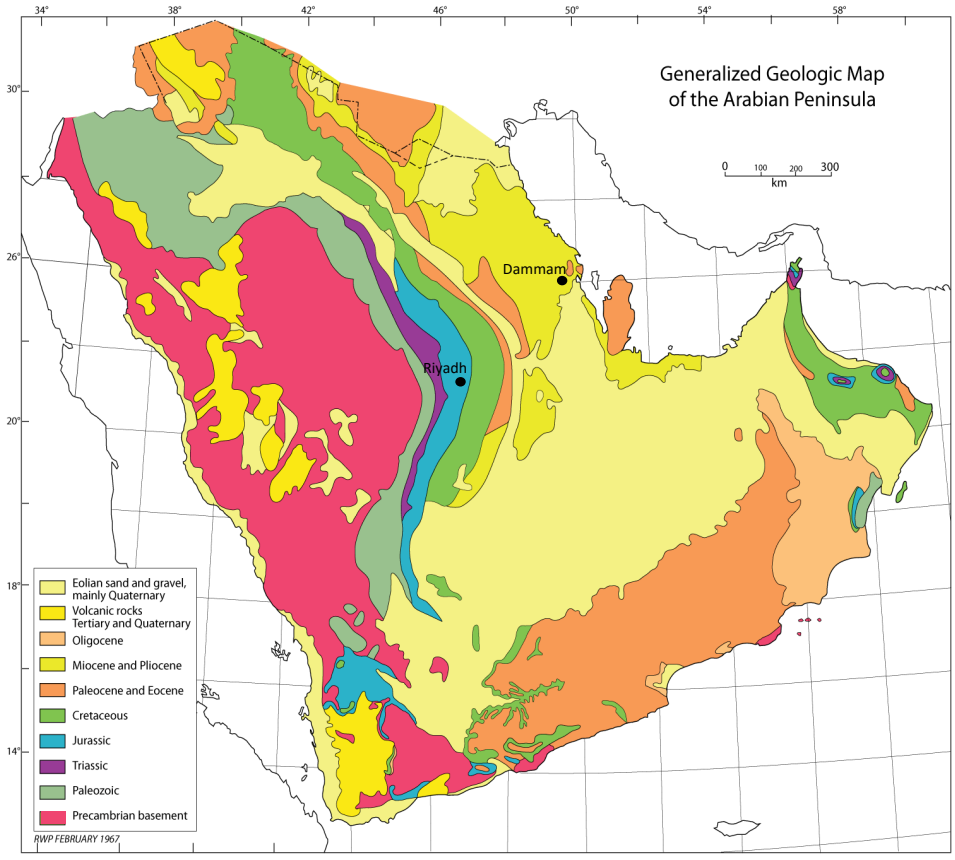


Figure 1-1: Distribution of the Precambrian Shield and Phanerozoic sedimentary succession in the Arabian Peninsula (Powers et al., 1966)

## 1.2 Location of the Study Area

Dam Formation is widely exposed in the Eastern Province of Saudi Arabia. The formation is distributed either in shape of continuous escarpment or as detached outcrops, extending from Al-Nuairyah Area in the North to Salwa Area in the Saudi-Qatari borders, and into the southwestern region of Qatar Peninsula, and Bahrain as well (Figure 1-2).

The study area is located in Al-Nasbiyah Area in the Eastern Province of Saudi Arabia, some 61 km to the Southwest of Dammam City. The outcrop under study represents one of the most extended outcrops in the study area, with 230 m length and varied thickness up to 12 m (Figure 1-3). This makes it suitable for geostatistical modeling of facies and petrophysical properties, besides, the easy accessibility to the study area.

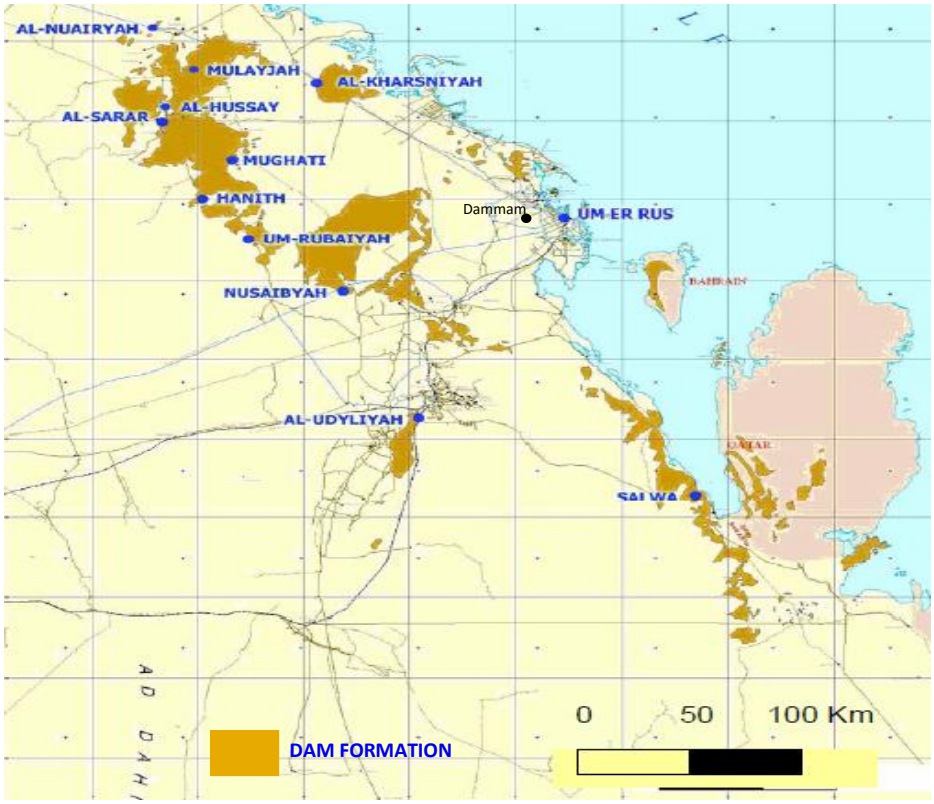


Figure 1-2: Distribution of Dam Formation In the east of Arabian Peninsula (Tayyib, 2007)

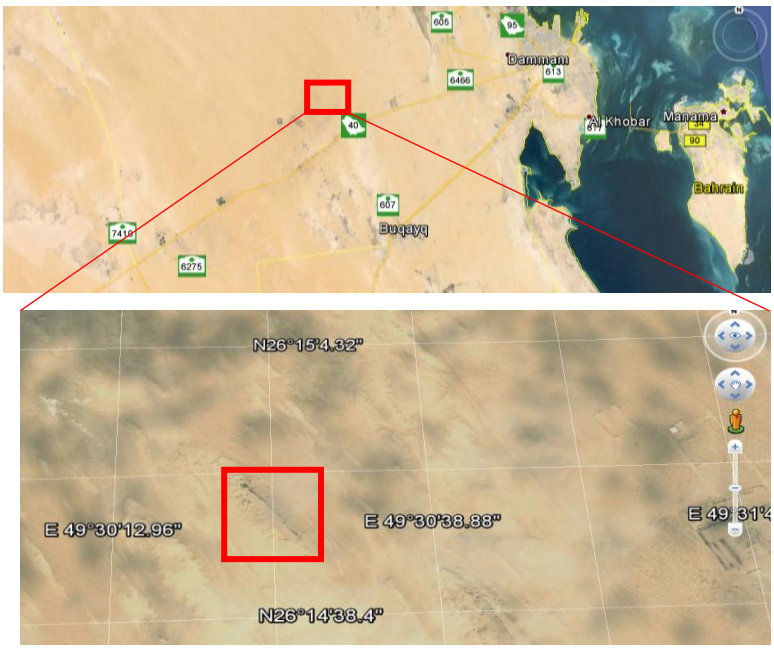


Figure 1-3: Google map showing the location of the studied outcrop in Al-Nasbiyah Area, Eastern Saudi Arabia

## 1.3 Problem Statement and Research Question

Understanding the degree and principal direction of heterogeneity of carbonate reservoirs is a highly demanded exploration task. Depositional or diagenetic changes or both can affect the clean reservoir bodies in terms of their composition, texture, and petrophysical properties. In this context, the importance of outcrop analogue comes to the light since the subsurface setting carries limitations and uncertainties especially at a large (meter and kilometer) scale. Accordingly, the current study will be dedicated to understand the heterogeneity patterns of porosity and permeability behaviors within the best reservoir units of the equivalent outcrop body of the Dam Formation, with respect to the distribution of different lithofacies. The outcomes of this research will include answers of the following questions:

- Throughout the lithofacies setting of Dam Formation; what are the best unit(s) in terms of reservoir quality?
- What are the variabilities in porosity and permeability of the selected unit(s) with respect to the lithology, facies, and depositional setting of the selected outcrop?

## 1.4 Objective of the Study

Integrated geological and petrophysical investigations are expected to provide understanding and answers of the aforementioned questions about reservoir properties. The main objectives of this study are to characterize porosity and permeability within the lithofacies framework of Dam Formation. The research specific objectives are to:

- Characterize the sedimentary facies and depositional setting of the Dam Formation outcrop, which will yield the framework for understanding the reservoir heterogeneity, thereafter selecting the reservoir unit(s) for petrophysical work.
- Investigate the porosity-permeability relationships.
- Establish the variability patterns of facies for the outcrop body, and for the porosity and permeability for the selected unit(s).
- Produce several realizations including facies, porosity, and permeability models for better understanding of these parameters.

## 1.5 Previous Studies

The Arabian Peninsula is one of the most important geological regions in the world. The Arabian Plate is a rich region in terms of basement complexes in the Arabian Shield, and sedimentary rock successions in the Arabian Platform. Arabian Plate hosts the world's most productive oil and gas fields with the Arabian Gulf countries considered as the top ranking oil producing countries. Most of the Arabian fossil energy resources are located in carbonate successions which contain more than 50% of the world reserves (Flugel, 2010). Thus, for these and other considerations, the geology of this area has attracted and still attracting the scientists and researchers.

In the following sections, the tectonic and paleogeographic settings of the Arabian Plate as well as the sedimentology and stratigraphy of Dam Formation will be summarized.

### 1.5.1 Tectonic Setting and Paleogeography of the Arabian Plate

During the late Precambrian, accretion events between ancient micro-plates produced a consolidated shield in the eastern part of Arabian Plate. The most important among these events, Amar collision (640 – 620 Ma) took place when the Al-Rayn micro-plate migrated towards the west and collided with the Arabian Shield creating the N–S Amar Suture (Figure 1-4). Structurally, this collision resulted in several anticlines in N–S trend and surrounded by gigantic NE Bin Batin and NW Abu Jifan Faults (Al-Husseini, 2000). After that, the A-type granitic pluton intruded and initiated a stage of extension which resulted in some collapses in the Shield. That extension was concluded by Najd Fault System that moved the whole area in a left-lateral side for about 300 km and this caused

creation of many rifts in NE direction (Al-Husseini, 2000). Subsequently, there are three main structural elements in the Arabian Peninsula with different chief trends: the North trend system, the Northwest, and the Northeast trend system (*Figure 5*).

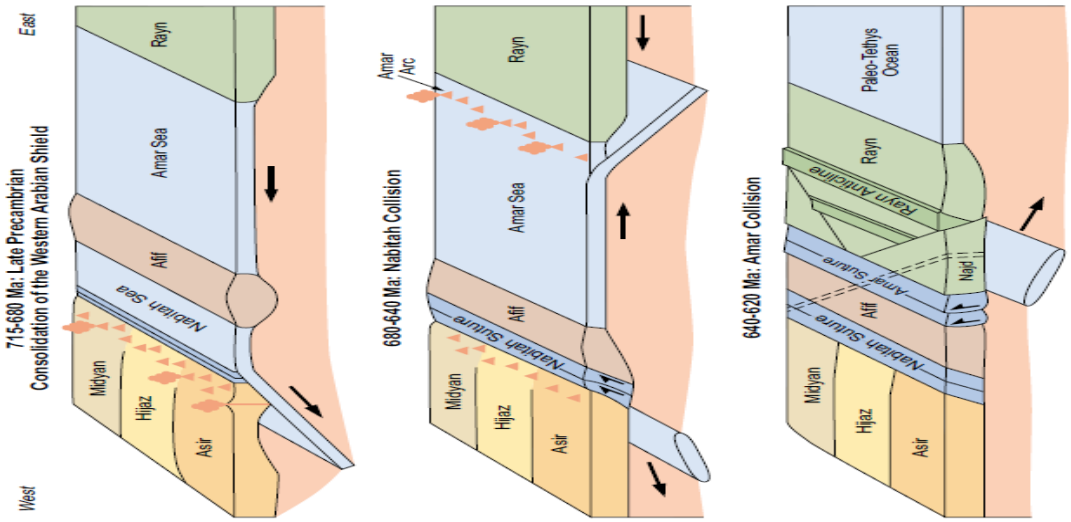


Figure 1-4: The accretion evolution of the Arabian Shield (Al-Husseini, 2000)

The intercalation between the three fault systems resulted in a jointed and complex basement architecture that has been reactivated by subsequent younger deformations (Konert *et al.*, 2001). The Hercynian Orogeny during the Late Paleozoic led to reactivation of the basement fault systems and formed main N-S trending basement involving horst blocks in eastern and central Saudi Arabia.

The Arabian Plate experienced different locations by wandering in an anti-clockwise manner. Starting from latitude 0° to latitude 45° during the Proterozoic to Ordovician-Devonian, and ending by latitude 0° again at Jurassic time when the plate had started to take the orientation of its current day (Figure 1-6) (Konert *et al.*, 2001).

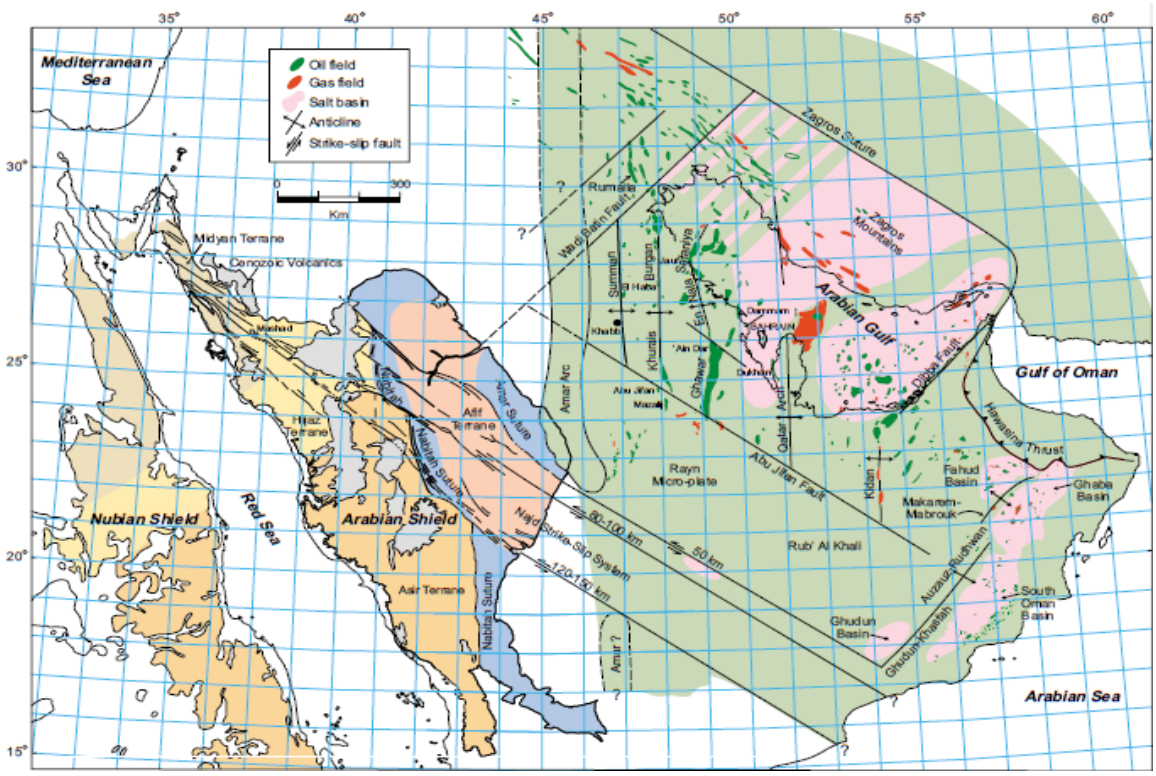


Figure 1-5: The main structural elements of the Arabian plate (Al-Husseini, 2000)

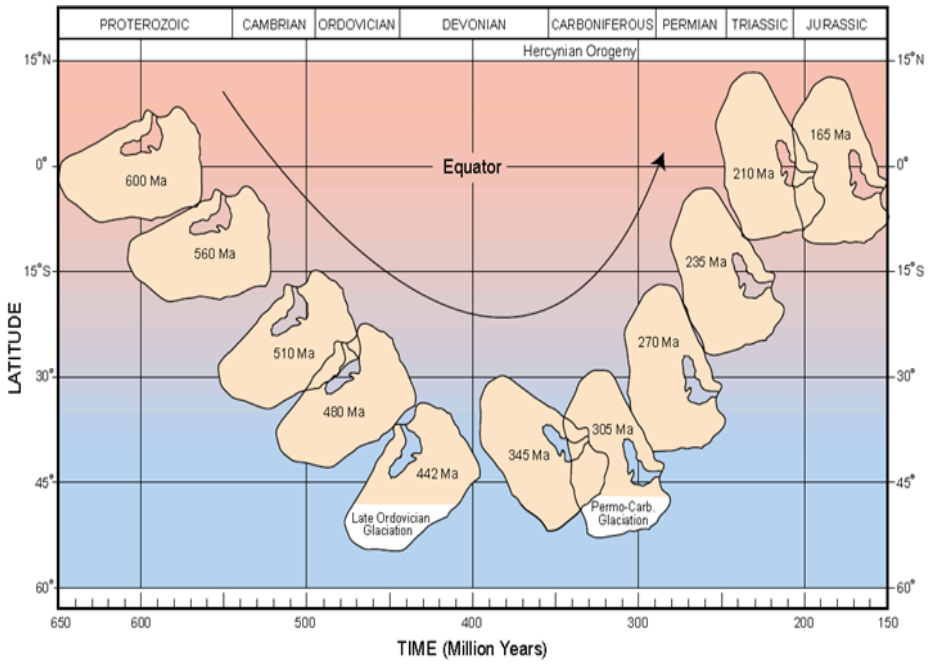


Figure 1-6: Wandering of the Arabian Plate through latitudes during the Phanerozoic time (Konert et al., 2001)

### 1.5.2 Dam Formation

In addition to Hadroukh and Hofuf Formation; the name of Dam Formation was first introduced in the literature by Steineke and Koch in 1935. These authors studied some about 90 m thick units of Dam Formation in Jabal Al-Lidam (latitude 26°21'42"N, longitude 49°27'42" E) (Figure 1-7) in the Eastern Province of Saudi Arabia, where they defined the lower boundary of the formation in the eastern face of Jabal Al-Lidam. According to their works, the lower part of Dam Formation is composed of fossiliferous marl at the top of Hadroukh Formation, and the upper boundary at Al-Umayghir Area (lat. 26°17'15" N, long. 49°30'24" E) is composed of an association of marls, limestones and marine fossils overlain by clays, sandstones, and basal gravel of the Hofuf Formation. Generally, the Dam Formation is composed of white, grey, and pink marl, and

green, olive, and red slightly interbedded sandstone, chalky limestone, and coquina, besides abundance of marine fossils all over the formation. In this context, the best marker zone is near the base of the formation (Powers *et al.*, 1966).

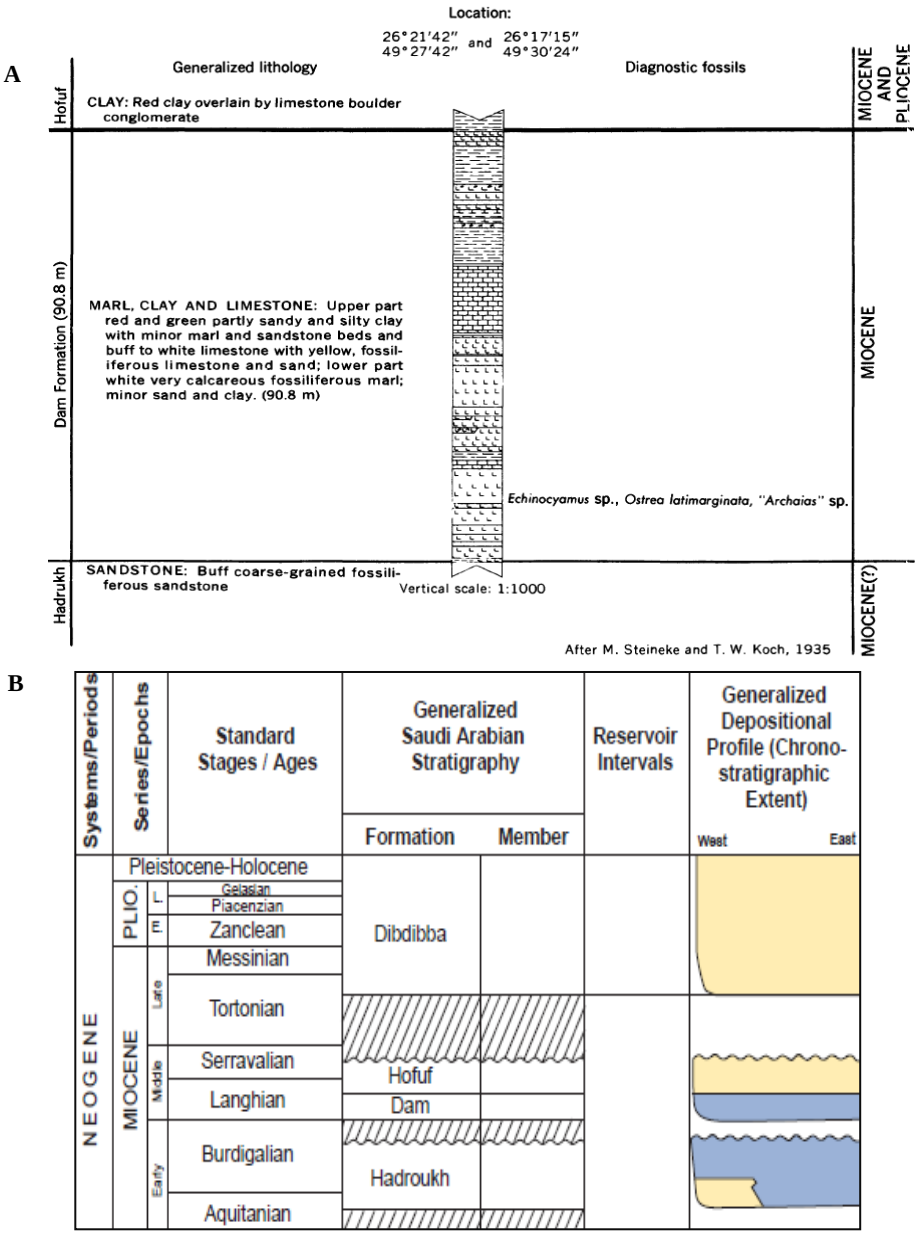


Figure 1-7: A: The type section of Dam Formation (Steineke and Koch, 1935). B: position of Dam Formation in the stratigraphic column of Saudi Arabia (Haq and Al qahtani, 2005)

The Hadroukh, Dam, and Hofuf Formations formally appeared in a paper by Thralls and Hasson (1956). The type sections were described in details by Steineke *et al.* (1958). Using many age-diagnostic species, Powers *et al.* (1966) recognized the age of Dam Formation as Middle Miocene.

During the Miocene (Aquitanian 23.8 Ma to Messinian 5.3 Ma); Hadroukh, Dam and Hofuf Formations of Saudi Arabia, and their regional equivalents; Fars, Agha Jari, and Gachsaran of Iran, and their regional equivalents were deposited in the Arabian Platform (Ziegler, 2001). The European Alpine Orogeny took place in the Burdigalian phase, and regionally, the Red Sea rifting began and led the African-Arabian separation, accompanied by opening of the Aden Gulf. In addition, a strike slip complex faulting deformation occurred along the transform fault zone of the Dead Sea, this event produced faults and uplifts along the Syrian Arc. The Sanandaj-Sirjan thrust zone happened onto the Arabian Plate in the eastern part as a result of Arabian-Asian collision. Simultaneously, the Zagros Foredeep Basin was characterized by huge accumulations of continental to deltaic clastics with shallow marine shales occupying the fast subsiding zone. In Zagros Foredeep Basin, the period between Miocene deposits of post Asmari Formations to the recent sediments occupied five kilometers in the Dezful Embayment (Koop and Stoneley, 1982). The north-trending Hercynian lineaments separate the Miocene associations of the Arabian Plate (Dam and Agha Jari Formations) from Guri Formation in Fars Province. In the vicinity of the Arabian Arch, a string halo of Hadroukh Formation continental deposits and shallow marine Dam Formation were also deposited (Figure 1-8).

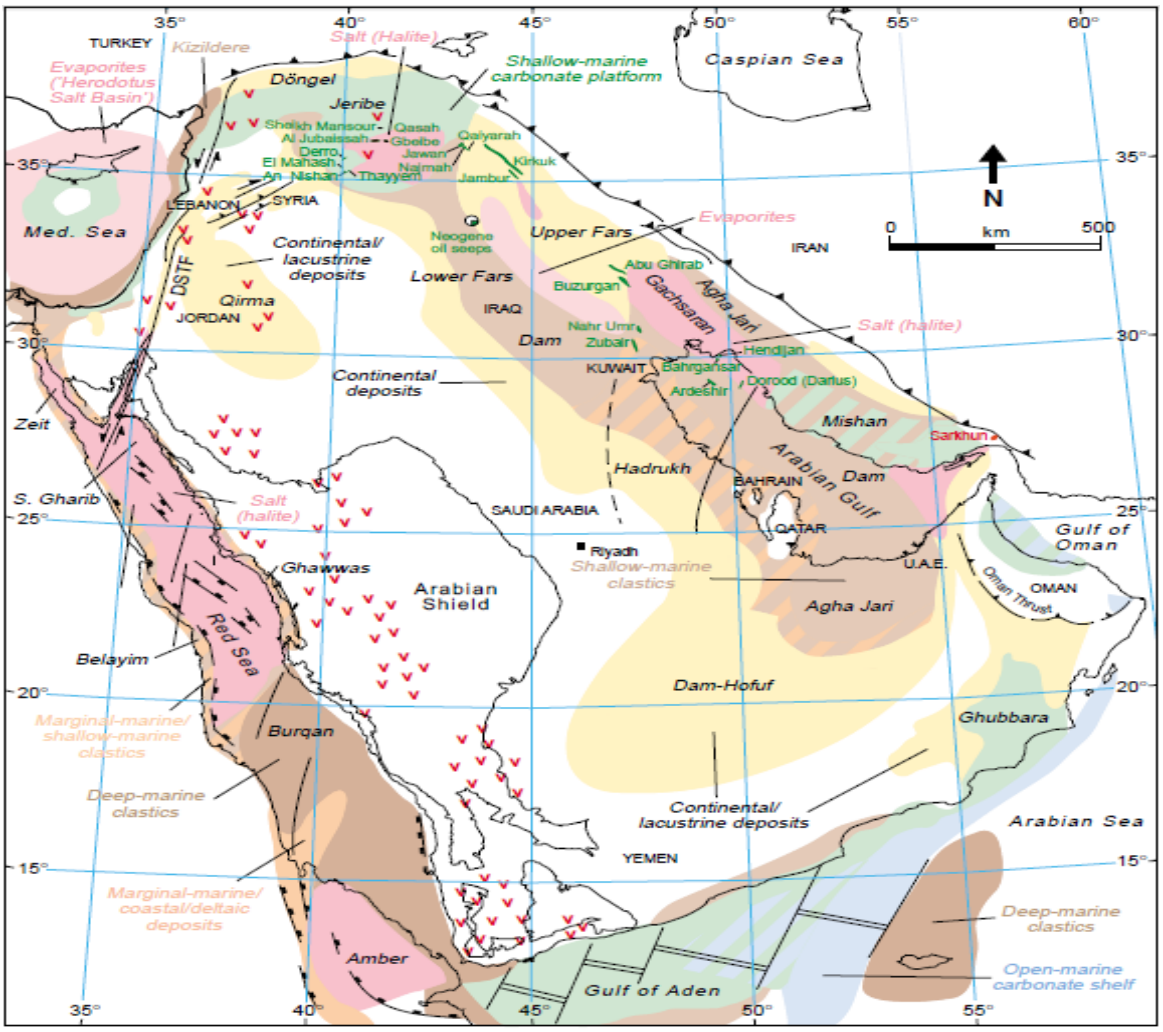


Figure 1-8: Miocene paleofacies deposition: Hadroukh, Dam, and Hofuf Formations (Saudi Arabia), and their equivalents: Fars Formation (Iraq), Agha Jari and Gachsaran Formations (Iran) (Ziegler, 2001)

In Qatar, Dam Formation was divided into lower and upper parts by Cavelier, 1970. With extensive study on the clay constituent, this division was changed into Dam Member A and B by Abu-Zied and Khalifa, 1983.

Tleel (1973) investigated the Dam Formation outcrop in Jabal Midra Al-Janubi with several measured sections. According to his work, the top-most part of Dam Formation composes of massive reef (Siderastrain type), and molluscs.

Irtem, 1986 investigated the tidal flat stromatolites of the Miocene Dam Formation in Al-Lidam Area, Eastern Saudi Arabia. Irtem stated that the stromatolite association occurred in the lower zone of Dam Formation, and concluded that the formation is composed of three deepening upward cycles, and the stromatolites were found at the upper part of the third cycle. Typically, the deepening upward cycle starts with supratidal gypsiferous claystone which grades up into intertidal sandstone and shallow sub-tidal to lower inter-tidal limestone, and thinly bedded oolitic grainstone. Stromatolite associations occur as close, detached, columnar structures which are common in oolitic grainstone as intraclast which derived from stromatolite lumps. The Faunal assemblage and lithology features of the oolitic, stromatolite-rich grainstone indicated the shallow sub-tidal to lower inter-tidal environment.

Hewaidy, 1991 investigated the foraminiferal association of Dam Formation in Jebel Al-Nakhash and Al-kharrara Area, the author dated the Dam Formation as Burdigalian – Helvetian (Lower to Middle Miocene).

In Jabal Al Nakhash Area, Khalifa and Mahmoud, 1993 recognized three types of algal

stromatolite in the B Member of the formation. These stromatolites were related to protected tidal flat environment.

The stratigraphy, micropaleontology, and paleoecology of the Dam Formation in Qatar were studied by Al-Saad and Ibrahim in 2002 where they related the formation to shallow tidal flat environment in arid and saline setting.

Correlative study between the microbial components of the recently deposited sediments in the coast of Arabian Gulf of Saudi Arabia, with the components of Dam Formation in Jabal Midra Al-Janubi was done by Al-Enezi, 2006. As a result of this work, wackestone, packstone, and grainstone with foraminifera colonies have been defined in small scale shallowing upward cycles.

In Iraq, the Middle Miocene (Langhian) Jeribe Formation (Jassim and Goff, 2006) is the equivalent of the Middle Miocene (Langhian) Dam Formation of Saudi Arabia (Haq and Alqahtani, 2005). The carbonate inner shelf and shoal (Jeribe Formation) was first defined as an Early Miocene Formation (Bellen *et al*., 1959)., however it had been later included within the Middle Miocene sequence where its age is indicated by the presence of Orbulina datum near the base of the formation (Prazak, 1974). Bellen *et al*., (1959) suggested that the Jeribe Formation was deposited in lagoonal (back-reef) and reef environments and that back-reef facies are predominant. In North Iraq, and locally in South Iraq, Jeribe and Euphrates Formations represent some of the Tertiary reservoir intervals of the main oilfields, where Lower Fars evaporites regionally seal the underlying Miocene Jeribe and Euphrates Formations, and the Oligocene Kirkuk Group. Jeribe and Eupharates have both primary and secondary (due to dolomitization)

porosities, Jeribe Reservoir porosity ranges from 14 to 21% (averaging about 17%), its permeability varies from 1 to 1146 md (averaging about 200 md) (Jassim and Goff, 2006).

Tayyib (2007) studied many localities of Dam Formation in the Eastern Province of Saudi Arabia, he investigated the impact of depositional setting of the Dam Formation limestone units on the Portland Cement quality. The study was based on field work, geochemistry, and mineralogy, comparing among the twelve different locations which had been studied. Tayyib concluded that the very warm water lagoon with moderate circulation environment found in northern and northwestern part of the Dam Formation at Al-Nuairyah, Mulajah and Al-Sarrar areas, is the best environment, and the hypersaline tidal pond environment in the middle is a good environment. However, the deposits of muddy lagoons, tidal pond, and tidal channel environments in the southern part are unsuitable for Portland Cement production because of their high silica contents and the dolomitization effect.

Al-Khaldi (2009) investigated the outcrop of the middle Miocene Dam Formation in Al-Lidam Area, he studied the lithofacies setting and distribution within high resolution cycle stratigraphic framework, and considering the controls on hierarchy of the Miocene Buildups. His work targeted one outcrop in the study area. Stratigraphically, Al-Khaldi divided Dam Formation into three composite sequences, four high frequency sequences were established equally in two of the three composite sequences, the outcrop is dominated by mud-cracked stromatolites, tidal flats, red beds, ooid grainstone, dominantly mono-specific skeletal banks, and adjacent continental eolian facies at the Lidam escarpment.

Those lithologies reflect the mixed carbonate–siliciclastic succession in a closed embayment on a homoclinal ramp.

# CHAPTER 2

# LITERATURE REVIEW

## 2.1 Introduction

Outcrop studies have always been and are still attracting scientists for many years. By considering the limitations of subsurface data to understand the geological setting, and later on the properties of the units under investigation, this fact is reasonable, since the outcrop investigation has taken place as a tool to fill the gap of limited subsurface data, particularly, that related to reservoir heterogeneity.

Many studies were conducted on outcrops of different rock types, environment, geological setting, and tectono-staratigraphic setting, what reflects the applicability of outcrop studies in wide range of geological settings. In the following I review the relevant literatures, with main focus on porosity and permeability.

## 2.2 Literature Review

Eltom et al. in 2014 investigated the outcrop of Arab-D member of Arab Formation and Upper Jubaila Member of Jubaila Formation as analogues to better understand of subsurface reservoir stratigraphy, facies architecture, and heterogeneity, since the outcrop studies have a lot of information that are related to the large inter-well intervals even within the confines of an individual petroleum field. The study included sedimentology, petrography, spectral gamma ray, porosity, permeability, and geochemistry, then using

geostatistics as a tool for 3D modeling of these parameters. The authors identified three lithofacies associations deposited on a gentle-slope carbonate platform, these litofacies included nine internal high frequency depositional sequences. Regarding the reservoir properties' variability, the outcrop reflected a small scale reservoir heterogeneity that was represented by the 3D geocellular modeling, although the outcrop's petrophysical parameters are different from that of the subsurface.

In Eastern Spain, a well-exposed Upper Kimmeridgian carbonate ramp was investigated by Alnazghah et al., 2013 as an analog for subsurface Arab-D reservoir in Middle East and Smackover in Gulf of Mexico. The goal of the study had been to investigate the inter-well heterogeneity in the ramp succession (1.3 km long, 40 m thick), using five detailed measured sections (around 300 m interval) and photomosaic to construct the 2D lithofacies view. The study showed that the large scale of facies heterogeneity rules the fluid flow in reservoir environment, although this scale is much below the resolution of subsurface exploration tools.

Borgomano et *al*., 2013 studied the porosity and permeability in the Lower Cretaceous carbonate outcrops in Urgonian Province, southeast of France. The high resolution analyses included more than 500 plugs for porosity and permeability measurements selected from carbonates of grain supported texture.

The main goals of the study had been collecting petrophysical data from the carbonate exposure, examining rock porosity and permeability, identifying spatial heterogeneity in rock properties from plugs to inter-well scale, and finally construct a framework for modelling and upscaling of the mentioned petrophysical parameters. The importance of this work for the Middle East is the sedimentological and chronostratigraphic analogies

of these carbonate outcrops to the Barremian to Early Aptian carbonate reservoirs reported in east of Arabian Peninsula including Shuaiba and Kharaib Formations (Masse, 1995; Dercourt *et al*., 2000).

According to the authors, the study is most important for the distribution of reservoir properties and modelling at the inter-well scale, this had been expressed by petrophysical variations related to stratigraphy and sedimentary structures. By conventional field works and petrography, the authors recognized three principal rock types, each of which relates to a precise pore system. These are: 1- moderate intragranular -microporosity in the fine grained grainstone which explicit good homogeneity at all scales, low permeability, however the poro-perm correlation is strong with weak sedimentary-diagenetic anisotropy, 2- coarse grained grainstone with intragranular microporosity, moldic and intergranular porosity with all scale homogeneity, the poro-perm correlation is moderate with weak sedimentary anisotropy, 3- complex pore type characterize the rudstones facies including intra-skeletal, intergranular, and moldic microporosity) which reflects clear heterogeneity at small scales, weak poro-perm correlation and robust sedimentary anisotropy. The random sampling of plugs do not reflect representation of the reservoir effective properties for the coarse fabric rocks besides the pore fabric as rudist rich rudstones, according to the authors, and as a contrary to the finer fabric with fine pore system, the effective reservoir properties for the coarser rocks requires samples larger than plugs. From the two-dimensional simulations, via geostatistics; two permeability models (by Sequential Gaussian Simulation and poro-perm transform from porosity model) for the homogeneous grainstone can be comparable, however those models

showed different behaviors for heterogeneous rudstone, the degree of correlation depended on poro-perm relation.

Eltom *et al*., 2012 used outcrop analogues to construct a high resolution model for the Jurassic Arab D reservoir (Upper Jubaila Member of Jubaila Formation, and Arab D Member of Arab Formation) in Central Saudi Arabia. This high-resolution model aimed to realize the spatial behavior of the reservoir unit at surface scale, the authors matched the lithofacies and porosity of the studied outcrop to the published subsurface data from Uthmaniyah, Shudgum, and Ain Dar Fields of the giant Ghawar Field in east of Saudi Arabia. Using geostatistical modeling, nine models of porosity have been built using minimum, average, and maximum porosity of subsurface to each facies that were assigned. The variability of these models was assessed by running many realizations for each one, in addition to measuring the uncertainty related to the models. As a result of the established ties between porosities and lithofacies, the potential carrier zones were related to grainstones, packstones and some wackestones, the direction-dependent behavior of the semivariogram illustrates that the continuity is good in N-S direction, and less in E-W direction. Moreover, the permeability barriers and low porosity zones have been identified by the high resolution models of lithofacies.

Leonide *et al*, 2012 investigated the relation between the architecture of the stratigraphy of the Barremian - Lower Aptian Monts de Vaucluse and its multiscale heterogeneities in the Urgonian carbonate platforms, Southeast France. This relation used to build spatial distribution of reservoir patterns based on detailed and high resolution measured sections and microfacies inspection, bio stratigraphy and paleoenvironment interpretations, and

sequence stratigraphy framework with high focus on discontinuity surfaces and its stratigraphic correlation and environmental sense. This work has come up with thirty types of elementary facies (twelve facies associations and five stratigraphic sequences), those depositional sequences have been clustered into two dischronous and different carbonate systems; the gentle slope-flat top platform without shelf break, and the outer shelf steepening-flat top platform, the authors concluded that the smaller scale of heterogeneity defined by three dimensional facies within each stratigraphic unit, in contrast with the larger scale, represents the transition between the inner platform and outer shelf profiles.

Koehrer *et al*. 2010 used sedimentological description, field gamma ray, petrographic thin section, porosity and permeability laboratory measurements and cathodoluminescence microscopy to define multi-scale facies and variations of reservoir quality within a dolomite body as an outcrop analogue in the Middle Triassic succession of the Southwest German Basin. The study targeted the porous dolomitic body in the proximal area of an epeiric Triassic carbonate ramp which is equivalent to the hydrocarbon rich reservoir of Khuff and Arab Formations. According to the authors, the dolomite bulk is composed of shoal, lagoon, peritidal facies which have been built by threefold hierarchy cycles from $3^{rd}$ to $5^{th}$ order. This study indicated that the dolomite reservoir of best quality was found in fine lagoon dolomitic mudstone enhanced by micro intercrystalline and vuggy pore spaces. Various ranges of reservoir potential has been observed in the coarse shoal dolomitic grainstone; this variation was linked to diagenetic effect.

In terms of stratigraphy, the authors linked the highest dolomite porosities to the upper regressive portion of the 3rd order cycle, this quality decreases bottomward of the section in the limy facies. Facies, porosity and permeability showed lateral continuity at the 10s meters scale, considerable heterogeneity of these parameters has been observed at 100s meters scale within the 5th order cycle, however, the lithofacies distribution is managed by the inclined geometry of the carbonate ramp which is considered as a 1000s meters scale. Lithology, facies, porosity, and permeability data have been used to construct a 3D geostatistical model for each parameter, for this purpose, Petrel software was used. The poro-perm variation models are correlated to the grade of heterogeneity which is a combination of lateral lithology changes and facies variability.

Sandstone Reservoir equivalents outcrops were targeted by Felletti, 2004, where he integrated the conventional outcrop investigations with geostatistics, in a Late Oligocene-Miocene turbidite sandstone in the eastern region of the Tertiary Piedmont Basin of Northwestern Italy. The author used the geological model that he built as a template for the geostatistical simulations of the small-scale geological heterogeneities. The author concluded that a better understanding and characterization of the depositional environment can be attained by Conditional Gaussian Simulation from the variations that appear clearly on facies assemblages.

Jennings et al., 2000 studied the variability in permeability of the shallow water carbonate platform outcrops in the west of Texas and New Mexico. By targeting two scales of heterogeneity (large scale of 40 to 50 m interval, and small scale of 1 to 2m), the authors could show 2 up to 5 orders of variability in magnitude, and the majority were

found in the small-scale lag distance. This study reflects the importance of sampling strategy to reveal the different scales of variability.

Through one section in the topmost Maastrichtian chalks exposure, Frykman, 2001 intended to *a)* evaluate the spatial variability of porosity and permeability, and their relation to geology using a systematic procedure of variogram analysis *b)* identify the cyclicity in petrophysical properties in the pure (homogeneous) chalk and *c)* correlate the section with subsurface chalk reservoirs in North Sea. This outcrop study had been done in the Sigerslev quarry at Stevens Klint, Denmark. The study showed small scale (centimeter) heterogeneity of petrophysical parameters with the geology context, moreover, the outcrop did not show correlative analogue to the subsurface reservoir except the trend and variability patterns of some basic material properties such as the porosity and permeability trend.

Misra *et al.* 1998 investigated the lateral spatial variability in petrophysical properties for the outcrop analogs at the inter-well intervals in the marginal marine environment of the upper Almond Formation nearby Rock Springs, Wyoming, United States. This work included detailed core plug porosity and permeability measurements, petrography and compaction parameters. The results show that compaction caused porosity loss in tidal delta and shoreface sands, while both compaction and cementation reduced the tidal channel sandstones' porosity. The variogram modeling for petrophysical parameters can be used for prediction due to the consistence of its variance and continuity even though the geography of reservoir features is variable.

Sahin *et al*., 1998 collected well log driven-porosity measurements in the reservoir rocks of Hanifa Formation, and Arab C and D members of Arab Formation, from thousands of

porosity measurements in three hundreds wells. The authors targeted the relation between geology and porosity variogram patterns. Clear variogram features related to structurally controlled anisotropies, and short ranges with great nugget variances belonged to the more complex lithology layers.

Senger et al., 1992 worked on the deposits of a carbonate ramp in the upper San Andres Formation where it is cropping out along the Algerita Escarpment in New Mexico. The authors tried to characterize complex heterogeneity related to depositional and diagenetic effects within the inter-well spacing scale. For the permeability investigation, the authors applied detailed measurements using both field permeameter and core plugs. From the multiple parasequences that had been established on the 10 to 40 ft thick reservoir intervals, the authors noticed discrete variation of the petrophysical properties within the scales less than inter-well spacing. The variation in permeability was referred to local random heterogeneity (nugget effect) which had been confirmed by conditional simulation, moreover, the numerical water flood simulation (by several conditional realizations) has been accommodated with the numerical simulation of the geometric mean permeability distribution.

# CHAPTER 3

# METHODS OF INVESTIGATION

## 3.1 Introduction

As mentioned earlier, this work includes reconnaissance field trips, conventional field works and logging, establishing facies geometry and architecture through high resolution photographs and mosaic, determining sampling strategy for geostatistics, all these steps can be categorized under field work. Regarding the laboratory works, which is the backbone of the study, the work includes petrographic investigation of facies and facies associations, plug preparation, porosity and permeability measurements for the selected reservoir-prone facies. The last stage is the geostatistical and variogram modeling of the facies, reservoir porosity and permeability. These procedures are illustrated below (Figure 3-1).

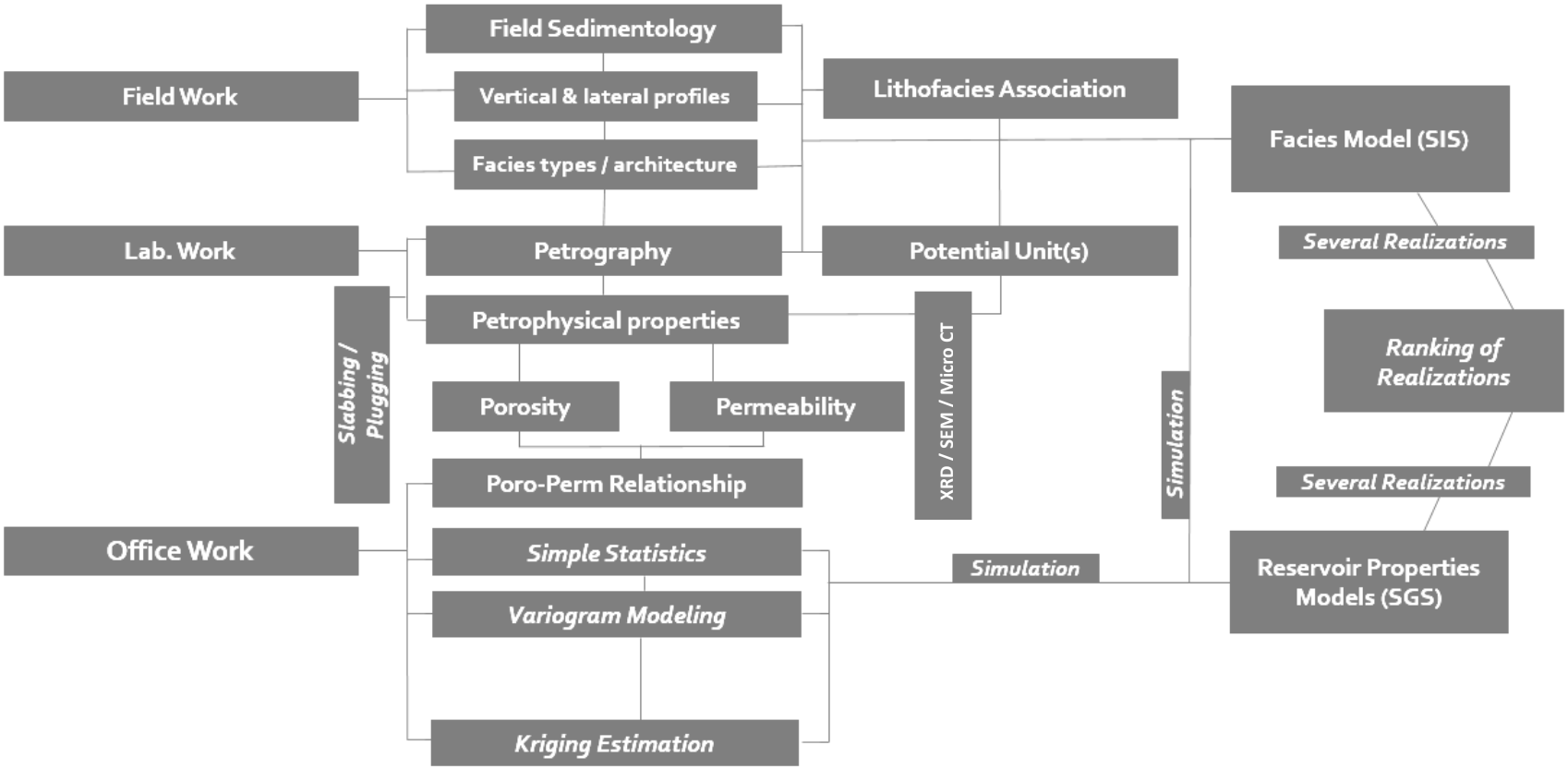


Figure 3-1: Diagram showing the research procedures

### 3.1.1 Field Work

The ultimate task of this part is to construct the facies model through identifying the sedimentary lithofacies and lithofacies associations. Middle Miocene Dam Formation is well exposed in Al-Nasbiyah Area in Eastern Province of Saudi Arabia, one outcrop was selected to fulfill the objectives of this work mentioned earlier. The studied outcrop is about 231 m long, with varied thicknesses along the exposure (maximum thickness is 12 m, and the minimum is 3 m). Five high resolution sedimentological logging sections were performed from bottom to the crest of the outcrop, taking into account lateral facies changes. Field sedimentology description included -but was not restricted to- Dunham classification of carbonate texture, color, thickness, structures, bioturbation and fossil contents, and bedding contacts. Detailed sampling was performed for each section with respect to distribution of lithofacies along the exposure, these samples were used for further description through thin section petrography. Total of 254 samples were collected from the outcrop. These samples were used for detailed petrographic and petrophysical analyses.

### 3.1.2 Laboratory Analyses

This part represents the core of the research, since all later analyses depend on the quality of laboratory works. The laboratory investigations included: sample slabbing, slab imaging, petrographic thin section preparation, and cylindrical core plugs preparation. Thin sections were prepared from samples collected from five measured sections with more focus on lithofacies selected for porosity and permeability. 254 core plugs were cut; including samples of petrographic sedimentology and lithofacies analyses.

### Thin section Petrography

Thin section petrographic analyses were conducted to investigate the litofacies of Dam Formation as well as facies heterogeneity, and then correlate them with petrophysical parameters. The samples selected for petrographic analysis were impregnated with blue epoxy pressurized incubator. After the impregnation, the sample is left over night for curing. Then the sample is glued to glass slides using Canada Balsam and kept under pressure to stick to the glass appropriately. The rock piece is cut from slides leaving the thin layer on the glass. Silicon carbide is used for grinding the glass mounted slab consequently to get polished and smooth surface. The thin section is then analyzed visually by point count method under plain-polarized microscope (Krumbein and Pettijhon 1961).

### XRD, SEM and Micro CT-Scan

X-Ray Diffraction (XRD), Scanning electron microscope (SEM) and Micro CT-Scan were applied on four selected lithofacies in order to get more detailed sedimentological and petrophysical properties. These lithofacies represent the target of later porosity and permeability analyses.

### Petrophysical Measurements

The rock samples were cored to prepare 254 plugs for porosity and permeability (vertical and horizontal). Porosity was measured using gas expansion and saturation, while gas permeability method was used for permeability capturing in both vertical and horizontal directions.

**Porosity**

The total porosity can be defined as a fraction of bulk volume of the rock which is not filled by the solid matter (Tiab and Donaldson, 2004), there are two types of porosity, the primary porosity which develops during the deposition time, and the secondary porosity which results from later diagenetic processes. If V is bulk rock volume, $V_s$ is the solid volume, $V_p$ is the pore volume; then the porosity can be estimated as fraction as:

$$\phi = \frac{V - V_s}{V} = \frac{V_p}{V} = \frac{\text{Pore Volume}}{\text{Total Bulk Volume}}$$

**Gas expansion and Helium porosimetry**

The theory behind gas expansion is based on Boyle's law where the sealed rock is put in a container of known volume ($V_1$) in atmospheric pressure ($P_1$), a valve is attached to both the rock container and to another container also of known volume ($V_2$) which contains a gas with known pressure ($P_2$). The valve is opened slowly until the equilibrium pressure is reached which is used later to estimate the grains volume (Vs Boyle's law guarantees the constancy of volume times the pressure. If ($P_3$) is the total pressure of the two container volumes; then:

$$P_1 (V_1 - V_s) + P_2 V_2 = P_3 (V_1 + V_2 - V_s)$$

The grain volume can be calculated as:

$$V_s = \frac{P_1 V_1 + P_2 V_2 - P_3 (V_1 - V_2)}{(P_1 - P_2)}$$

Helium is frequently used in research and industry as the expansion gas (Figure 3-2, 3-3), the less permeable rocks usually need longer time to reach equilibrium to allow flow into narrow and tight pore geometries (Torsæter and Abtahi, 2000).

Figure 3-2: TPI-219 Helium porosimeter device used for porosity measurements (coretest.com)

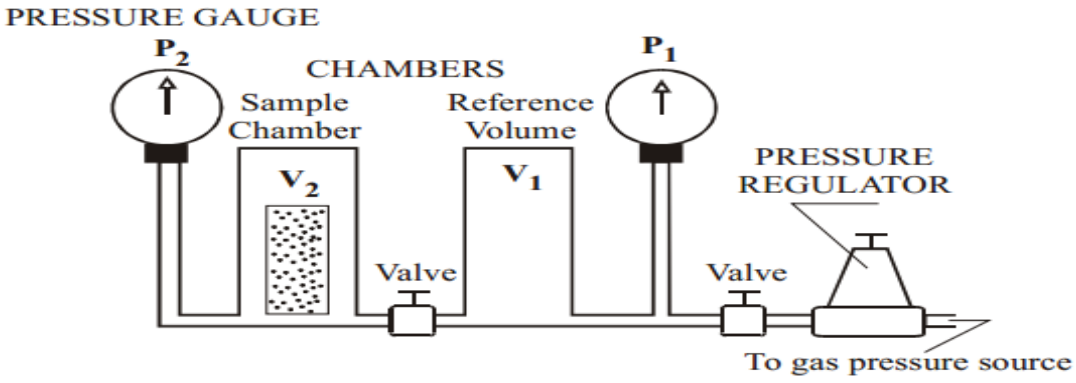


Figure 3-3: Theory of Helium porosimetry (Torsæter and Abtahi. 2000)

**Permeability**

For a successful reservoir, the rock should have an ability to allow fluid movement through the connected pore spaces, this ability of rock to conduct fluid is called permeability, hence this points out to non-permeability of a non-porous rock (Tiab and Donaldson, 2004), Rock permeability depends mainly on the effective interconnected porosity but is also affected by many other factors including grain shape, grain size, grain sorting, grain cementation and packing. Permeability can be measured on core plugs using laboratory permeameter (Figure 3-4).

One of the mathematical tools that has become a standard for petrophysicists and petroleum engineers is the fluid flow equation which had been discovered by a French engineer “Henry Darcy”. This formula states that:

$$u = \frac{q}{A_c} = -\frac{k}{\mu}\frac{dp}{dl}$$

where:

u = velocity of the fluid (cm/sec)

q = rate of flow ($cm^3$/sec)

k = porous rock permeability (Darcy = 0.986923 $\mu m^2$)

$A_c$ = cross section area of the rock ($cm^2$)

μ = fluid viscosity (centipoises cP).

L = rock sample length (cm)

dp/dl = directional pressure gradient (flow direction) (atm/cm)

However, a permeability of one Darcy in petroleum reservoir setting is very rare, since in most cases the reservoir permeability does not reach more than a few tens or hundreds milli Darcies (mD). Millidarcy is commonly used in petroleum industry. The above equation is valid for absolute permeability i.e. when only one fluid or phase is flowing in the rock. This term modifies to effective permeabilities (and to relative permeabilities).

When more than one fluids are present, most probably water, oil, and gas occur together in the reservoir, each of which having its own effective permeability (Tiab and Donaldson, 2004). In Petroleum Industry, (as well as in Hydrogeology) both horizontal and vertical permeabilities are considered to get a full view of the flow regime in the reservoir. In a similar way to the porosity; permeability has two genetic types: the primary and the secondary. Primary permeability (matrix permeability) is created at the deposition time and through the later lithification of the rock, any considerable alteration of the matrix by any means (fracturing, dissolution, cementation, compaction,…) might lead to a secondary permeability.

**Gas permeability**

The TKA-209 utilizes a steady-state flow technique and is operated manually. Measured pressure and flow data from the digital display meters on the front panel are used to calculate permeability after reaching steady-state flow condition. The TKA-209 Gas Permeameter system consists of 4 sides containing the main equipment components (Figure 3-5), which are distributed on the Top panel, the Front panel, the Right side and the Back side (Figure 3-4).

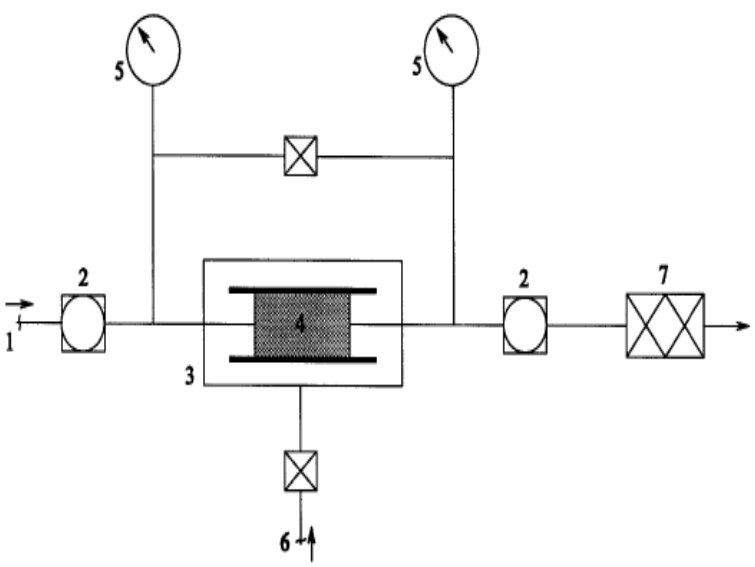


1. Air supply
2. Reduction valves
3. Core holder
4. Core sample
5. Manometers
6. Sleeve pressure
7. Wet-test meter (gas-volume measurement)

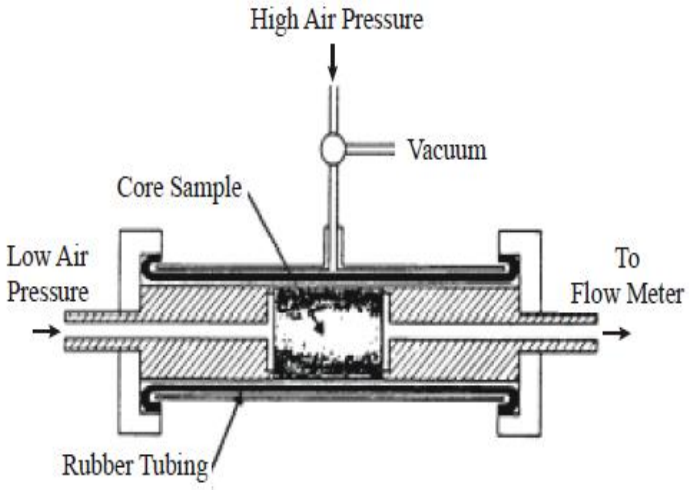


Figure 3-4: Lab permeameter device (Torsæter and Abtahi, 2000)

The Manual calculation of Standard permeability:

$$K_g = \frac{2\mu_g Q_g P_{atm} L}{A(P_1^2 - P_2^2)} * 1000$$

Where:

Kg = Permeability to gas, milli-darcy (not corrected for slip).

$\mu_g$ = Gas viscosity, centi-poise (At the flowing temperature).

Qg = Gas flow rate, cubic centimeter/second.

Patm = Atmospheric pressure inside the laboratory, atmospheres.

L = Core Length, centimeter.

A = Cross-sectional area of the cylindrical core, cm*2.

$= \pi / 4 * (D * 2)$.

P1= Inlet pressure, atmospheres.

P2= Outlet pressure, atmospheres.

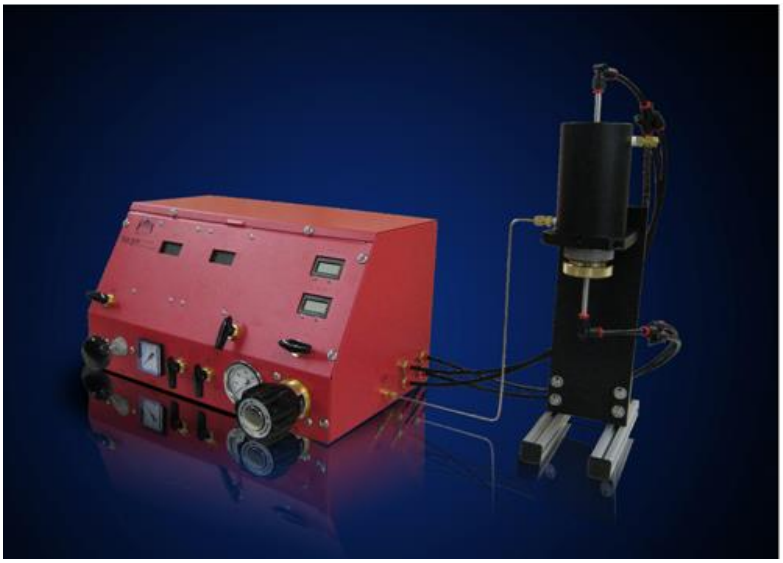

Figure 3-5: TKA-209 Gas Permeameter used for permeability measurements

(coretest.com)

To calculate gas viscosity, use the following equations:

For Air: Viscosity, $\mu_a$ (cp) = (Temperature, ° C) 0.0000493477 + 0.0171204

For Nitrogen: Viscosity, $\mu_{N_2}$ (cp) = (Temperature, ° C) 0.0000420067 + 0.016593

For Helium: Viscosity, $\mu_{He}$ (cp) = (Temperature, ° C) 0.0000489855 + 0.018259

$Q_g$ = Flow rate of gas reported from meter reading at the flow conditions in cc/min. is converted to cc/sec by dividing by 60.

$P_a$ = Atmospheric pressure, atmospheres absolute

$$= \frac{Barometer\ \mathrm{Re}ading, mm - Hg.}{760}.$$

$P_1$ = Inlet pressure, atmospheres absolute.

We get differential pressure, $\Delta$**P** from the meter front panel in psid.

When $\Delta P < 3$ psi: P1 = Downstream Pressure + $\Delta P$ + Atmos. Pressure, $P_a$.

When $\Delta P \geq 3$ psi: P1 = Upstream Pressure + Atmos. Pressure, $P_a$.

To convert the digital differential pressure display readings from psid to atmospheres multiply by 0.06805. Be sure to subtract the pressure reading taken with the end piece removed from the core holder.

Downstream Pressure is the meter reading when the end piece removed from the core holder.

Upstream Pressure is the side gauge reading during flow steps in psig and converted to atmospheres by multiply by 0.06805.

$P_{\Delta P}$ = Differential pressure (Read from meter and convert to atmospheres).

$P_2$ = Outlet pressure, atmospheres.

= Downstream Pressure + Atmospheric Pressure, $P_a$

L and A = Sample length, (cm.) and sample area, (sq.cm.).

**Verification of Klinkenberg effect**

**Principle**

The data from gas permeability measurements are used. Several gas permeability values, at different pressures, are plotted against the reciprocal of the mean pressure (1 / (Pm-1.0))**.** The intercept of the best fit straight line resulted with the gas permeability axis at zero $1/p_m$ is equal to the liquid permeability because this means that the gas is pressurized to infinity and became in the liquid phase.

**Procedure**

The procedure for this experiment is the same as for gas permeability measurement**.** However, in this case several gas permeabilities are measured at different low flowing pressures**.** In addition to that, liquid permeability measurement for the same rock sample as mentioned in the last experiment is also measured for correlation purposes**.** The Core-Lab Gas Permeameter is used for this part as described before for the determination of gas permeability.

**Calculation**

Klinkenberg used the following relationship to determine the slip effect of gases and determined the liquid permeability**:**

$$K_l = \frac{K_g}{1 + b / P_m}$$

Where**:**

$K_l$ = Permeability to non-reactive liquid = ($k\infty$).

$K_g$ = Permeability to a gas

$P_m$ = Mean pressure of flow

b = Klinkenberg constant for a given gas in a given porous media.

Klinkenberg relationship can also be written as**:**

$$K_g = K_l * b * 1 / P_m + K_l$$

Since we are getting different values of Kg at different mean pressures, we can compare this equation with the straight line equation Y = m X + c.

Where**:**

m = the slope of the straight line resulted**.**

c = the intercept of the line with the Y-Axis (gas permeability axis)**.**

Therefore, $Y = K_g$, $m = K_l * b$, $X = 1/P_m$ and $c = K_L$. .

We can use the data and results in the excel sheet to**:**

(a) Plot $K_g$ versus $1/P_m$

(b) Determine the value of Kg at the intercept. (Note this value is equal to KL or K∞.

(c) Find the slope m, and then get the Klinkenberg constant b.

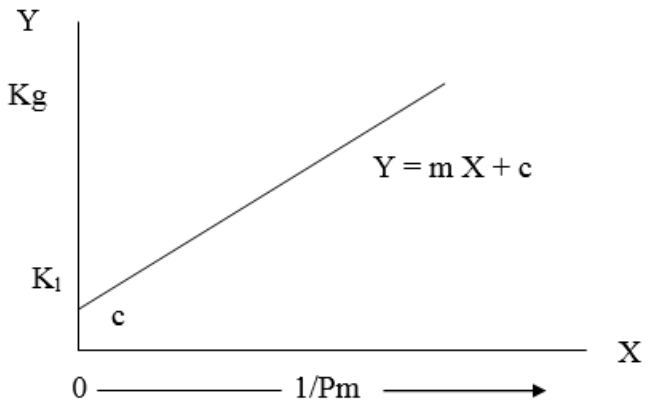


From the above plot, the value at $1/P_m = 0$ represents infinity $P_m$ and the gas behaves as liquid. Therefore, the value of $K_g$ on Y -axis at the intercept C is equivalent to liquid permeability $K_l$**.**

### 3.1.3 Geostatistical Modeling

Classical Statistics includes data analysis related to the uncertainties of huge amounts of data (Davis, 2002). The first part of this study will involve graphical views such as Histogram, Probability Density Function (PDF), and Cumulative Distribution Function (CDF), as well as the interpretation of the center, location, variability, and shape of the distribution beside analyses of the mean, median, standard deviation, minimum, maximum values, and coefficient of variation. This will lead to interpret patterns of the population (e.g. distinguishing normal and non-normal distributions).

Interpretation and analysis of uncertainties that are related to limited sampling plans over a spatial domain require a special tool, such as geostatistics. This is different from classical statistics, geostatistics does not assume the model of a population distribution in which all samples are assumed to be normally distributed and being independent on each other (Zhang, 2011). Since most measured data in Earth Science and geological information do not fulfill the statistical assumption of normality and independence, geostatistics is widely used to analyze spatial data where the relation between close-by space points is usually different from data at points further apart. Geostatistics incorporates the statistical distribution of data with the spatial relation between these data.

**Semivariogram**

Matheron 1967 defined the semi-variogram function which describes the spatial correlations of any substantial random spatial function as:

$$\gamma\,(h) = 0.5\ \mathrm{Var}\,[Z(x + h) - Z(x)]$$

*Assuming that the mean value of Z(x+h) – Z(x) is zero, then γ represents the half of mean square of this difference:*

$$\gamma\,(h) = 0.5E[Z(x + h) - Z(x)]^2$$

Arithmetically, the construction of the semivariogram can be described as following (Sarma, 2009):

- Start at 0 [ $h = 0$, $Z(x + h) = Z(x)$ ]
- Generally it increases with *h.*
- Continuous increasing up to a definite level which is called "*Sill"*, and the flattening out (bounded semivariogram), however in some cases it could keep rising (unbounded semivariogram) (Figure 3-6).

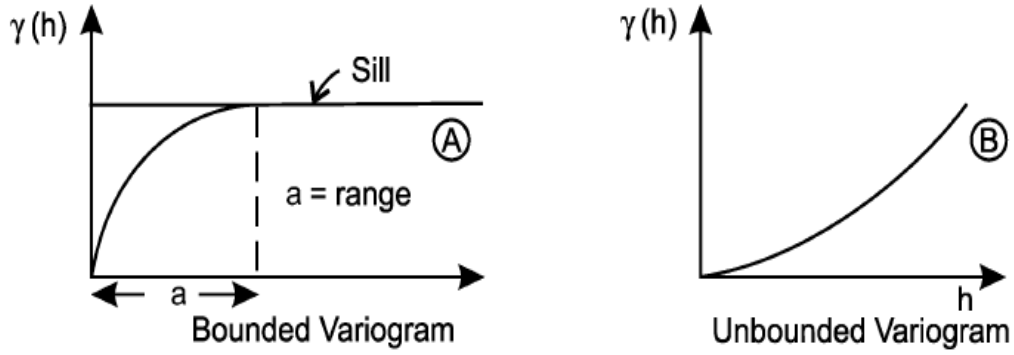


Figure 3-6: Schematic bounded (A) and unbounded (B) semivariograms (Sarma, 2009)

The semivariogram is commonly utilized to address the spatial variability and continuity evaluation of the variable under study, the majority of geostatistical processes and simulations need analytical semivariogram models. These semivariogram models can ease the understanding of behavior, continuity, and geometry of the investigated variable

Semivariogram analysis includes two processes; the first step is to build the experimental semivariogram of data sets as an averaging process with specific distance separation and direction, then plotting the output variability results in two-dimensional view. The second step is the fitting of the experimental semivariogram with a number of mathematical model functions to come up with spatial correlation by choosing the best and most suitable matching between the mathematical function and the experimental semivariogram.

**The properties of semivariogram**

[1] Sill value ($C_0$+C): A point from which the semi-variance will not increase anymore producing a flat behavior (stable) where the semi-variogram equals the variance (S) around the mean value of the dataset; represents the value at which the semivariogram levels off (Bohling, 2005).

[2] Range: The distance to a threshold value of the variance (sill) after which the variance shows constant value (plateau) after corresponding increase of square average difference due to increase in pair distance (Bohling, 2005).

[3] Nugget ($C_0$): Theoretically represents the zero variability at the origin (Bohling, 2005).

[4] Nugget effect: the vertical distance between the zero values to the smallest separation distance (Figure 3-7), this effect appears due to some factors such as sampling errors and short scale variability which lead to discontinuity at the semivariogram origin, hence the nugget value is not zero (Bohling. 2005).

*Relative nugget effect*: the percentage (ratio) between nugget effect and sill (Isaaks and Srivastava, 1989).

*Lag tolerance:* an arithmetic estimation to compensate for the irregularity in data distribution in order to obtain a logical number of pairs for computer statistics (Bohling, 2005).

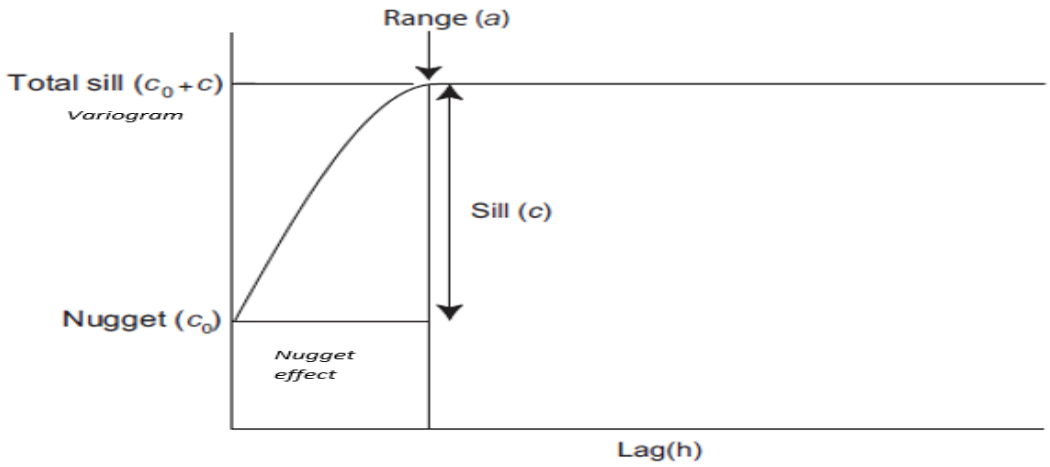


Figure 3-7: Semivariogram parameters where X-axis represents the separation distance between data pairs of one variable; Y-axis represents the lags variability (after Bohling, 2005)

**Semivariogram Estimation**

In semivariogram estimation, the semivariance is computed for pairs of data that fall inside some specific bands with specific direction (directional semivariogram) and limited lag distance (h), these bands are identified by a known band width, angular tolerance, and azimuth direction (Figure 3-8).

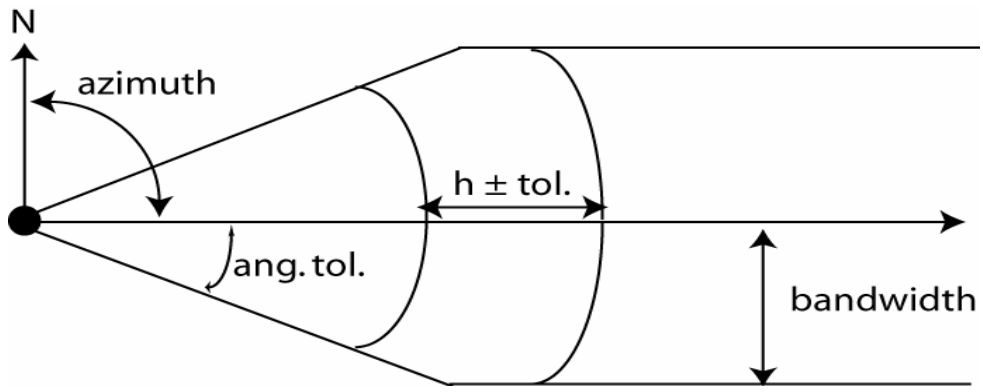


Figure 3-8: Sketch shows the methodology of estimating the directional semivariance (Bohling. 2005)

**Type of Semivariogram Models**

Semivariogram models are classified into two sets depending on the sill's presence or absence:

1- Transition models (models with sill).

2- Drift models (trends; models without sill).

**1. Transition models**

There are numerous types of semi-variogram models. However, the most common transitional type includes models of linear behavior at the origin (exponential and spherical models) and the parabolic origin behavior model (Gaussian model) (Figure 3-9).

The mathematical forms of the most often used model types (Bohling, 2005) are given below:

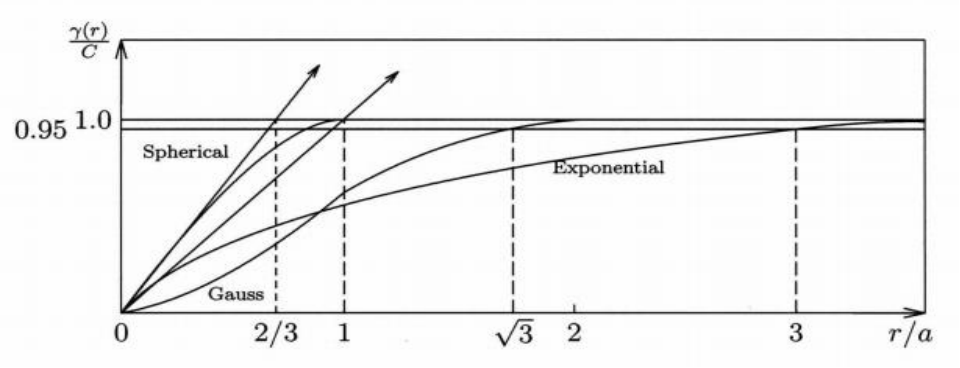


Figure 3-9: Representation of the three main transition models; the spherical, Gaussian, and exponential models with their Sill values, equivalent lag distances, and relation to the Range values (Bohling, 2005)

Nugget: $$g(h)=\begin{cases}0 & \text{if } h=0\\ c & \text{otherwise}\end{cases}$$

Spherical: $$g(h)=\begin{cases}c\cdot\left(1.5\left(\frac{h}{a}\right)-0.5\left(\frac{h}{a}\right)^3\right) & \text{if } h\le a\\ c & \text{otherwise}\end{cases}$$

Exponential: $$g(h)=c\cdot\left(1-\exp\left(\frac{-3h}{a}\right)\right)$$

Gaussian: $$g(h)=c\cdot\left(1-\exp\left(\frac{-3h^2}{a^2}\right)\right)$$

Power: $$g(h)=c\cdot h^{\omega} \quad with\ 0<\omega<2$$

where: **a:** practical range value, **c:** sill value, and **h:** lag distance.

## 2. Drift models:

The no-sill models are corresponding to random functions that cover unlimited spatial dispersions of data (Figure 3-10); the variance and co-variance cannot be defined, the drift model includes two types (Clark, 2001):

I. Linear model (the simplest): $\gamma(h) = ph$

Or generalized as: $\gamma(h) = ph^{\alpha}$ $\alpha \in (0, 2)$ **and not equal 2**

$p \approx$ slope of the line

II. Logarithmic de Wijsian model: the linear semi-variogram is plotted against logarithmic distances.

$$\gamma(h) = 3\alpha \log_e(h)$$

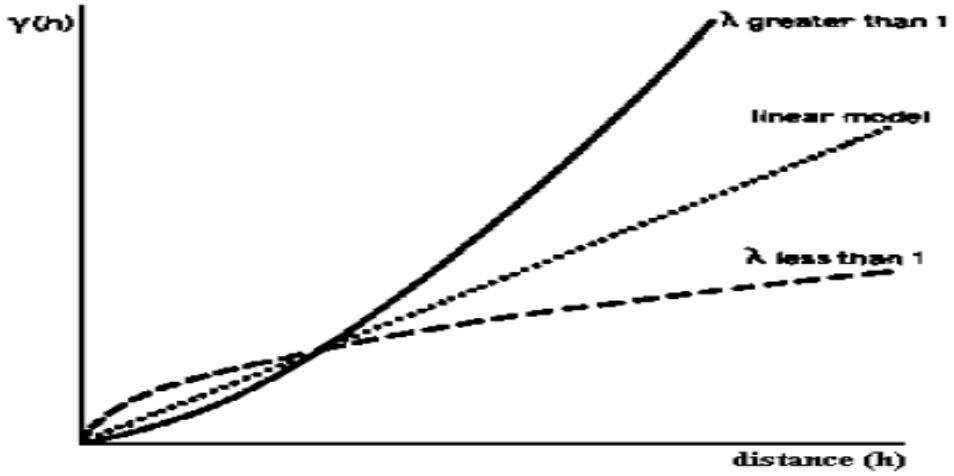


Figure 3-10: linear drift model (Clark. 2001)

**Kriging**

Most geostatistical estimations can be performed through two steps: the first step is to build the suitable semivariogram model, which models the difference simply between two values, in separated two locations depending on the separation distance and direction between them, the second step is estimation of the values at unsampled locations by kriging method; the basic and most common type is the ordinary kriging. Kriging as a

term refers to Danie Krige (1919 - 2013). In geostatistics, Kriging can be defined as a spatial interpolation method by which the neighboring unknown values can be derived from the measured weighted values. The Kriging is a technique that is always associated with an acronym written as (B. L. U. E.) which derived from "Best, Linear, and Unbiased Estimator" (Isaaks and Srivastava, 1989); Kriging is "Best" since it works to optimally reduce the error variance ($o^2_R$), the linear behavior comes from the weighted linear combination used for the estimation of the available data set, kriging is "Unbiased" because it attempts to get the mean residual error ($m_R$) as close to zero as possible. The linear and unbiased behavior holds true to all other estimation methods, however the "best" is a kriging distinguishing - characteristic that not found in other estimators (Isaaks and Srivastava, 1989).

**The random function model and unbiasedness**

The random function model is used to decide how to weight the surrounding samples to give an estimate for the desired location which means the unbiasedness of the estimation. So for any unknown or inaccessible location the available weighted linear combination is:

$$\hat{v} = \sum_{j=1}^{n} w_j \cdot v$$

The error for any specific value estimate is the difference between the true value and the estimate (Isaaks and Srivastava, 1989).

$$Error\ of\ i\text{-}th\ estimate = r_i = \hat{v}_i - v_i$$

Then the error average for a population of k estimates:

$$Average\ error = m_r = \frac{1}{k}\sum_{i=1}^{k} r_i = \frac{1}{k}\sum_{i=1}^{k} \hat{v}_i - v_i$$

According to Goovaerts, 1997:

$$Z^*(\mathbf{u}) - m(\mathbf{u}) = \sum_{\alpha=1}^{n(\mathbf{u})} \lambda_\alpha [Z(\mathbf{u}_\alpha) - m(\mathbf{u}_\alpha)]$$

u ,$u_a$ : Vector location for point estimation (u) from neighboring known point ($u_a$).

n(u): the number of neighboring data points that are used for estimating $Z^*(u)$.

m(u),m($u_a$): expected mean values of Z(u), Z($u_a$).

$\lambda_a$(u): weight of kriging allocated to z($u_a$) datum to estimate point (u), the same datum will be considered with different weight when used for a different location.

Z(u) considered as random field with m(u) trend, and R(u) residual component where:

**R(u) = Z(u) – m(u)**

Kriging estimation for residual of (u) as summation weights of residuals at neighboring data points, the kriging weights ($\lambda_a$) are obtained from semivariogram or covariance function which should distinguish the residual factor (Bohling, 2005).

So the issue is to determine the point weights that reduce the estimator variance:

$$\sigma_E^2(\mathbf{u}) = \mathrm{Var}\{Z^*(\mathbf{u}) - Z(\mathbf{u})\}$$

According the unbiasedness constraint: **$E\{Z^*(u) – Z(u)\} = 0$**

The random field Z(u) is analyzed into trend and residual components, Z(u) = R(u) + m(u), the residual component treated as a random field with stationary mean of 0, and stationary covariance (function of lag h, not of position 'u'):

$$\mathbf{E\{R(u)\} = 0}$$

$$\mathbf{C_0v\{R(u),R(u+h)\} = E\{R(u).R(u+h)\} = C_R(h)\}}$$

The covariance residual function is mainly obtained from semivariogram model:

$$C_R(\mathbf{h}) = C_R(\mathbf{0}) - \gamma(\mathbf{h}) = Sill - \gamma(\mathbf{h})$$

Hence the feeding semivariogram should reflect the residual component of the investigated variable**.**

In Geostatistics, there are three major kriging variants those are: simple kriging, ordinary kriging, and trend kriging (Bohling, 2005). The current case deal with the ordinary kriging as an objective, so other variants will not be considered in the following discussion.

**Ordinary kriging**

In ordinary kriging, the assumption is about the mean is constant in whole domain can be replaced by assuming that the mean is constant in the local surrounding neighborhood of each estimated value, so, in such case the kriging estimator can be formatted as:

$$Z^*(\mathbf{u}) = m(\mathbf{u}) + \sum_{\alpha=1}^{n(\mathbf{u})} \lambda_\alpha(\mathbf{u})[Z(\mathbf{u}_\alpha) - m(\mathbf{u})]$$
$$= \sum_{\alpha=1}^{n(\mathbf{u})} \lambda_\alpha(\mathbf{u}) Z(\mathbf{u}_\alpha) + \left[1 - \sum_{\alpha=1}^{n(\mathbf{u})} \lambda_\alpha(\mathbf{u})\right] m(\mathbf{u})$$

**Basic steps for kriging:**

1- Select a kriging plan:

Determine the block size of estimation.

Determine the number of samples to be considered for kriging.

Find the modeled semivariogram parameters (model type, C, $C_0$, a, sill)

$C_0$: should be equal in all directions to reflect same random phenomena.

Sill values: to define the anisotropy factor based on the ratio between the major and minor ranges.

2- Setting up of linear simultaneous equations:

Mathematically (for illustration, consider a 2-point interpolation only):

$$\lambda_1\gamma_{11} + \lambda_2\gamma_{12} + \mu = \gamma_{01}$$

$$\lambda_1\gamma_{21} + \lambda_2\gamma_{22} + \mu = \gamma_{02}$$

$$\lambda_1 + \lambda_2 = 1$$

where: $\lambda_1$ and $\lambda_2$: assigned weights for $x_1$, $x_2$

$\gamma_{01}$ and $\gamma_{02}$: variogram value between $x_1$ , $x_0$

3-Kriging coefficient: estimates all spatial relations between points ($\gamma$).

Consider a spherical model:

$$\gamma(h) = C_0 + C[\,1.5(h/a) - 0.5(h/a)^3] \qquad \text{for } h < a$$

$$\gamma(h) = C_0 + C \qquad \text{for } h >= a$$

4- Answer the linear equations of step (2).

5-Calculation of the kriging and kriging variance.

$$[A] \bullet [W] = [B]$$

$$[A]=\begin{vmatrix} \gamma_{11} & \gamma_{12} & \gamma_{13} & 1 \\ \gamma_{21} & \gamma_{22} & \gamma_{23} & 1 \\ \gamma_{31} & \gamma_{32} & \gamma_{33} & 1 \\ 1 & 1 & 1 & 0 \end{vmatrix} \quad [W]=\begin{vmatrix} \lambda_1 \\ \lambda_2 \\ \lambda_3 \\ \mu \end{vmatrix} \quad [B]=\begin{vmatrix} \gamma_{V1} \\ \gamma_{V2} \\ \gamma_{V3} \\ 1 \end{vmatrix}$$

**Kriged estimate:** $Z^* = \lambda_1 x_1 + \lambda_2 x_2 + \lambda_3 x_3$

**Kriging variance:** $\sigma^2_k = \lambda_1 \gamma_{V1} + \lambda_2 \gamma_{V2} + \lambda_3 \gamma_{V3} + \mu$

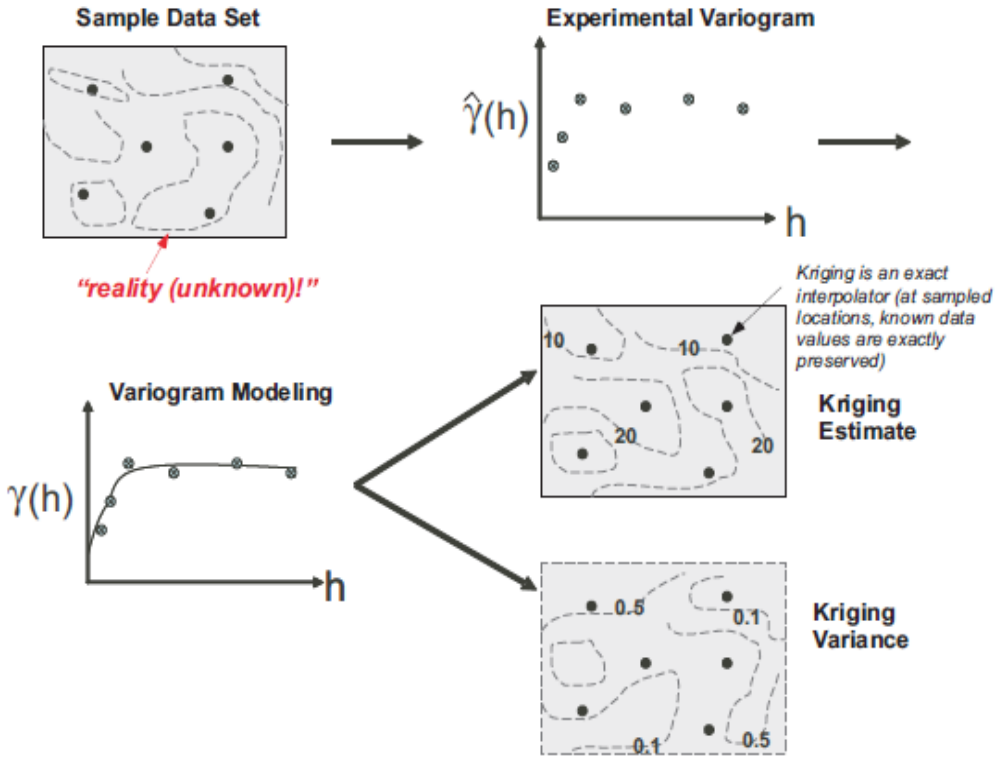


Figure 3-11: Diagram showing the kriging estimation work flow (Zhang, 2011)

**Simulation**

Stochastic simulation is a tool to generate several possible views of reality (realizations) with equal probability for the property or variable under investigation. Consequently, this approach is much better than just the estimates of the mean methods. Among geostatistical simulation there are two methods that are commonly used especially in reservoir modeling (Bohling, 2005), these are namely; Sequential Gaussian Simulation, and Indicator Gaussian Simulation. However, there are many other methods like turning band method, Simulated Annealing (SA), Boolean method, and LU decomposition. The Sequential Gaussian Simulation (SGS) it is mainly used for continuous variables such as porosity, permeability, and gamma ray, while, the Sequential Indicator Simulation (SIS) is commonly utilized for categorical variables such as facies distribution (Eltom *et al*., 2012). Yet, the same basic algorithms are used for both sequential simulation methods.

The conceptual idea beyond the sequential Gaussian simulation is straightforward, the kriging provides an estimation of both the standard deviation and mean of the variable in any grid node, which implies that the variable can be represented in each grid node as a Gaussian random variable. The sequential Gaussian simulation algorithm selects a random sample from this normal distribution rather than selecting the mean value as an estimate for each node.

The interpolation approaches usually generate one estimation for each location. In real world, there are many equally probable values that could be generated at every un-sampled location, in which the real value is unknown. The geostatistical simulation

generates multiple realizations or predictions that mimic reality (Isaaks, and Srivastava, 1989).

**Sequential Gaussian Simulation**

In this approach, at the unknown location the simulated value is controlled by the CDF (Cumulative Distribution Function), which is calculated from the observed and formerly simulated values in the vicinity of this location. The simulation process commonly begins with a location that is selected randomly, then progresses sequentially through the grid that represents the simulated area. However, the steps of the movement are not theoretically specified, instead they usually follow a random sequence (Isaaks and Srivastava, 1989).

Then, at every point or location, the program searches for the point values to be included in the calculation of the unknown point (s) in a predefined neighborhood (search radius). Those points may consist of both points that already had been simulated in previous steps, and points introduced as input data to the program. From these points, a probability distribution is calculated.

The sequential Gaussian Simulation approach calculates a conventional kriged estimate and variance from normal score transformed data (Eq.1). This method involves a single semi-variogram model based on the data that have been transformed. When the simulation at every intersection is finished, the result are transformed back to the original values (units) (Eq.2).

$$y_i = G^{-1}(C_i + C_{i-1}) / 2 \quad \text{…….. (1)}$$

$$Z_i = F^{-1}(G(y_i)) \quad \text{…….. (2)}$$

where: $G_{(y)}$ is the standard normal Cumulative Distribution Function (CDF)

$G^{-1}$ is the corresponding standard normal Quantile

$C_i$ is the cumulative probability associated with $Z_i$

$F_{(z)}$ is the Cumulative Disribution Function (CDF) of the original data.

The whole technique can be described as follows:

1. Transforming the data values to be normally distribued (Gaussian). The most common method to acomplish this is the normal score transform technique.
2. Giving each of the un-conditioned cell values, to be equivalent to those at the adjacent conditioned cell.
3. Defing a random route across the field in a way that every un-conditioned cell is visited only once.
4. Locating a predefined number of neighboring conditioning data for every cell across the random route. This may involve cells that had been simulated earlier, if they are selected to roughly conform to the semi-variogram's ellipse model range.
5. Executing ordinary kriging by using the data at the surrounding vicinity as conditionig points. This step will determines the Gaussian (normal) distribution mean (kriged estimate) and the point variance (variance from kriging estimation). Thus, the CDF will be known as the variance and the mean would completely determine a normal distribution.

6. Drawing a randum value from the distribution (CDF), which willl become a conditioning datum for the folowing drawing. This value is realized by a Quantile value $z=q_{(p)}$, which is corresponds to a random value p distributed uniformly between 0 and 1.

$$\mathbf{z = q\,(p) \longrightarrow F^{-1}\,(p) \qquad F\,(z) = F\,(q\,(p)) = p \in [0, 1]}$$

7. Newly simulated data are now added to the set of the known (or simulated) data, and we proceeds to the following cell until all the cells get assigned a simulated value.

**Sequential Indicator Simulation**

Theoretically, the Sequential Indicator Simulation (SIS) is similar to the Sequential Gaussian Simulation (SGS), except using indicator kriging to construct the discrete cumulative density function (CDF) for the single categories, and then getting the node assigned a randomly selected category from the discrete cumulative density function (Bohling, 2005). The representation of a category variable as facies (Figure 3-12) can be represented as an indicator as following:

$$i(\mathbf{u}_\alpha; k) = \begin{cases} 1 & \text{if facies } k \text{ is present at } \mathbf{u}_\alpha \\ 0 & \text{otherwise} \end{cases}$$

Hence, one indicator of any variable (facies) is assigned to each *K* different facies.

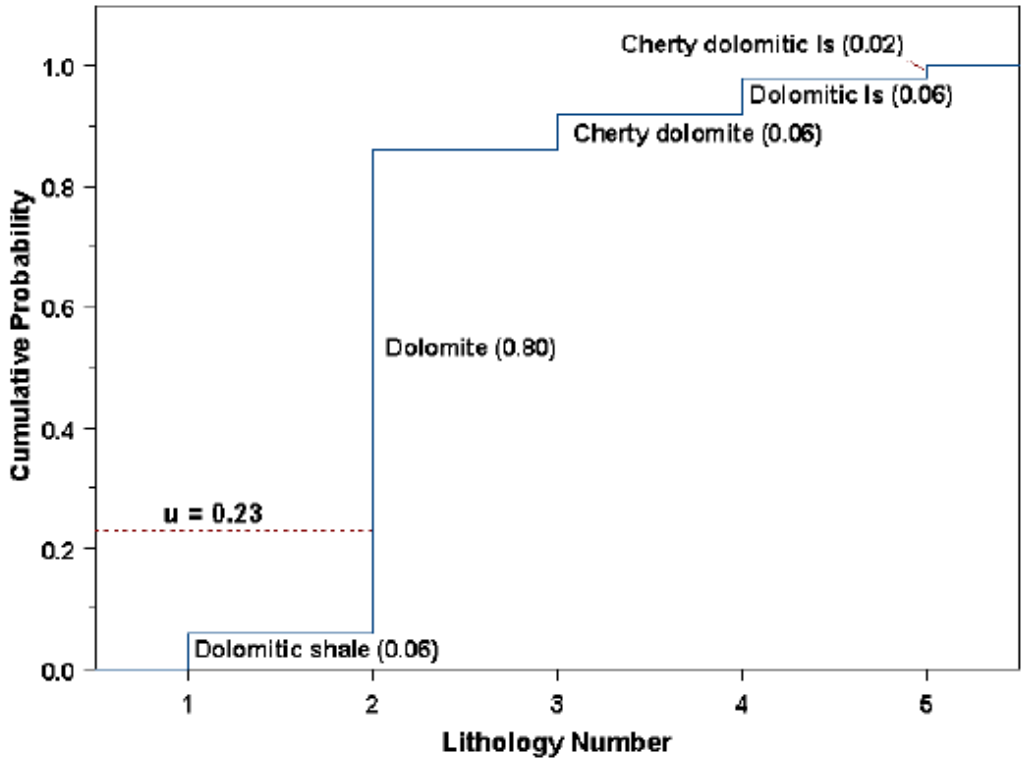


Figure 3-12: Probabilities of facies membership based on indicator semivariogram and their equivalent CDFs (Bohling, 2005)

For continuous variables like permeability, the indicator variables are constructed by comparison of data values to set of different thresholds, these thresholds for example can be defined as percentiles of the distributed data ($10^{th}$, $25^{th}$, $50^{th}$, …).

$$i(\mathbf{u}_\alpha; k) = \begin{cases} 1 & \text{if } z(\mathbf{u}_\alpha) \leq z_k \\ 0 & \text{otherwise} \end{cases}$$

# CHAPTER 4

# LITHOFACIES FRAMEWORK

## 4.1 Introduction

Better reservoir characterization requires a detailed facies description as an essential framework for further properties modeling. The outcrop under study composes of maximum of 19 m thick of mixed carbonate-siliciclastic sedimentary successions. Due to the heavy eolian sand cover and differential weathering, the Dam Formation is not fully exposed especially in the lower part of the studied outcrop. However, the main outcrop body is fully exposed (Figure 4-1). Genetically, the precipitation of carbonate deposits of the Dam Formation is predominated by abiotic producers (mostly marine micrite and minor evaporites), and biotic producers which include autotrophic cyanobacteria producers (stromatolite), and heterotrophic producers (mostly mollusks with less foraminifera), in addition to the non-skeletal grains (mostly ooids and peloids). The outcrop can be divided into two parts; the talus-dominated sequences of carbonate rocks in the lower part, and the main outcrop body which is composed of mixed carbonate and siliciclastic rocks (Figure 4-1). The siliciclastic units occurs in the lower successions of the main outcrop body, however carbonates are the most represented in the study area. This chapter includes the detailed description of lithofacies of the Dam Formation in a composite section. In addition to that, taking into consideration the heterogeneity that might be found along the exposure, with more concentration on the lithofacies that

represent most appropriate reservoir-prone according to petrographic studies of different lithofacies representations. This task was conducted using field description, high-resolution outcrop photograph, high-resolution slab photos, and thin section petrography stained with Alizarin Red using the procedure of Dickson, 1966. Carbonate texture classification was conducted based on Dunham classification (Dunham, 1962).

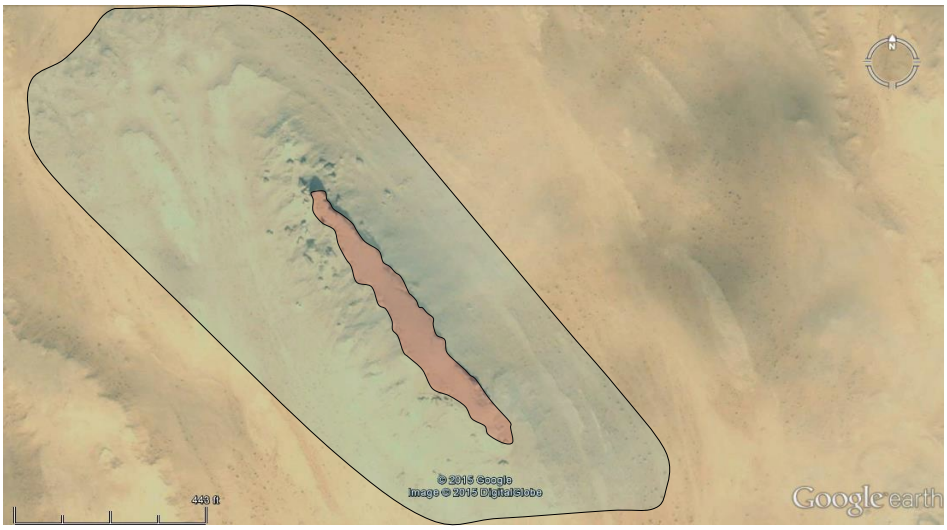


Figure 4-1: Google earth image shows plane view of the study area, the transparent red color area represents main outcrop body, and the transparent blue is the periphery successions (talus- dominated)

## 4.2 Lower Part of Dam Formation in the study area

This part is composed of six coarsening and thickening upward cycles of carbonate sequences, the sequences is exposed in only few locations in both sides of the outcrop, with best exposures at the northwestern part (Figure 4-1, Enclosure 4-2).

### 1- Sandy mudstone (D10-1) and skeletal packstone (D10-2)

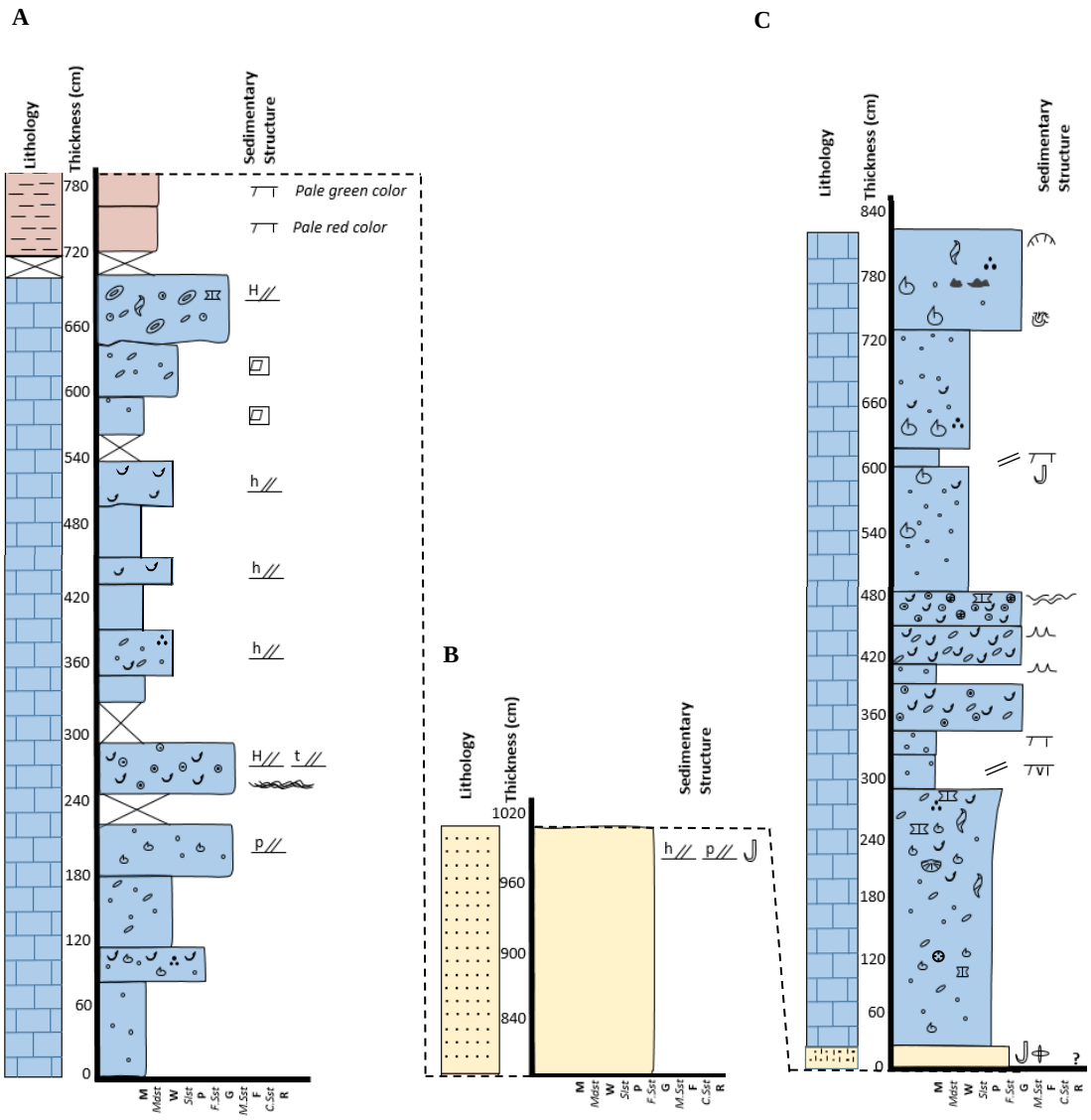


Figure 4-2: Composite section of the Dam Formation in the studied outcrop. A and B represent the talus-dominated area, C is the main outcrop body. See symbol key in the next page.

Basic Lithology

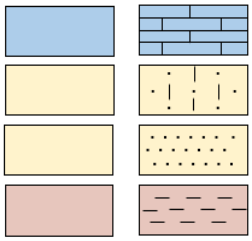


**M:** Mudstone (carbonates)

*Mdst:* Mudstone (siliciclastics)

**W:** Wackestone

*Slst:* Siltstone

**P:** Packstone

*F.Sst:* Fine-grained Sandstone

**G:** Grainstone

Composition/ Sedimentary Structure

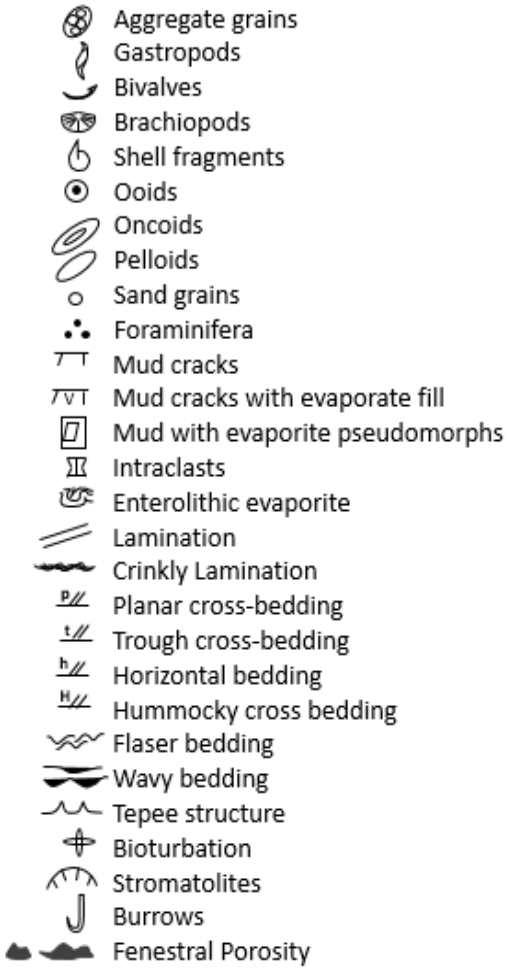

This lithofacies occurs at the base of the succession of Dam Formation in the northwestern part of study area. The unit composes of 80 cm of white color, loose, massive mudstone, with scatters of sub-angular to sub-rounded, moderately to well-sorted sand grains in micritized matrix. Fossil content is low (Figure 4-3).

The sandy mudstone is followed by skeletal packstone (D10-2). Comparing to D10-1, this unit contains richer fossil content. The skeletal components are mainly bivalves and broken shells and fragments which are mainly dissolved to form moldic porosity. Peloids commonly occurred in the moderately micritized matrix (Figure 4-3). The thickness is about 25 cm. The large size of skeletal grains besides the broken fragments and the peloidal content might indicate current energy. There are no bedding structures observed except the common orientation of bivalves along the horizontal stacking of deposition.

### 2- Peloidal wackestone (D10-3) and lithified sandy grainstone (D10-4)

The second cycle starts with relatively massive, white color wackestone (D10-3) with small size, elongated mud intraclasts, and moderate content of peloids (Figure 4-3B). Sand grains are dispersed unsystematically in this unit. Thickness according to top (D10-2) is 58 cm. Similar to the first cycle, this cycle is also characterized by coarsening upward pattern in which the peloidal wackestone grades into 30 cm thick of lithified and highly cemented, massive, sandy, peloidal, grainstone. Horizontal bedding is not clear due to high lithification and weathering (Figure 4-4C). The slab sample and thin section clearly showed calcite crystals filling some of the molds of bivalves and broken skeletal fragments (Figure 4-4D). The clasts are poorly sorted and poorly rounded. In addition, no preferred orientation was observed.

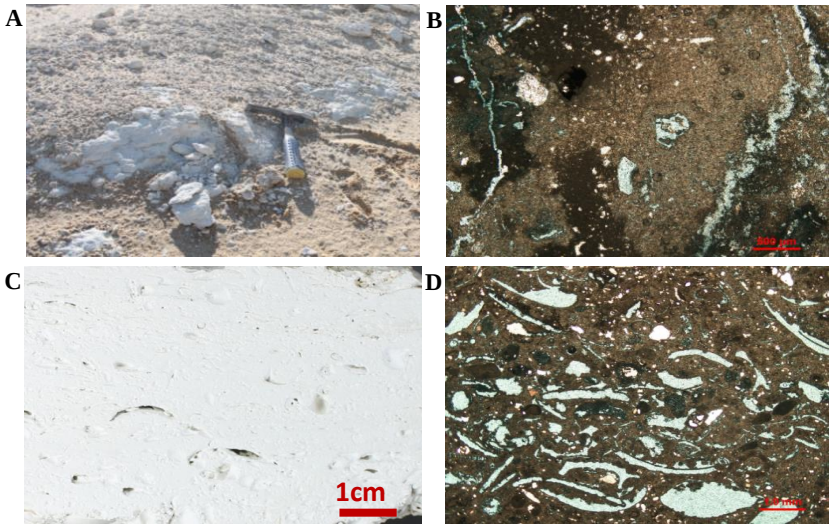


Figure 4-3: Sandy mudstone and skeletal packstone: representing sandy mudstone. A: The bottom-most exposed unit of the study area represented in sandy mudstone (D10-1). B: Thin section of same unit (notice channel porosity). Slab image (C), and microphotograph (D) of the skeletal packstone (D10-2) showing prominent moldic porosity of completely dissolved bivalves.

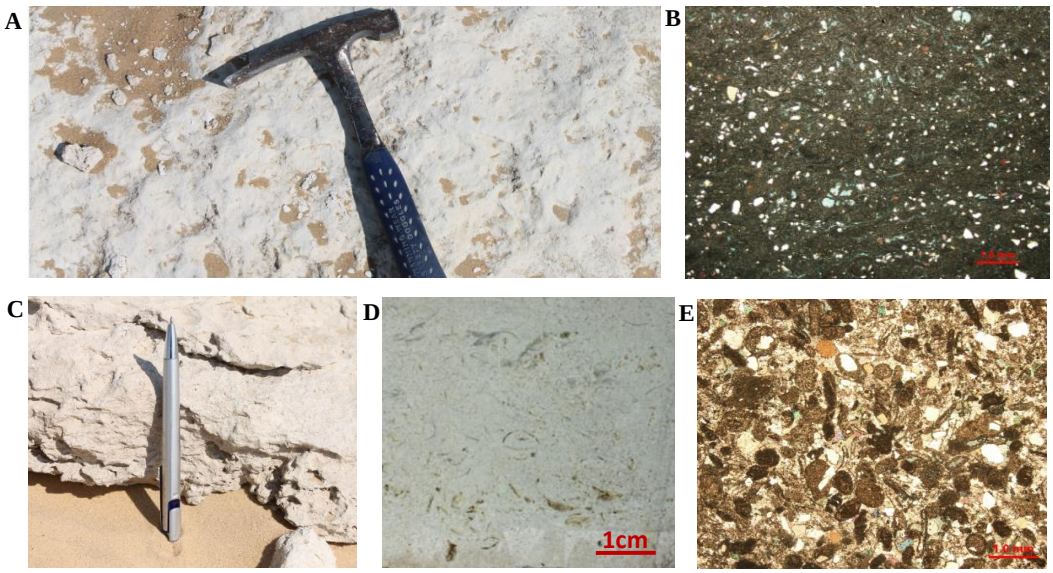


Figure 4-4: Peloidal wackestone-packstone and lithified sandy grainstone. Field view (A) and thin section (B) of massive peloidal wackestone-packstone (D10-3). Coarser component of the second cycle showing lithified texture of sandy grainstone (D10-4) (C), calcite filling in the upper part of slab photo (D), quartz and peloid grains (E).

### 3- Skeletal oolitic grainstone (D10-5)

The lower unit of this sequence, which might represent a mud-dominated or fine texture, was not detected in the outcrop. The exposed units (Figure 4-5A,D) are represented by planar cross bedded, skeletal, oolitic grainstone (35 cm). The skeltal fragments are mostly bivalves and broken shells of other mollusks which are dominant in the lower part (Figure 4-5A, E). The petrographic study also showed aggregate grains of ooids and coated grains. Bidirectional cross stratification indicates the asymmetrical ebb and tide currents. Since it is not common that ebb and tide have same velocity (Davis and Dalrymple, 2011), so that, there is a difference in surface angle of each of tide and ebb to the reactivation surface (Figure 4-5A). Thickness of the skeletal oolitic grainstone changes laterally due to changes in the ebb and tide energy, which also controls the bedding relationship along the exposure (changing from planar cross bedded to trough cross bedded and hummocky cross stratification) (Figure 4-5).

As lateral facies changes, this unit changes laterally into 25-30 cm of oolitic, peloidal, planar cross-bedded, coarse texture grainstone, with mud clasts and micritized shell fragments oriented parallel to the bedding surfaces. Porosity is up to 40%, mainly of intergranular type, with some intragranular, moldic ooid and moldic skeletal porosity, few species of foraminifera were observed with low density. In the eastern side of the far northwest area of outcrop periphery, the skeletal oolitic grainstone unit is associated with crinkly laminations of columnar-shape stromatolites (Figure 4-5G, H). The evolution of crinkly laminated columnar stromatolite is deformed and ceased by skeletal oolitic grainstone current as indicated by scouring bounding surface between the two units, that

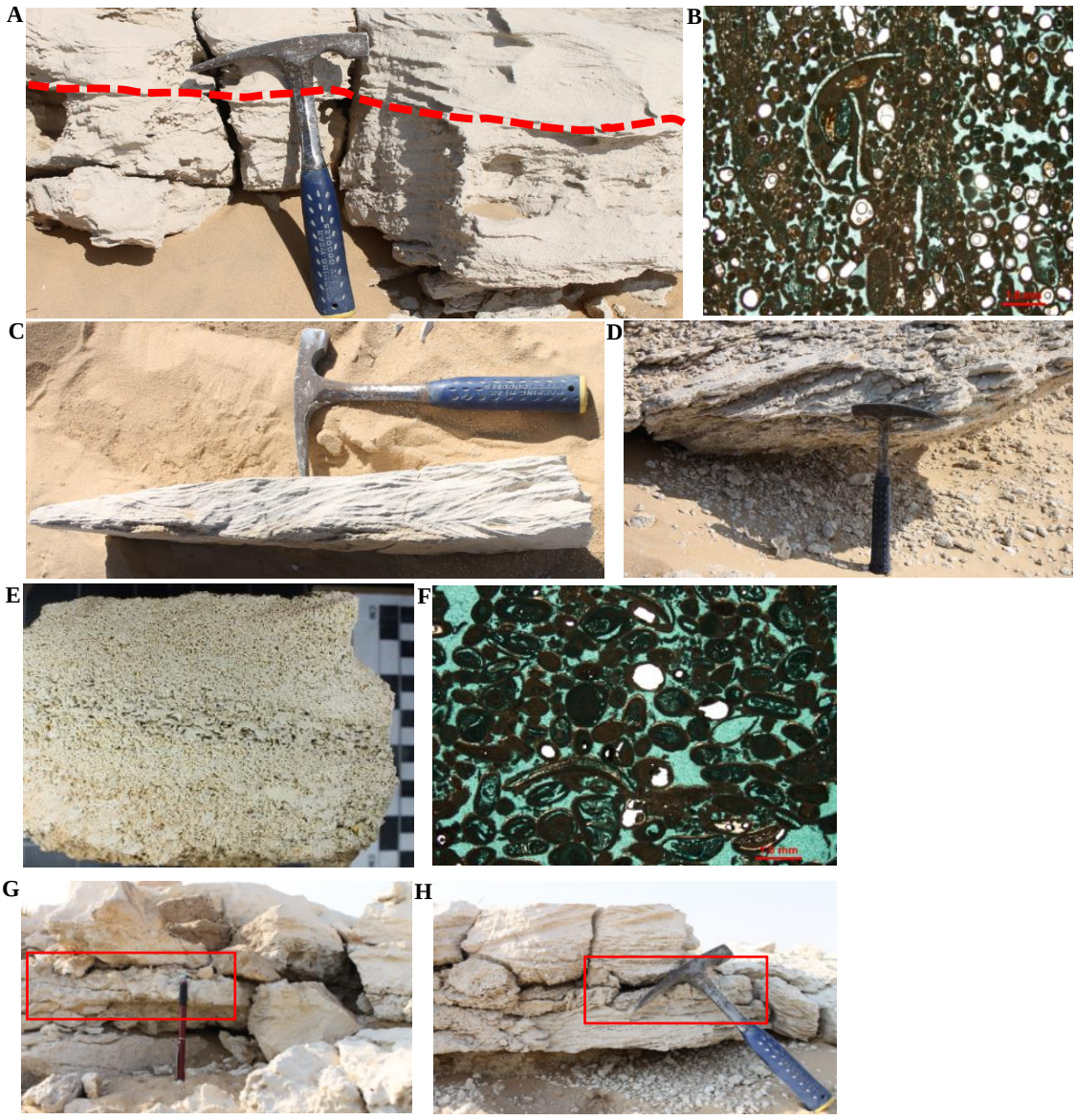


Figure 4-5: Skeletal oolitic grainstone: A: Reactivation surface (ebb and tide effect) in the skeletal oolitic grainstone (D10-5) and its microscopic photograph (B). C: well developed hummocky cross stratification in a broken block of same unit. D, E, and F represent lateral variation of (D10-5) into coarser, planar cross bedded, and more skeletal grainstone. G: Locally well- developed, and H: poorly-developed (deformed) crinkly-laminated columnar stromatolite (red rectangles), due to high energy current of skeletal oolitic grainstone, scale in (G) is 10cm.

led to formation of the poorly developed crinkly laminated-columnar stromatolite. (Figure 4-5H).

### 4- Cyclic mudstone-sandy wackestone sequence (D10-6)

The third sequence occurs as three cycles, each cycle starts with massive mudstone, distinguished by evaporitic pseudomorphs that form an external skin. This unit is topped and scoured by 20-30 cm of white colored horizontally bedded grainstone (C), dominated by fine grained, subrounded to subangular sand grains (40-50%) (Figure 4-6 A, B, C), quartz grains commonly occur as dispersed grains in the poorly micritized matrix, but also occur as aggregate grains bounded together by micrite film. Pellets, skeletal grains, and forams were slightly found.

### 5- Mudstone-wackestone and coated-grains grainstone sequence (D10-7,8)

The lower part of this sequence composed of 50 cm of massive mudstone carbonate with few scatters of reworked sand grains in micritized matrix. Size and density of clastic grains increased in the intercalated mudstone-wackestone of peloidal matrix. The lower part of mud-dominated carbonates is characterized by evaporite pseudomorphs (Figure 4-6 D) where the external surface is covered by evaporite skin, however no evaporites were observed in petrographic analysis. The coarser part of this sequence composed of 40 cm of oolitic, oncoidal, bioclastic, poorly cross-bedded grainstone. Coated grains are mostly of semi-ellipsoidal nucleus of elongated clast, some are dissolved nuclei. Gastropods were observed in thin section (Figure 4-6 H). This unit is scouring into the lower intercalated mudstone-wackestone facies (Figure 4-6 G). In the northwest face of the

outcrop, the planar cross bedding and its modification into poorly developed herring bone was detected (Figure 4-6 I).


Figure 4-6: The fourth and fifth sedimentary cycle. Prominent horizontal bedding of loose sandy wackestone (A), scouring into the lower mudstone-wackestone (B), dispersed quartz grains in a poorly micritized matrix of same unit (C). (D): Intercalation of mudstone-wackestone (E and F); notice the pseudomorph in the mudstone lens in (D). G: Scours of oolitic grainstone into lower mudstone-wackestone. H: Oncoids, semi-Ellipsoidal ooids, coated grains grainstone. I: Poorly developed herringbone cross stratification in a drop specimen of the scouring grainstone.

## 4.3 Main Outcrop body

The main outcrop body represents the best exposed sedimentary units of the study area. Mostly, all lithofacies are exposed in three dimensional NW-SE strike escarpment (Figure 4-1, Enclosure 4-2).

### 1- Estuarine sandstone (D10-9)

The sedimentary succession starts with Loose, fine grained, pale greenish brown color, horizontally bedded, to poor trough cross bedded, burrowed sandstone. The intensity of burrowing increases upward, with no evidence of borrowing noticed at the bottom of the unit. This unit exposed out in one location at the eastern face, and two locations at the western face, and the lower contact is exposed only in front of the northwestern edge of the outcrop, where the thickness of the fine grained sandstone is about 230 cm.

The extensive bioturbation (Figure 4-7A) indicates the tidal channel environment of this fine grained sandstone, since bioturbation is diagnostic feature to differentiate tidal channel deposits from fluvial deposits (Shinn, 1983).

### 2- Desiccated green mudstone (D10-10)

This lithofacies was observed as two types of morphologies (Figure 4-7), one occurs as a desiccated, thinly laminated, friable, dark green mudstone (Figure 4-7C), the other morphology is not different from the first one, however, the exception is about the invasion of upper unit (sandy fossiliferous packstone) coating the desiccated and caused the formation of mottles of the green mud (Figure 4-7D). Hand specimen of this unit showed weak reaction with 30% hydrochloric acid.

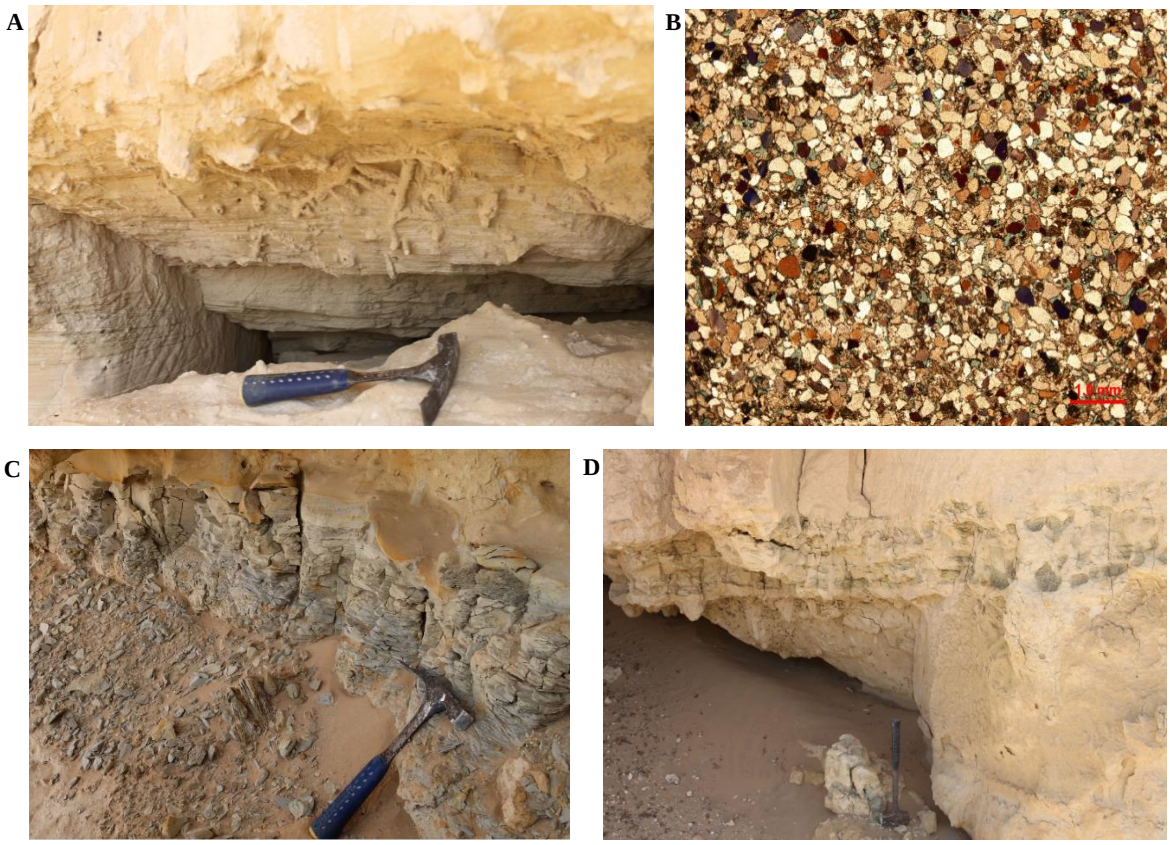


Figure 4-7: Estuarine sandstone and desiccated mudstone. (A): Pale greenish brown, burrowed, and horizontally bedded sandstone, (B): Thin section indicates moderately to well sorted, sub-rounded to rounded fine-grained sandstone, (C): Thinly laminated, desiccated mudstone, (D): Mottles of the same unit overlain and invaded by the calcareous sandstone and underlain by the fine-grained, loose sandstone.

### 3- Calcareous sandstone (D10-11)

This lithofacies represents a maximum of 173 cm thick bioturbated, greenish white colored calcareous sandstone, distinguished by trace fossils of skeletal fragments of different sizes scattered and mainly concentrated at the bottom of the unit. The bottom is also characterized by mottles of green mudstone (Figure 4-8C). The middle and upper parts of the unit are characterized by traces of bioturbation which increases upward.

Local occurrence of geoids of recrystallized silica. The calcareous sandstone is also characterized by trace imprints of worm activities, or gas bubbles escape, that might indicate supratidal flat environment according to (Shinn, 1983) or intertidal zone (Davis and Dalrymple, 2011). The dropped blocks of this unit reflects the intensive bioturbation at the top which made weak zones as shown in the internal surfaces (Figure 4-8A).

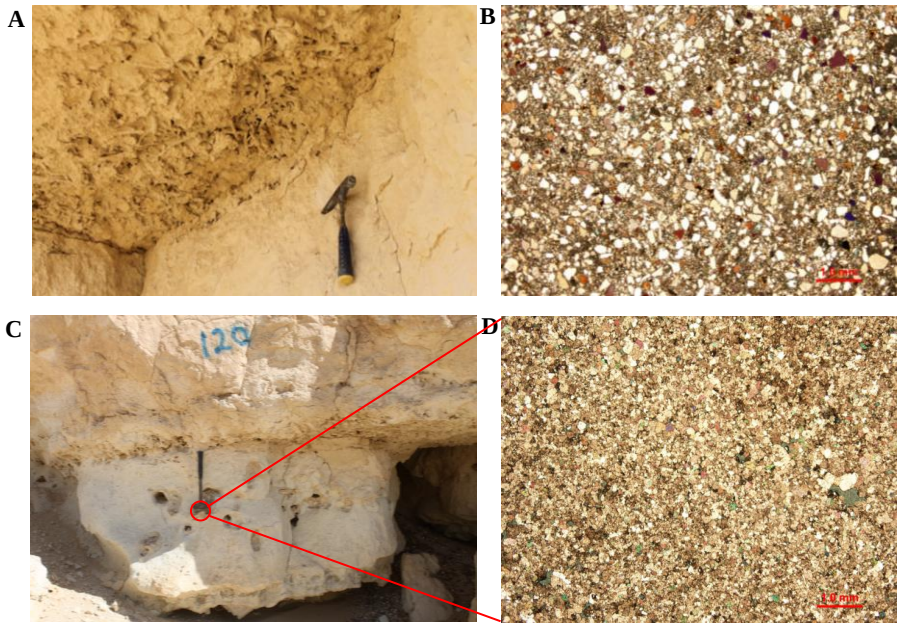


Figure 4-8: Calcareous sandstone: (A): Roof of borrowing networks at the top of calcareous sandstone, the intensive bioturbation led to block fall. (B): Photomicrograph of calcareous sandstone; note the micrite cement, (C): Local occurrence geoids, and (D): Photomicrograph of a silica geoid reflecting the finer texture of recrystallized quartz and siliciclastic grains.

### 4- Sandy fossiliferous packstone (D10-12)

This lithofacies is composed of maximum of 280 cm thick massive, sand grain-rich, fossiliferous packstone. In the middle and upper parts, the percentage of skeletal grains

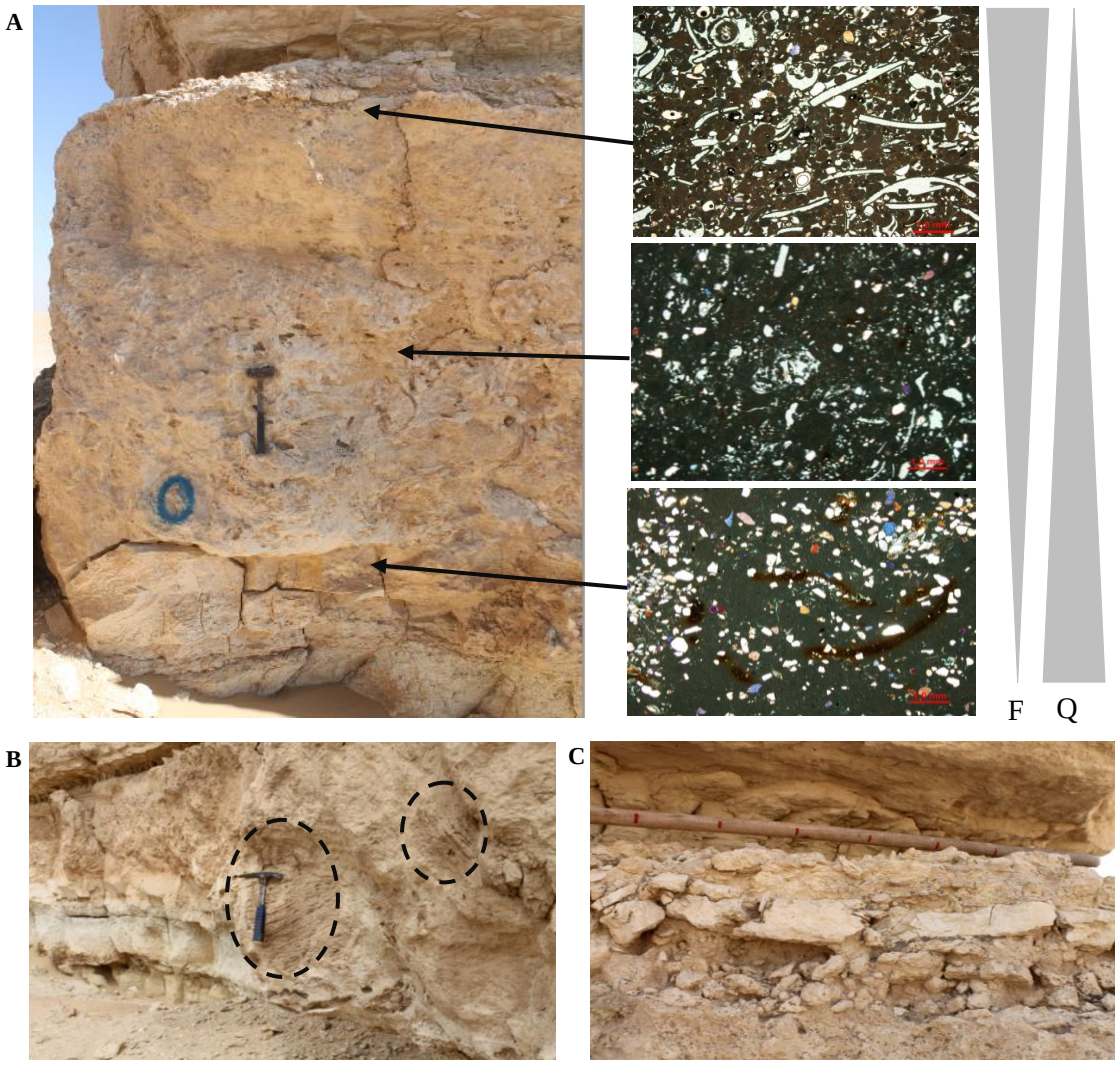


Figure 4-9: Sandy fossiliferous packstone. A: Three microphotographs (lower: D10-12A, middle: D10-12B, and upper: D10-12C) from massive sandy fossiliferous packstone (D10-12), where fossil content (F) increases upward in contrast with the quartz content (Q). B: Local-occurrence boulder of remnant reef (dashed circles) at the bottom of the unit. C: Heterogeneous mud intraclasts at the top of same unit; scale in 10cm.

increases respectively (Figure 4-9) indicating the coarsening upward sequence. This unit represents the first lithofacies that was selected for later porosity and permeability modeling. The fossil contents of this lithofacies include scatters of heterogeneous skeletal grains (bivalves, gastropods, brachiopods, and undefined broken skeletal fragments). Minor amount of non-skeletal content (peloids) present in the lower and middle parts, increasing significantly towards the top (Figure 4-9 A). This unit is also characterized by local occurrence of coral fragments (Figure 4-9 B), these fragments were also observed in the upper part of sandy skeletal packstone (D10-12C) in different sections through petrographic analysis. The top of this massive packstone is rich of heterogeneous sizes of mud intraclasts which are distinguishing this unit (Figure 4-9 C).

### 5- Polygonal dessicated mudstone (D10-13)

Approximately in the middle of exposed walls of the Dam Formation in the studied outcrop, a 35 cm of polygonal, desiccated, fissile, and thinly laminated green mudstone was deposited (Figure 4-10). This lithofacies was encountered also as muddy component of D10-6 with color difference, and also at D10-17. The bottom of this unit represents the fifth surface of the geometry model discussed in the next chapter. The petrographic analysis indicated that siliciclastic grains deposited in green glauconitic mud with fine micritized matrix. In some sections along the outcrop, the vertically oriented desiccation cracks were filled by evaporite threads as an early post-depositional (diagenetic) effect. This reflects the evaporation effect of the remnant saline water in a subaerial exposure after regression events. Mainly in upper intertidal and supratidal settings, the desiccation mud polygonal cracks are results of periodic exposure events of muddy flats (Davis and Dalrymple, 2011).

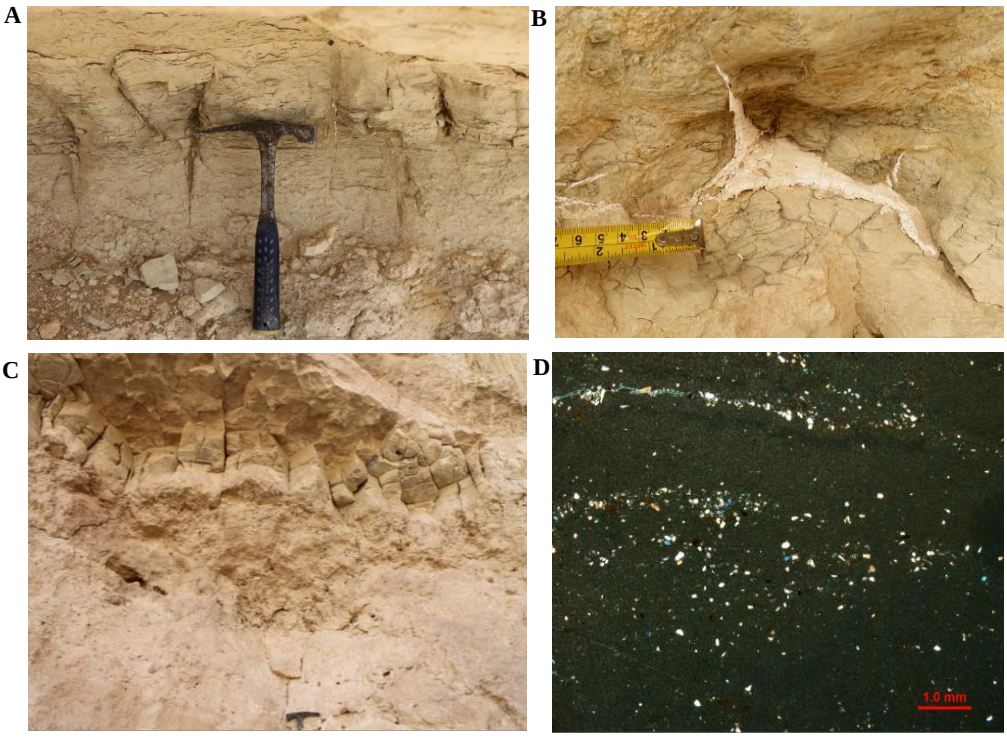


Figure 4-10: Thinly laminated, fissile, desiccation cracked-mudstone (A), cracks filled by anhydrites (B), 3D view of polygonal mud cracks (C), and photomicrograph of lime mudstone showing halos of quartz grains with slight preferred orientation (D).

## 6- Rhythmic mudstone-grainstone and rip up-clastic grainstone (D10-14, 15)

According to Reineck and Singh (1980), the lower intertidal deposits of highly-energized tide dominated coasts are composed of planar cross bedded peloidal/bioclastic-intraclastic grainstone that grade towards the land into heterolithic sand/coarse siltstone and mudstone with lenticular and flaser to wavy bedding. These rhythmic and heterolithic successions (rhythmites) are formed due to decrease in the energy of tidal current which can be translated into different sand/coarse silt to mud ratio towards the land. The

sand/coarse silt-size of grainstones deposited due to high ebb energy, while the muddy part was deposited as a result of current waning during slack periods (Davis and Dalrymple, 2011). In the Dam Formation, the rhythmite occurs as a tepee-structured succession of sandy mudstone and skeletal oolitic and peloidal grainstones (Figure 4-11B). The thickness of this unit ranges between 120 cm to 130 cm of amalgamated coarser components of skeletal oolitic grainstones, characterized by diverse fossil contents with indications of cross bedding (Figure 4-12), and finer mudstone with quartz grains and very low to no content of skeletal fragments (Figure 4-11). The basal unit composes of sandy micritized mudstone carbonates holding minor content of dissolved skeletal figments, followed by coarse bed of ooids, peloids, and skeletal grains (40%; mostly bivalves). The rhythmic stacking pattern is represented by these two units (Figure 4-11, 4-12, 4-13) which reflects reversed current energy and deposition mechanisms. The middle and upper mudstones are characterized by clear desiccation mud cracks which were injected by threads of evaporite in some sections (Figure 4-13). These Small scale polygonal mud cracks in the intertidal zone are associated with thin layers of coarser component of grainstone (Shinn, 1983), and can be easily identified along the outcrop wall faces (Figure 4-13). Quartz grains which are not diagnostic to these muds; are well sorted and sub-angular to well-rounded. The petrographic investigation indicated that quartz grains are randomly scattered and do not show clear orientation in most cases (Figure 4-11). Thus, wind-blown origin, or water carried-grains in a gentle slope platform are both probable. Initiation of the inverted “V” shape by the desiccated mudstone reflects that tepee structure is mostly formed as a result of desiccation and shrinkages of fine muddy components, and the latter coarser units (oolitic, peloidal, skeletal grains)

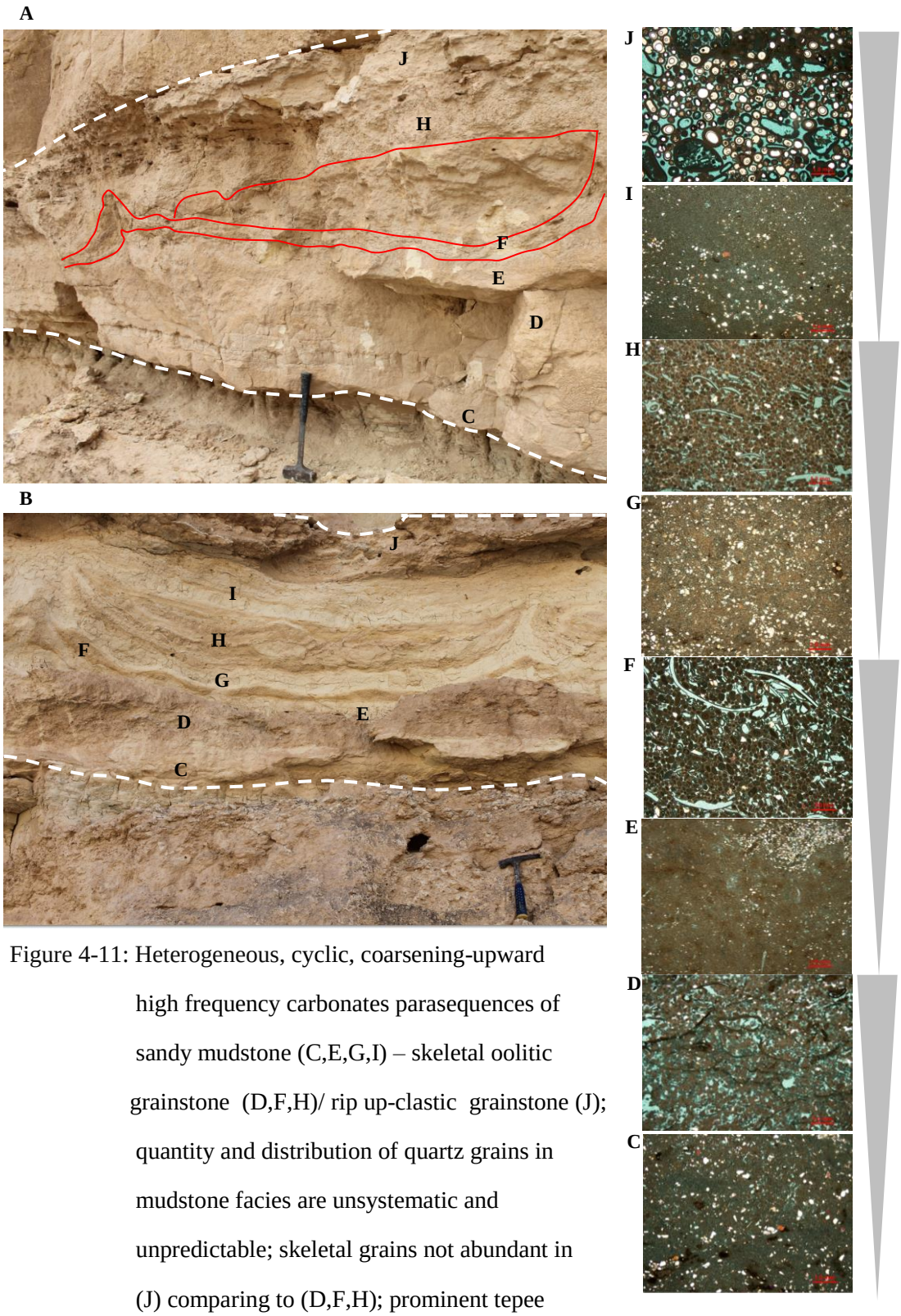


Figure 4-11: Heterogeneous, cyclic, coarsening-upward high frequency carbonates parasequences of sandy mudstone (C,E,G,I) – skeletal oolitic grainstone (D,F,H)/ rip up-clastic grainstone (J); quantity and distribution of quartz grains in mudstone facies are unsystematic and unpredictable; skeletal grains not abundant in (J) comparing to (D,F,H); prominent tepee structure in (A,B); scale (A):40 cm, (B):30cm

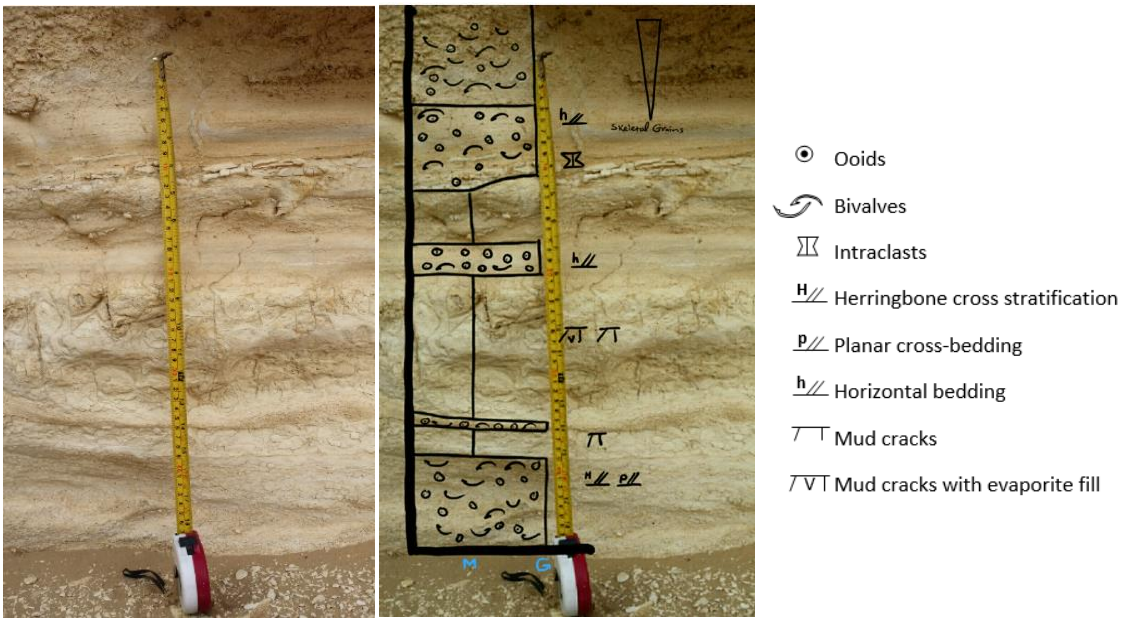


Figure 4-12: Local measured section of rhythmite sequence of mudstone-grainstone, note the herringbone to planar cross stratification at bottom indicating another stage of high frequent-flooding pulses

were deposited above the tepees. Tepee is a structure similar to an inverted V-shape, the name comes from American-Indian tents (Adams and Frenzel, 1950). Although these harmonic arrangements of inverted shapes are occasionally occur, and mostly formed irregularily (Pratt, 2002), the Dam Formation in Al-Nasbiyah Area included systematic, harmonic and well developed tepee structures (Figure 4-11B). These structures can be formed as a result of cementation, desiccation, thermal expansion, and crystal growth. Commonly, the inverted-V structures are found in peritidal deposition environment, and can be formed in the arid tidal flats or highly energized subtidal sediments due to contraction of partially lithified deposits (Kendall and Warren, 1987).

In general, desiccation mud cracks are not a distinctive features of tidal flats, they might also form in fluvial systems as flood plain deposits (Davis and Dalrymple, 2011). However, as mentioned earlier, these cracks are associated with evaporite minerals which invade and infill the cracks (Figure 4-13), this feature indicates the tidal flat environment regardless the depositional or diagenetic nature of evaporites.

### 7- Burrowed wackestone, desiccated mudstone, skeletal wackestone (D10-16,17,18)

The burrowed wackestone occurs as 160 cm thick, massive, sandy skeletal wackestone (D10-16). It is bioturbated and burrowed at the top. The surface of this lithofacies does not reflect any orientation or indicator for energized current deposition. At the top, the wackestone is characterized by moderate content of pale green color of vertical and horizontal burrowing networks (Figure 4-14). The petrographic study of this wackestone revealed a moderate content of skeletal fragments (bivalves, but mostly undefined broken shell fragments). The facies contains inclusions of moderattely to well sorted, subrounded to rounded quartz grains. These grains are not diagnostic and are found in most of lithofacies in the study area.

Conformably with deposition of 15 to 20 cm thick of green, cracked, dessicated mudstone took place (D10-17). The microscopic investigation showed micritized matrex, with moderate to low content of subangular to subrounded, moderately to well sorted quartz grains (Figure 4-15). The desiccation cracks are attributed to the lime content as a micrite matrix.

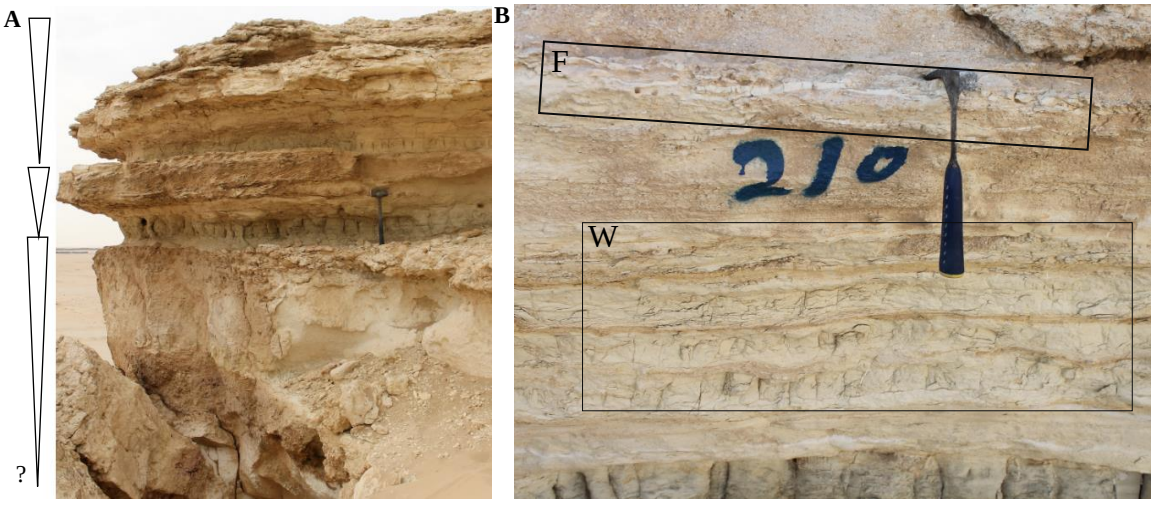


Figure 4-13: (A): Small scale coarsening upward parasequences of the rhythmite succession of finer mudy facies with coarser grainy facies (D10-14). (B) flaser bedding (F) of musdtone at the bottom of rip up-clastic grainstone (D10-15), and clear wavy lenticular bedding (W) in rhythmite layers. Note the evaporite injecting the muddy part in (B).


Figure 4-14: Burrowed wackestone showing bioturbation in: A: Hand specimen, B: Slabbed hand specimen; scale in 1 cm, and C: Thin section microphotograph

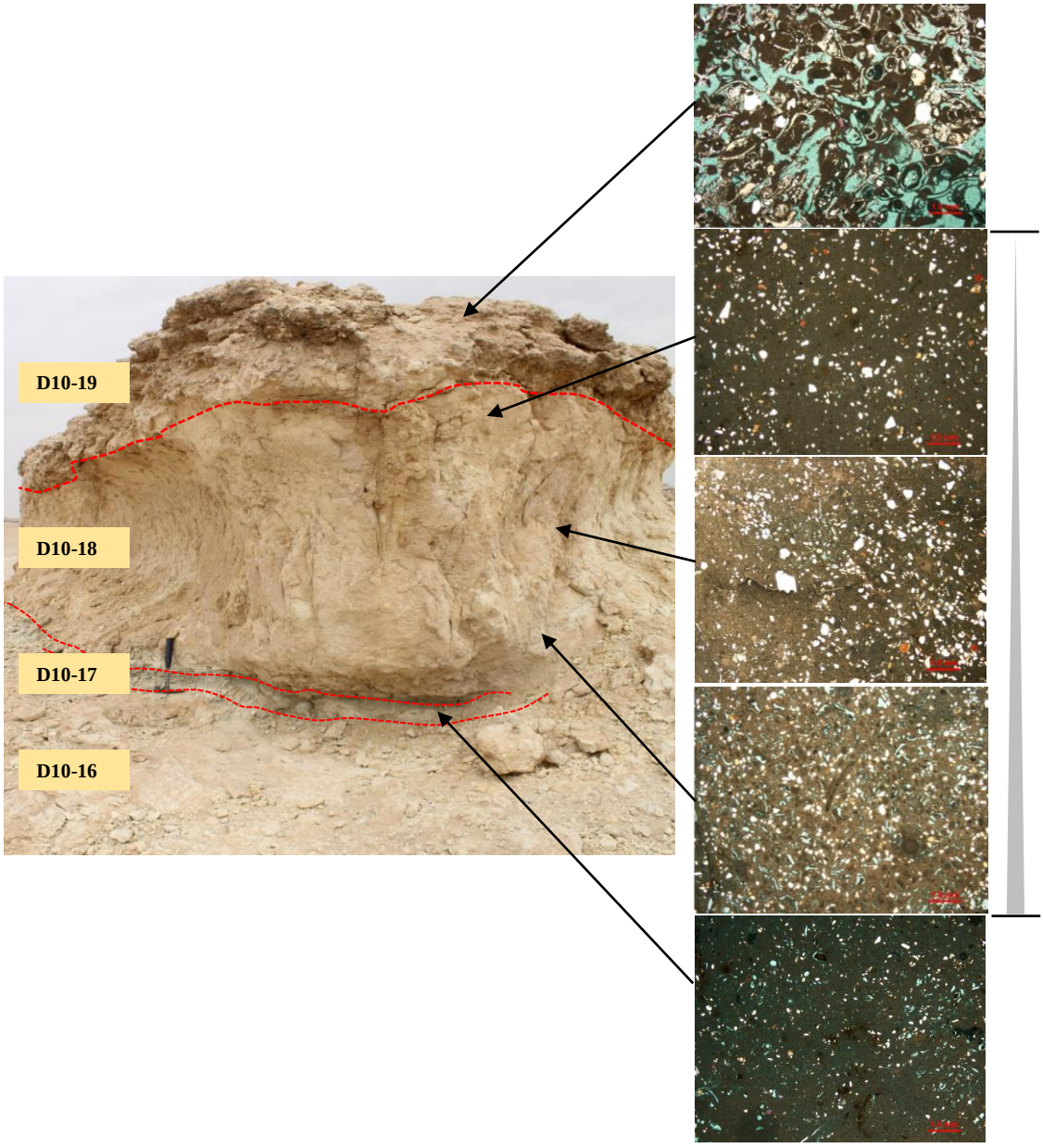


Figure 4-15: Field view of the four lithofacies of the upper part of Dam Formation in the studied outcrop, notice the domal cap of stromatolite (D10-19), and the fining-upward texture within skeletal wackestone indicated by fossil content

The desiccated mud is topped by 130 cm thick, massive skeletal wackestone (D10-18). Genetically, this wackestone is closely similar to burrowed wackestone (D10-16). The higher fossil content particularily in its lower part make it different from the burrowed wackestone (Figure 4-15), however, this difference does not affect the wacky texture. The dominance of undefined shell fragments in the lower part caused internal fining-upward grain size distribution (Figure 4-15). As expected, quartz grains distribution is unpredictable (Figure 4-15).

**8- Domal stromatolite grainstone (D10-19)**

Chronologically, this lithofacies represents the last unit of the Dam Formation exposed in the studied outcrop. It represents a domal shape (cap) of sandy skeletal grainstone. The thickness of this unit is around 90 to cm, and the thickness of microbial mats can exceed 1 cm thick (Figure 4-16A). Besides the presence of large scale domal stromatolites, the enterolithic evaporite structure (Ahr, 2011) or chicken wire (Shinn, 1983) which might indicate sabkha zone of high salinity water was also observed in some sections in the studied outcrop. Presence of siliciclastics and quartz grains, and fenestral porosity (Figure 4-16C, D) reflect the supratidal setting. Fenestrae (previously called “bird eye”) is an indicator of supratidal deposition, and can be as a result of: 1- shrinkage and expansions, 2- escapes of air during flooding, 3- formation of gas bubbles, or 4- wrinkling of algal mats (Shinn, 1968b). These fenestral structure can be filled by calcite or evaporites minerals. As shown in (Figure 4-16A), wrinkling of the stromatolite laminae created pore space between the stacked layers. This lithofacies was considered for further porosity and permeability characterization which will be discussed in the next chapter. Sandy components (quartz grains, sands) increases upward across the outcrop body, while sand

grains are absent or not abundant in the subtidal zone in the lower part of the outcrop (the small coarsening upward cycles). These grains are available upward, in the intertidal estuarine sandstone channel, or in the composition of the skeletal wackestone-packstone. The supratidal domal stromatolite grainstone contains evaporite components (Figure 4-16 B), and this could enhance the observed shallowing and coarsening upward which characterize the Dam Formation in the studied outcrop.

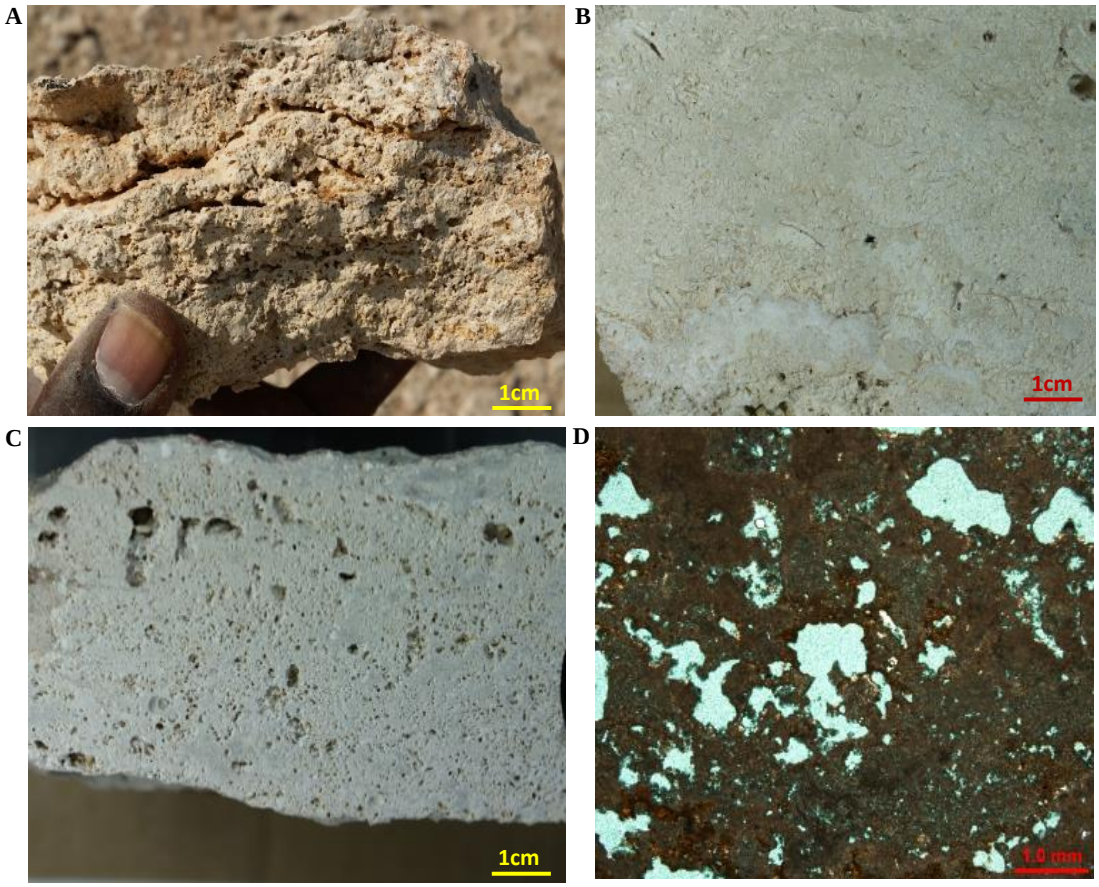


Figure 4-16: Stromatolite grainstone: A: Hand specimen shows domal structure of the stromatolite cap. B: Enterolithic anhydrite (chicken wire) in the basal part of stromatolite. C and D: Fenestral porosity

## 4.4 X-Ray Diffraction (XRD)

X-Ray Diffraction (XRD) analysis was conducted for only four samples of the Dam Formation in the studied outcrop. These samples represent the lithofacies selected for porosity and permeability analyses, which will be discussed in the next chapter. The XRD results showed that the selected lithofacies are dominated by dolomite minerals (Figure 4-17). This might indicate fabric preserving dolomite since dolomite crystals were not observed in petrography and SEM.

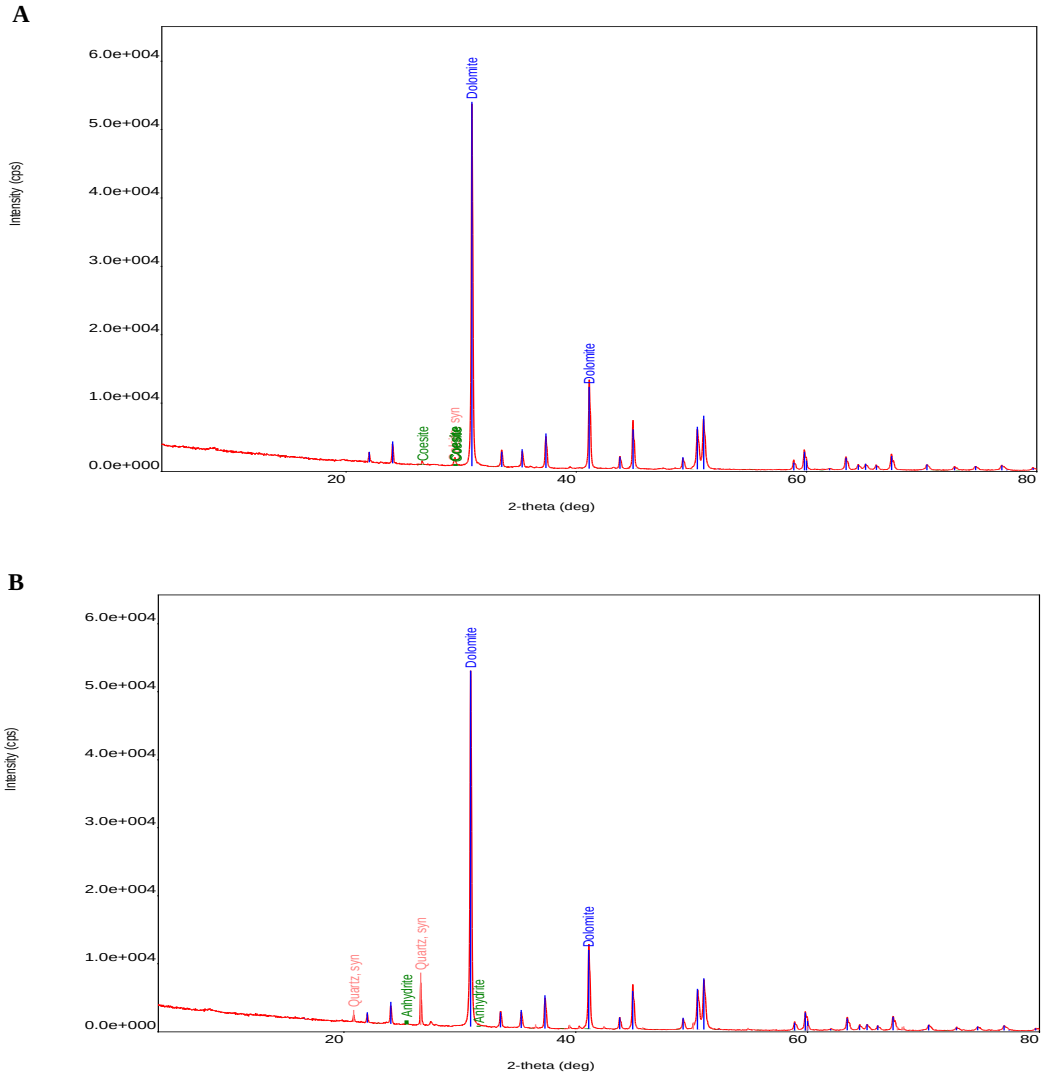

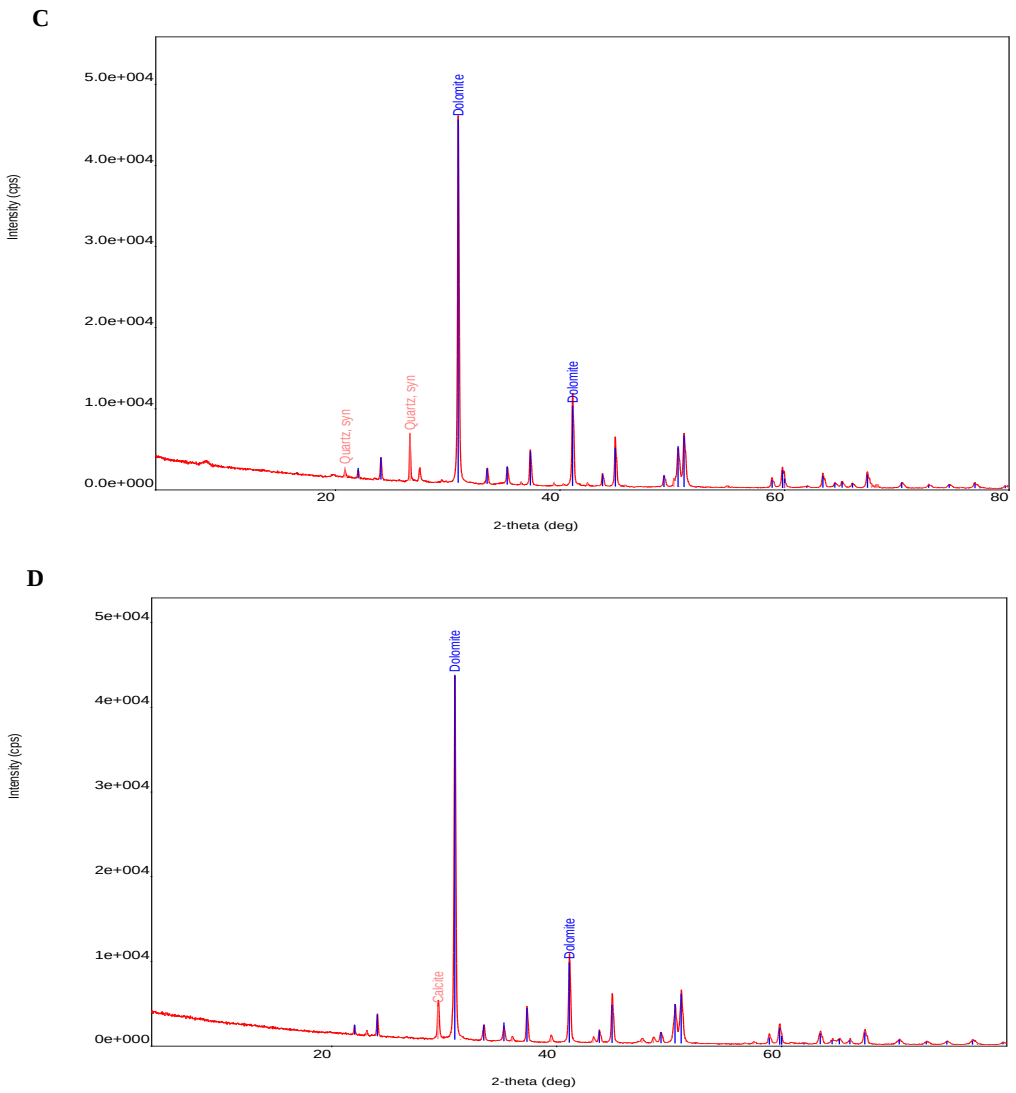


Figure 4-17: XRD analysis of the four selected lithofacies. A: Skeletal oolitic grainstone, B: Sandy fossiliferous packstone, C: Burrowed wackestone, and D: Stromatolite grainstone, note the dolomite peak in all lithofacies

## 4.5 Biocomponents of Dam Formation

Dam Formation succession in Al-Nasbiyah Area distinguished by diversity of biocomponents of skeletal grains, non-skeletal grains, and benthic foraminifera associations. These fossils indicate the prevalence of shallow marine environment. Here below is some lights shed on some of the most represented biocomponents across different lithofacies in the studied outcrop (Figure 4-18).

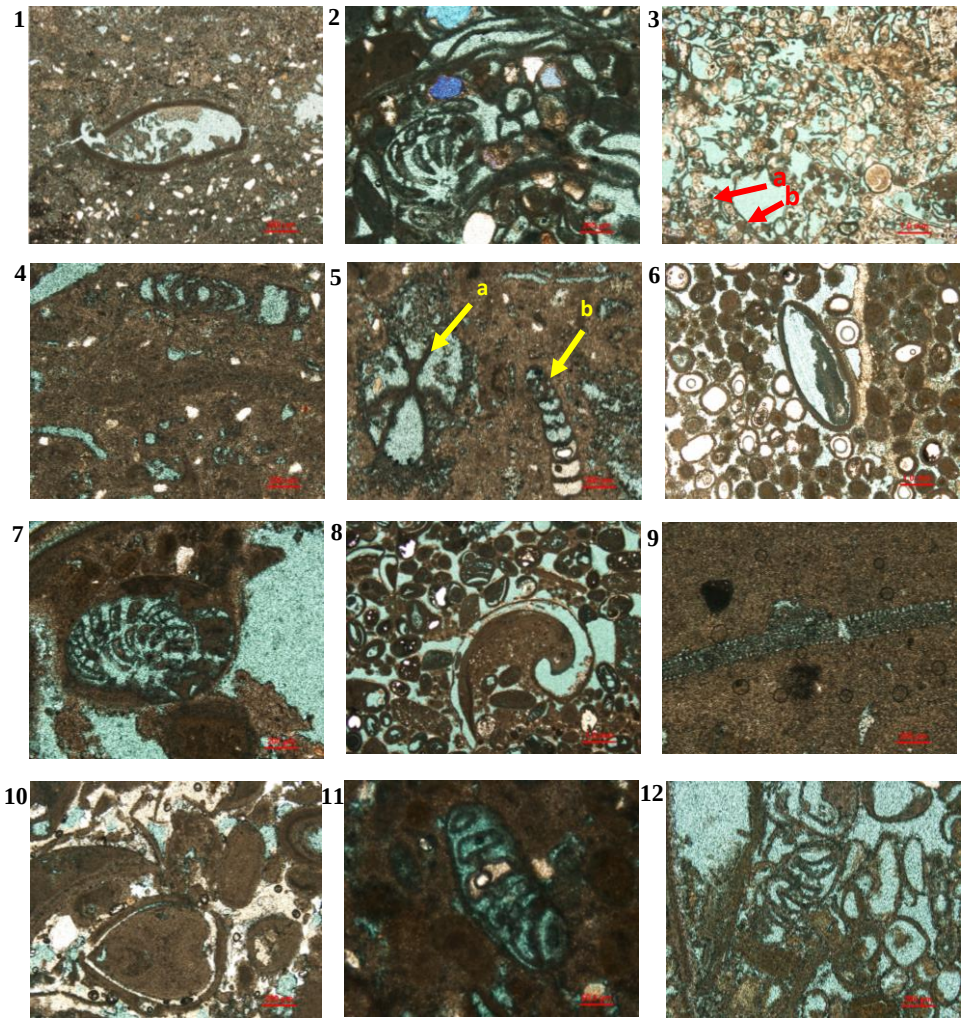

13 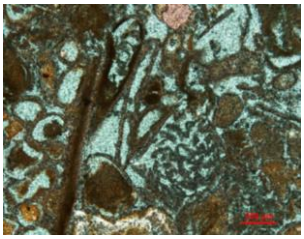

14 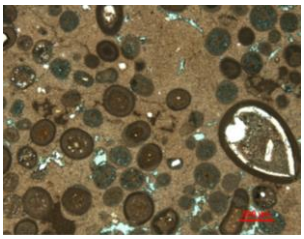

15 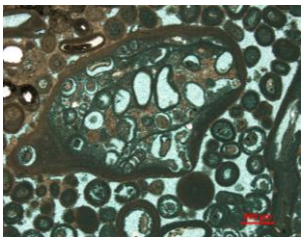

16 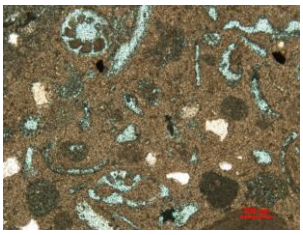

17 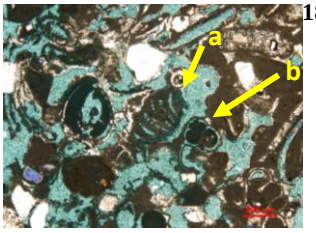


18 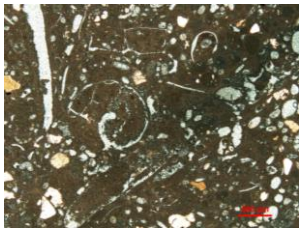

19 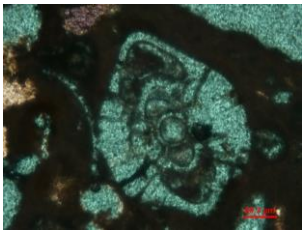

20 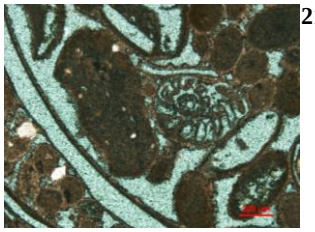

21 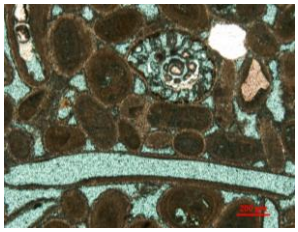

22 

23 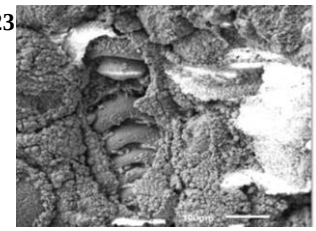

24 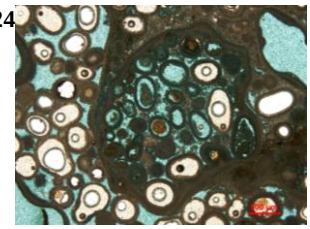

25 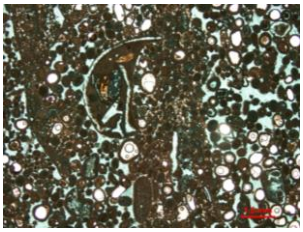

26 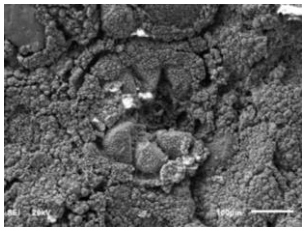

27 


28 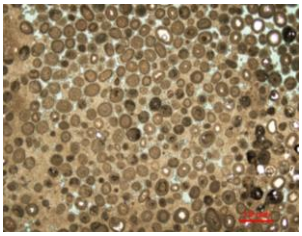

29 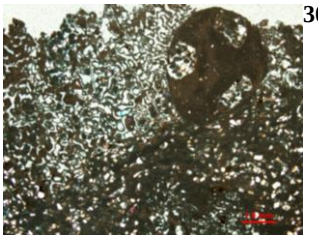

30 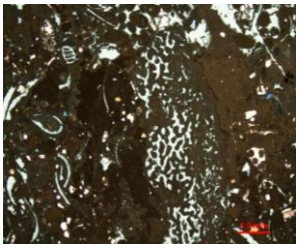

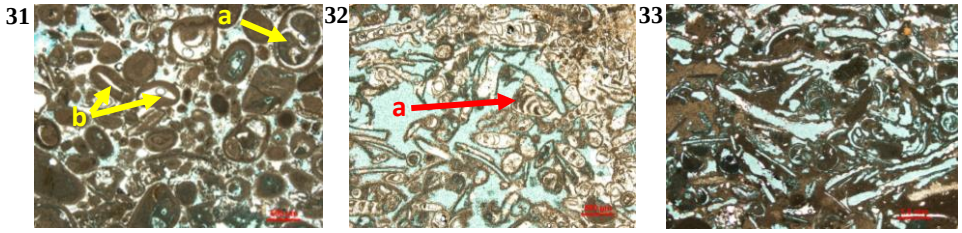


Figure 4-18: Most representative biocomponents of the Dam Formation in the studied outcrop:

1- Entire bivalve with micrite envelope (D10-3)

2, 7, 13, 16: Rotalid (*Ammonia sp.*) in different lithofacies (D10- 6, D10-12, D10-14)

2, 13, 19, 22, 26: Rotalid formainifera, 20, 21: spiral Ammonia *Rotalid Sp.* In different lithofacies (D10-6, 14, D10-18)

3- Diverse of foraminifera association: a: *Textularia sp.*, b: Coiled foraminifera (*Ammobaculites sp.*) in D10-19

4- Miliolid formainifera in D10-3

5- a: Coiled foraminifera *(Monalysium sp.)*, 5b, 23: Uniserial foraminifera (*Calvulina sp.*) in D10-3

6- Cross section across "uncommon" cephalopod coated by micrite envelope in D10-5.

8- Broken shell of brachiopod in D10-5

9- Broken fragment of *Archaias Hensoni* in D10-7A

10- Entire bivalve in oolitic in D10-8

11- Rotalid *Elphidium sp.* in grainy units of D10-14

14- Entire bivalve and ooids in micritized matrix in peloidal oolitic grainstone in grainy units of D10-14

15- Grapestone in D10-15

17- a: *Peneroplis sp.* Foraminifera, b: planktonic foraminifera (Lower Miocene) in D10-19

18- Gastropod in D10-12C

24- Aggregate grain in D10-15

25- Dissolved bivalve, coated grains in D10-5

27- Coated grains and leashed intraclasts in D10-15

28- Well-sorted ooids in D10-14F

29, 30- Coral fragments in D10-12C

31- a: Gastropod cross section, b: Oncoid and coated grain in D10-8

32- Diverse foraminifera, a: *Peneroplis sp.* in D10-19

33- Hetero-skeletal fragments, echinoid spines in D10-19

Enclosure 4-1: Summary of main characteristics of the different lithofacies in the studied outcrop

| **Lithofacies No.** | **D10-1** | **D10-2** | **D10-3** | **D10-4** | **D10-5** |
|---|---|---|---|---|---|
| **Lithology** | Carbonates | Carbonate | Carbonate | Carbonates | Carbonate |
| **Color** | White to greyish white | Bright white | Bright white | Dusty white | Paige, yellowish white, white |
| **Composition** | Subangular to subrounded, poorly sorted quartz grains of fine to medium grain size (15%), skeletal fragments, micritized matrix. | Fine grained sand and quartz grains, rounded to subrounded, skeletal fragments, bivalves, foraminifera. Micritized matrix | Quartz grains; subangular to subrounded, poorly sorted, peloids, very thin, elongated mud intraclasts | Intraclasts, skeletal grains, coated grains (mostly micritized ooids), ooids with quartz nuclei, foraminifera | Ooids, peloids,, bivalves, aggregate coated grains |
| **Texture (Dunham, 1962)** | Mudstone carbonates | Packstone | Wackestone-packstone | Grainstone | Grainstone |
| **Structures** | Micro-dissolution passages, massive. | Massive, bivalves oriented horizontally | Massive | Apparently massive, weathered planar X-bedding (not clear) | Planar to trough X bedding, reactivations surfaces |
| **Fossil content** | Skeletal fragments (undef.), Bivalves, foraminifera (1-2%) | Bivalves, skeletal grains (undef.), foraminifera | Peloids, foraminifera | Coated grains foraminifera | |
| **Porosity type / percent. (visual)** | Leaching, channel (non-fabric selective) (< 5%) | Moldic, intraparticle (20-25%) | Dissolution, Intraparticle, interparticle, channel (oriented with intraclasts) (<10%) | Intraparticle (< 10%) | Moldic, intergranular dissolution, intragranular (35-40%) |
| **Permeability (mean)** | ------ | ------ | ------ | ------ | 274.373 mD |

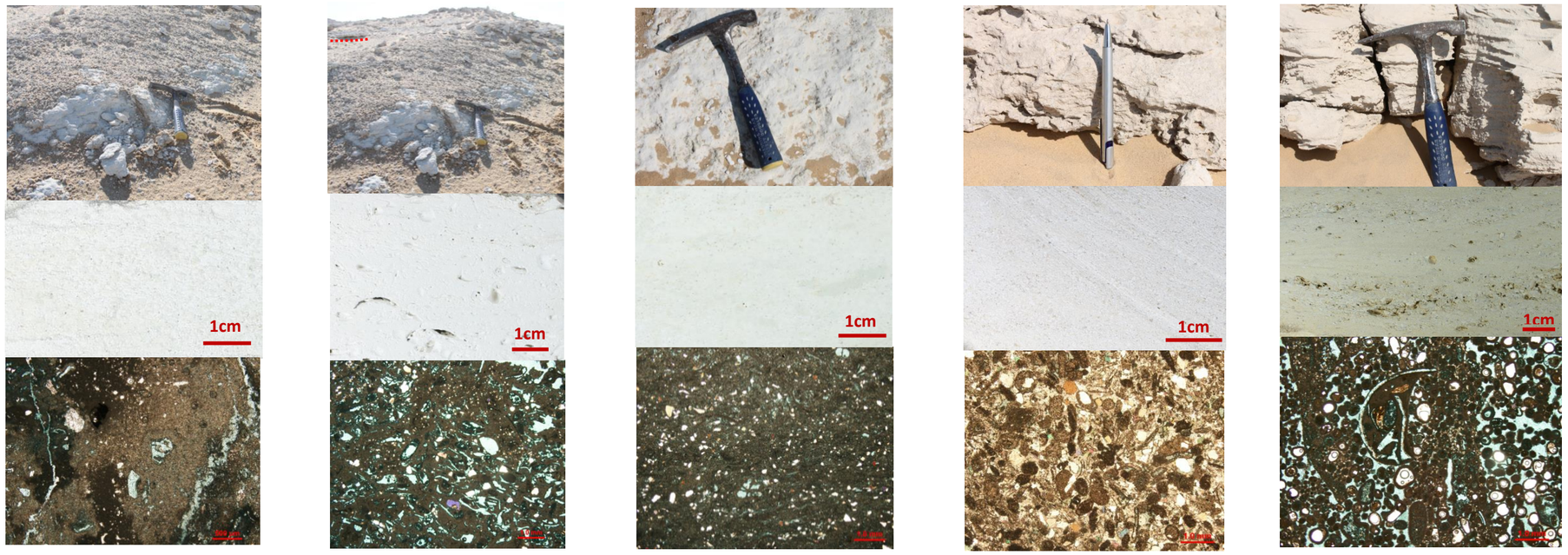

| Lithofacies No. | D10-6 | D10-7A | D10-7B | D10-8 | D10-9 |
|---|---|---|---|---|---|
| **Lithology** | Carbonate | Carbonate | Carbonate | Carbonate | Sandstone |
| **Color** | Shiny white | white | White | Pale white | Pale brown |
| **Composition** | 3 cyclic units of mudstone-wackestone with subangular to subrounded, well sorted Quartz grains (40%) | Skeletal fragments (>5%), quartz grains (>5%), in micritized matrix | Peloids, quartz grains | Ooids oncoids, peloids, aggregate coated grains, gastropods | Fine grained, very well sorted, sub-rounded to rounded quartz grains. |
| **Texture (Dunham, 1962)** | Wackestone | Mudstone | Wackestone | Grainstone | ------ |
| **Structures** | Horizontal bedding, each unit scours into lower beds | Massive, apparent evaporate pseudomorph (evaporate skin) | Massive, microchannel in thin section | Planar cross-bedded, hummocky cross stratified | Bioturbated (borrowing) at upper part, horizontal bedded to planar cross bedded |
| **Fossil content** | Peloids, skeletal grains (less than 3%) | Echinoid spine, skeletal fragments (Undef.) | ------ | Ooids, oncoids, peloids, coated aggregate grains, gastropods. | traces of worm activity |
| **Porosity type / percent (visual)** | Dissolution, intergranular (40%) | ------ | Channel (10%) | Interparticle, intraparticle, moldic (30-40%) | Intergranular (<5%) |
| **Permeability (mean)** | ------ | ------ | ------ | ------ | ------ |

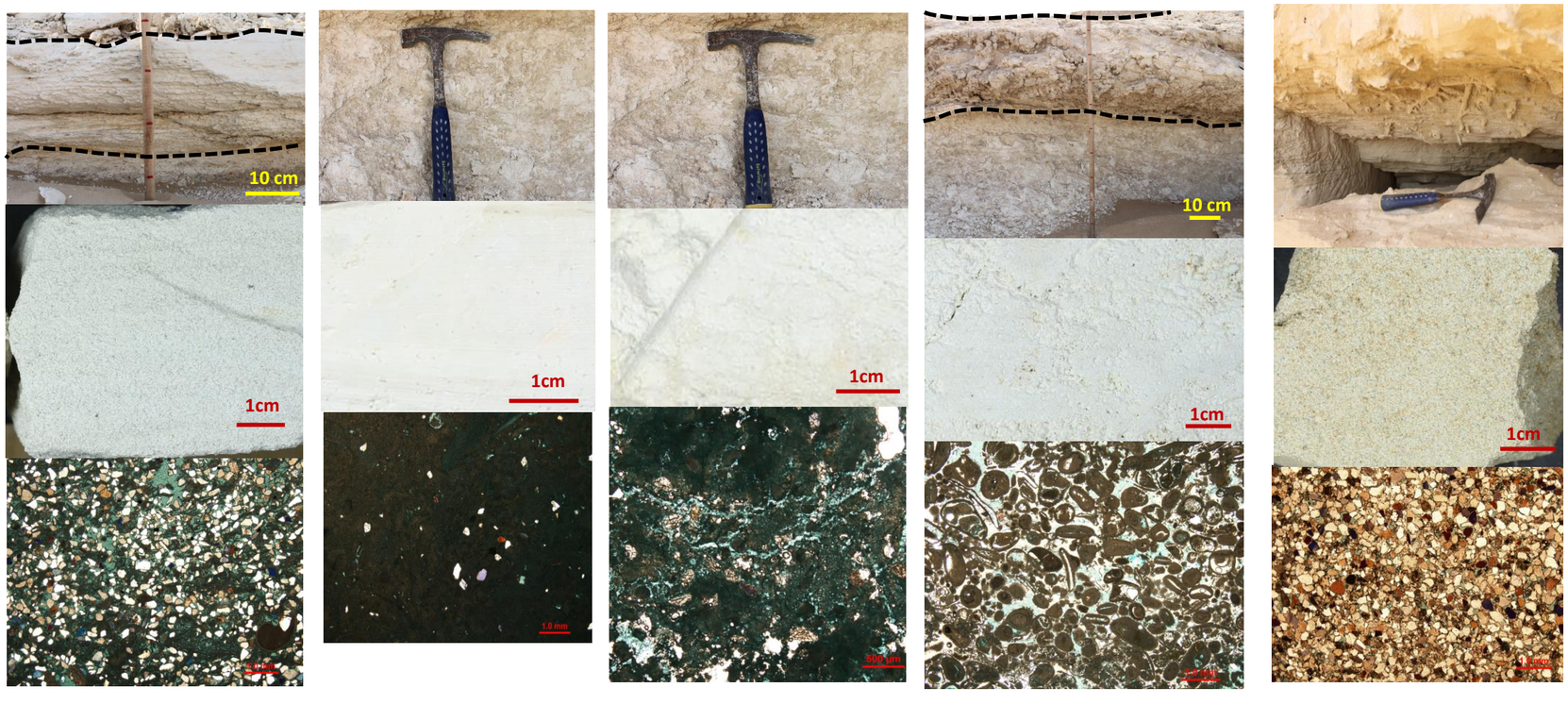

| Lithofacies No. | D10-10 | D10-11 | D10-12A | D10-12B | D10-12C |
|---|---|---|---|---|---|
| **Lithology** | Mudstone | Calcareous sandstone | Carbonate | Carbonate | Carbonate |
| **Color** | Dark green, pale grey | | Pale white | Pale white | Pale white, brownish white |
| **Composition** | Lime mud, quartz and sand grains | Fine grained, very well sorted, sub-rounded to rounded quartz grain, micrite matrix | Quartz grains (subangular to subrounded, well sorted), leached bivalves, skeletal fragments (undef.) | Quartz grains (moderate density) of subangular to subrounded, well sorted, leached bivalves, skeletal fragments (undef.) | Peloids, ooids, gastropods, bivalves, skeletal fragments (undefined), forams, quartz grains (least density), various size of mud intraclasts |
| **Texture (Dunham, 1962)** | ------ | ------ | Packstone | Packstone | Packstone |
| **Structures** | Fissile, desiccated, thinly laminated | Burrowing networks at top, bio – activity (warm trace) | Massive | Massive | Massive, breccia (mud intraclasts) |
| **Fossil content** | ------ | ------ | Bivalves, skeletal fragments (undef.) | Bivalves, skeletal fragments (undef.) pellets, coral fragments | Peloids, ooids, brachiopods, gastropods, bivalves, skeletal fragments (undef.), forams |
| **Porosity type / percent. (visual)** | ------ | Intergranular, dissolution of matrix (5%) | Leaching (10%) | Leaching (20-30%) | Leaching, Moldic, intraparticle (30-40%) |
| **Permeability (mean)** | ------ | ------ | 100.673 mD | 100.673 mD | 100.673 mD |

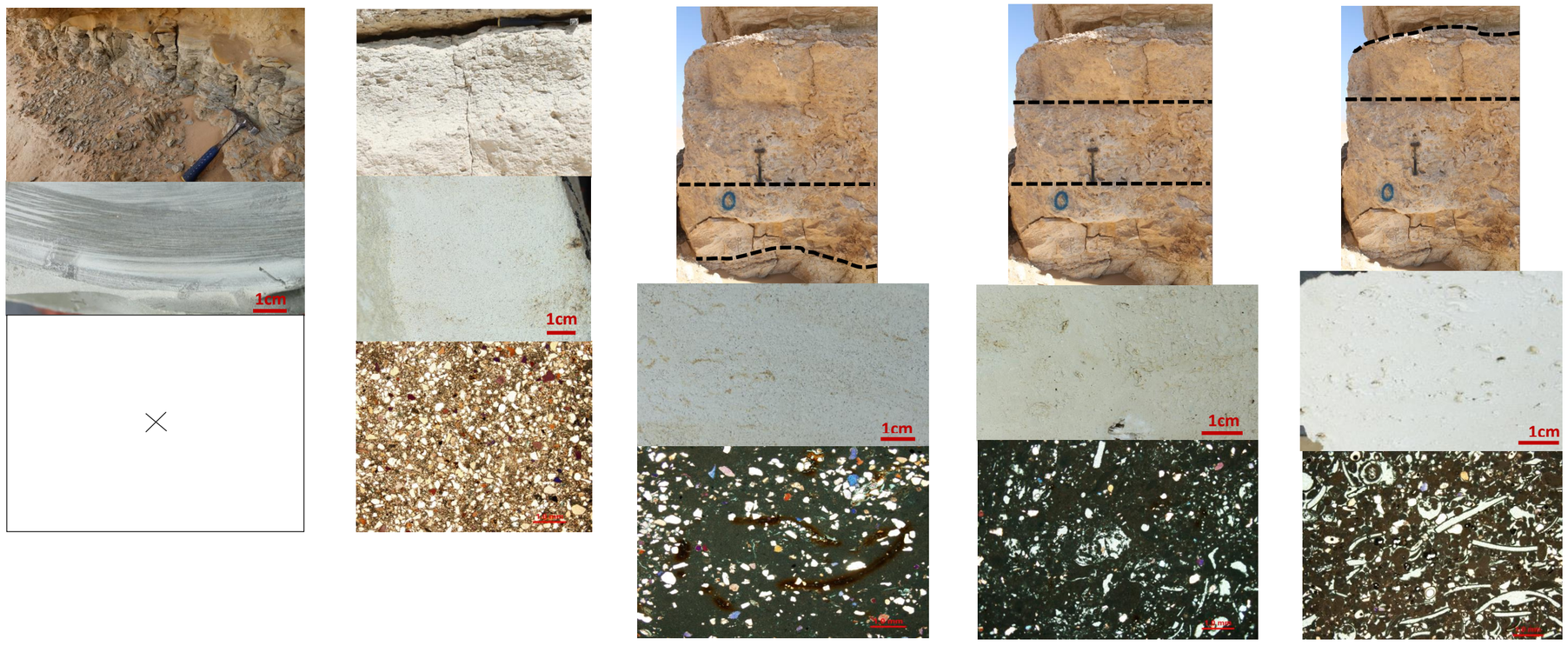

| Lithofacies No. | D10-13 | D10-14A | D10-14B | D10-14C | D10-14D | D10-14E |
|---|---|---|---|---|---|---|
| **Lithology** | Carbonate (Lime mud) | Carbonate | Carbonate | Carbonate | Carbonate | Carbonate |
| **Color** | Pale green | Pale white | Brownish white | Clear white | Brownish white | Brownish white |
| **Composition** | About 10% of subangular to subrounded quartz grains dispersed in a matrix of lime mud, diagenetic evaporate threads along the polygonal cracks | 10 % subangular to subrounded quartz grains, micritized matrix, trace of dissolved broken skeletal fragments | Peloids, bivalves, small and elongated mud intraclasts, foraminifera (>3%) | Micritized matrix with dispersed broken echinoid spines/shell fragments (5%) and subangular to subrounded quartz grains (15%) | Coated grains, bivalves, minor peloids, undefined skeletal fragments, foraminifera, Quartz grains (>3%) | Peloids, bivalves (increase upward in D10-15F), mud intraclasts, minor quartz grains and foraminifera (<1%) |
| **Texture** | Mudstone | Mudstone | Grainstone | Mudstone | Grainstone | Grainstone |
| **Structures** | Mud cracks, desiccation, fissile | Massive, the upper mudstone units show desiccation | Planar cross-bedded (different angles) to herringbone | Massive, to desiccated in some sections, tepee structure (inverted V-shape) | Massive, to planar bedded (clear in weathered surfaces), tepee structure (inverted V-shape) | Massive, coquina (rich in bivalves) |
| **Fossil content** | ------ | Remnant skeletal grains | Bivalves, peloids, ooids | Skeletal fragments (undef.) | Bivalves, undefined broken shells | Bivalves, undefined broken shells |
| **Porosity type / percent. (visual)** | Insignificant channel (around quartz halos) (<5%) | Dissolution and leaching (insignificant) (<10%) | Intergranular, moldic (20-30%) | Dissolution of echinoid/shell fragments (insignificant) (<5%) | Moldic, intergranular (25-30%) | Moldic, leaching, intergranular (15-20%) |
| **Permeability (mean)** | ------ | ------ | ------ | ------ | ------ | ------ |

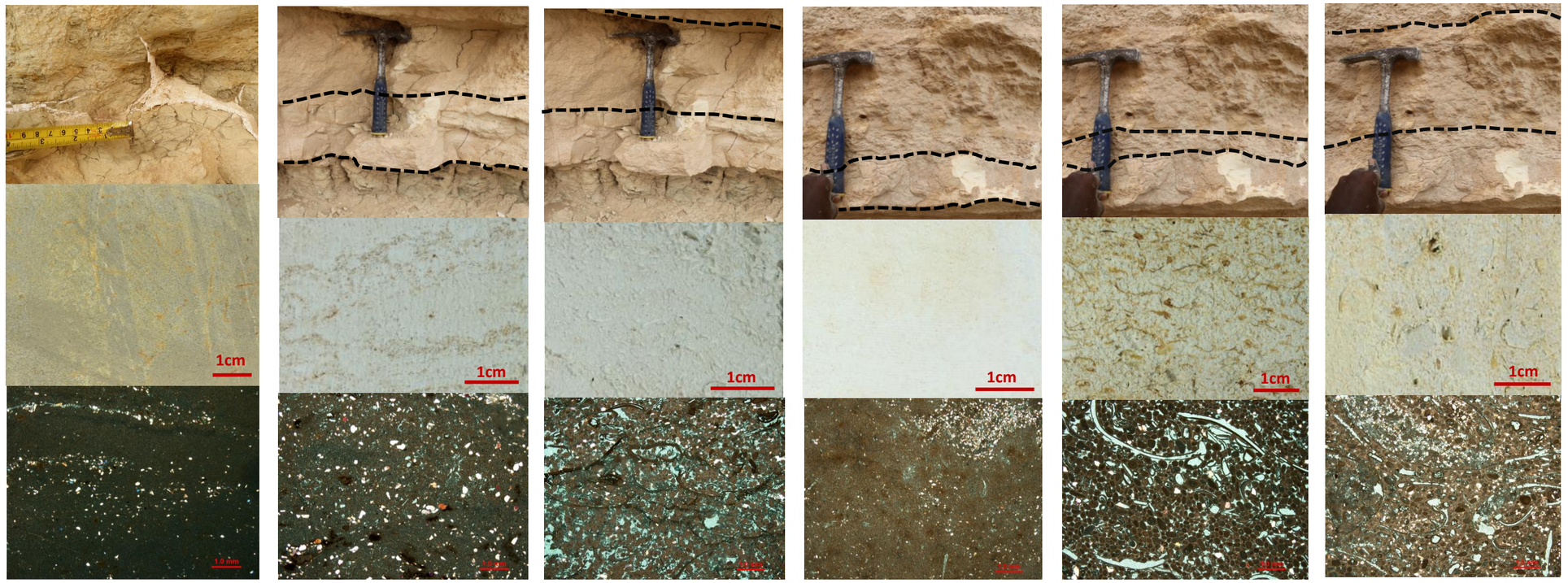

| **Lithofacies No.** | **D10-14F** | **D10-15** | **D10-16** | **D10-17** | **D10-18** | **D10-19** |
|---|---|---|---|---|---|---|
| **Lithology** | Carbonate | Carbonate | Carbonate | Carbonate | Carbonate | Carbonate |
| **Color** | Brownish white | Clear white | White to greenish white | Pale green | White | Brownish white |
| **Composition** | Peloids, bivalves, mud intraclasts, minor quartz grains, minor foraminifera (<1%) | Ooids, aggregate grains, elongated mud intraclasts, minor dissolved bivalves in partially micritized matrix | Bivalves, undefined skeletal grains, quartz grains in highly micritized matrix | Undefined shell fragments, bivalves quartz grains, minor gastropods and forams, | Undefined shell fragments, quartz grains, bivalves, peloids | Undefined shell fragments, Foraminifera, bivalves, gastropods, echinoid spines. |
| **Texture (Dunham, 1962)** | Grainstone | Grainstone | Wackestone | Wackestone-Packstone | Wackestone | Grainstone |
| **Structures** | Massive, rich in bivalves | Massive, flaser bedding of mud intraclasts at top | Massive, bioturbated at top | Fissile, desiccated, desiccation cracks | Massive | Stratified domal stromatolites, Enterolithic evaporites (bottom) |
| **Fossil content** | Bivalves, undefined broken shells | Minor bivalves, broken shell fragments | Bivalves, undefined shell fragments | Shell fragments, bivalves, minor forams, and gastropods | Intensive in lower part: Undefined shell fragments, bivalves | Undefined shell fragments, Foraminifera, bivalves, gastropods, echinoid spines. |
| **Porosity type / percent. (visual)** | Moldic, leaching, intergranular (15-25%) | Moldic, intergranular, dissolution (40%) | Dissolution, Channel (15-25%) | Moldic (5%) | Moldic, dissolution (20-25%) | Fenestral, interparticle, moldic (25-25%) |
| **Permeability (mean)** | ------ | ------ | 19.687 mD | ------ | ------ | 213.079 mD |

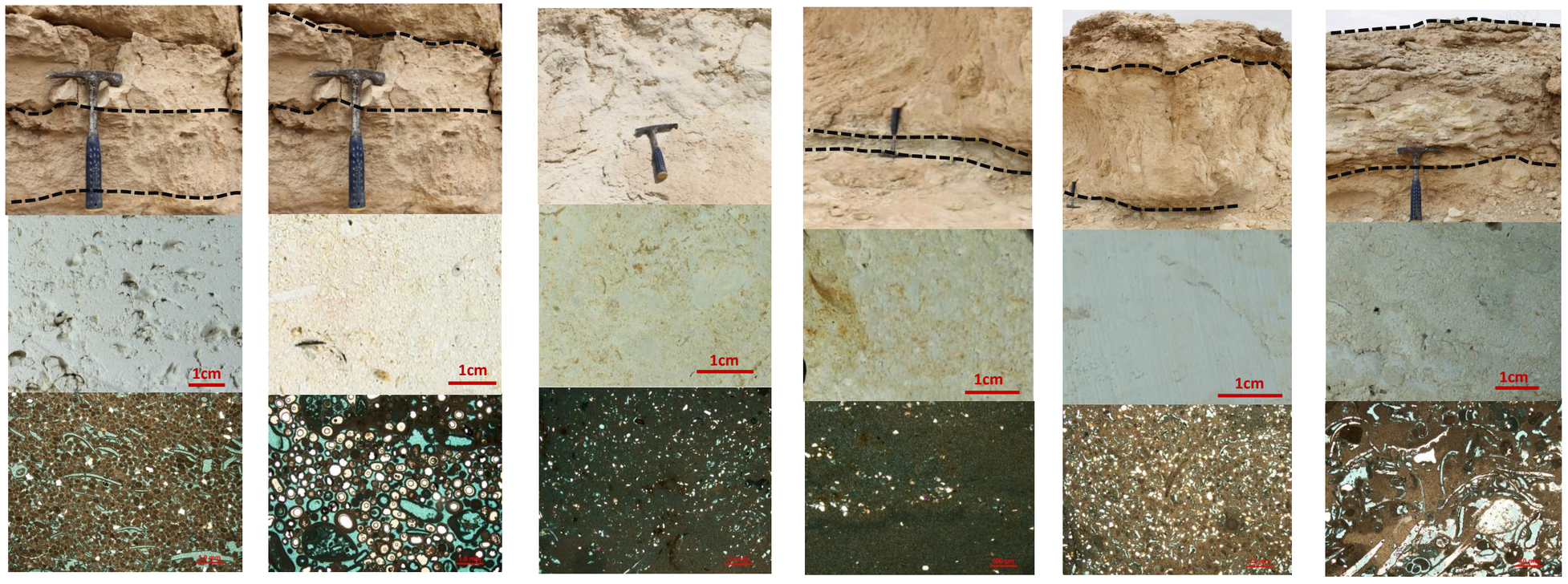

Enclosure 4-2: Modified “Geoeye” satellite map shows the study area, the rectangle represents the talus-dominated area, the numbers show locations of the five measured sections of the main outcrop body. See next four pages for the description of measured sections

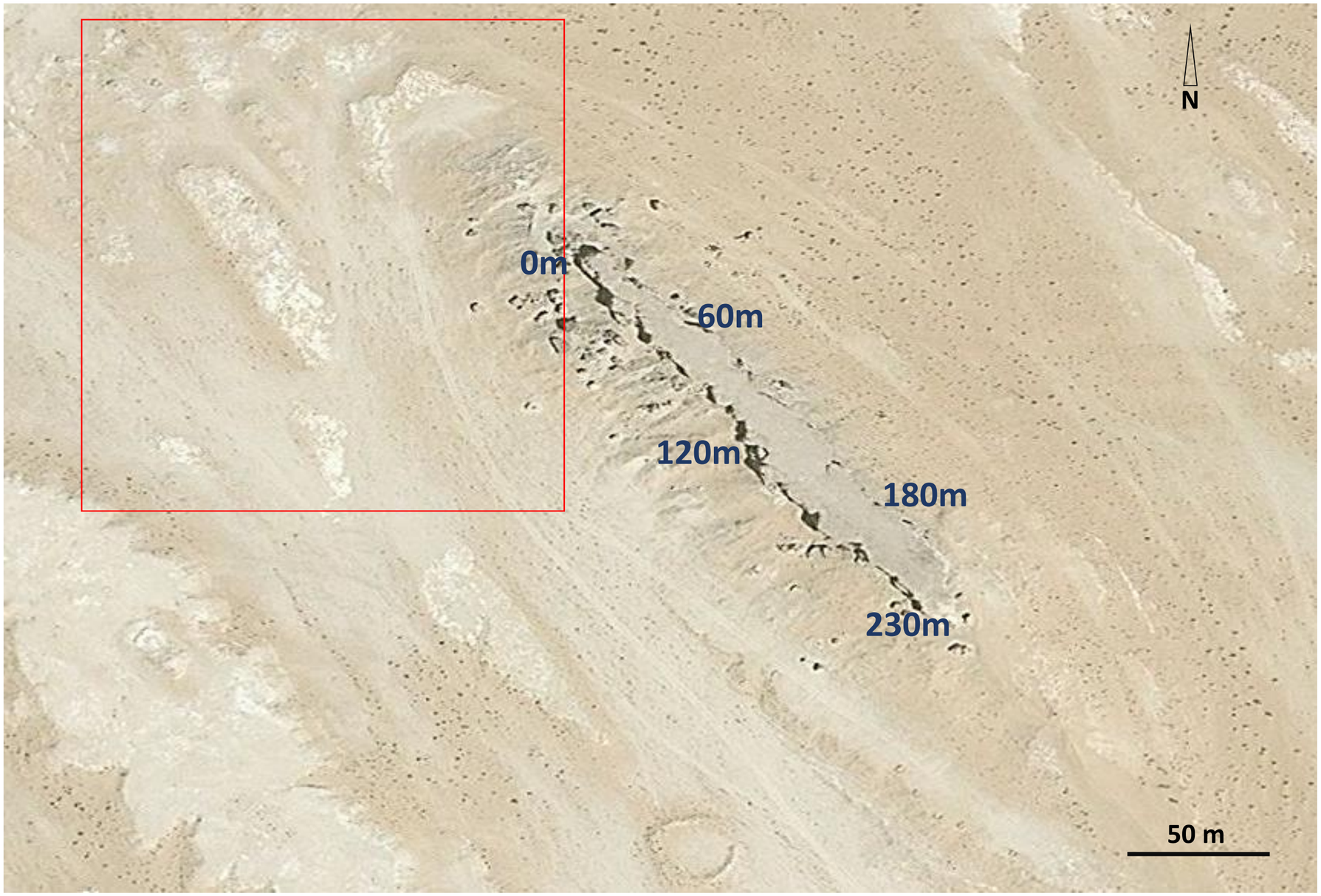

**Composite Section**

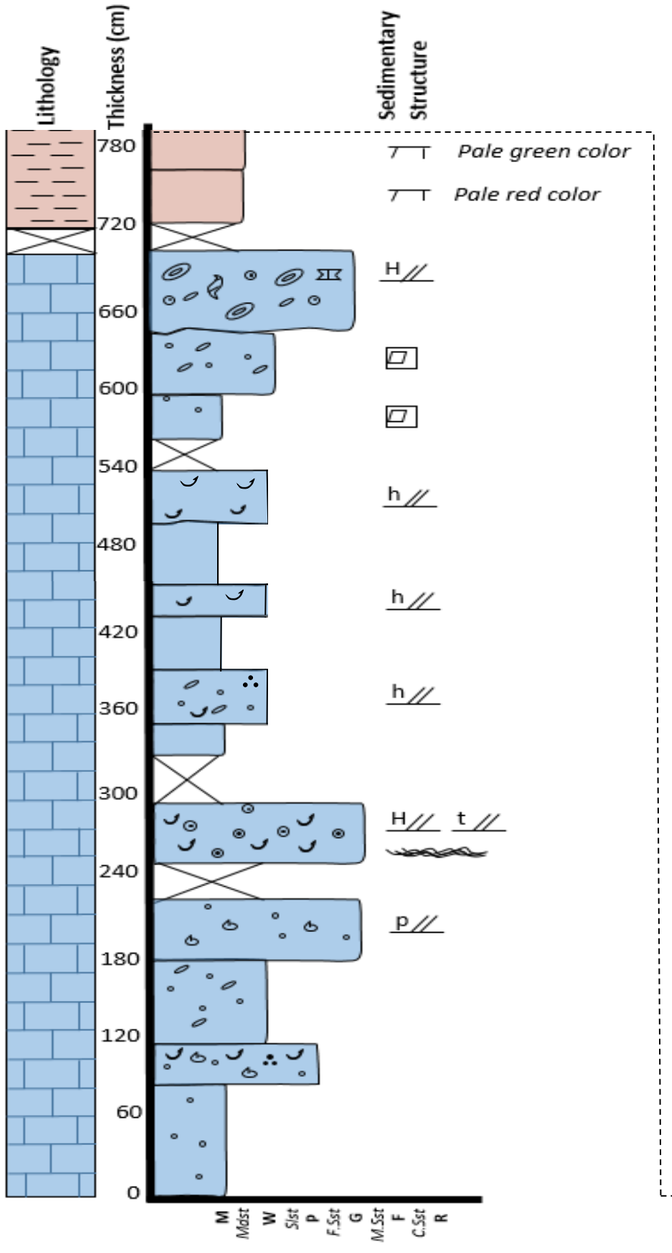


**Talus Section**

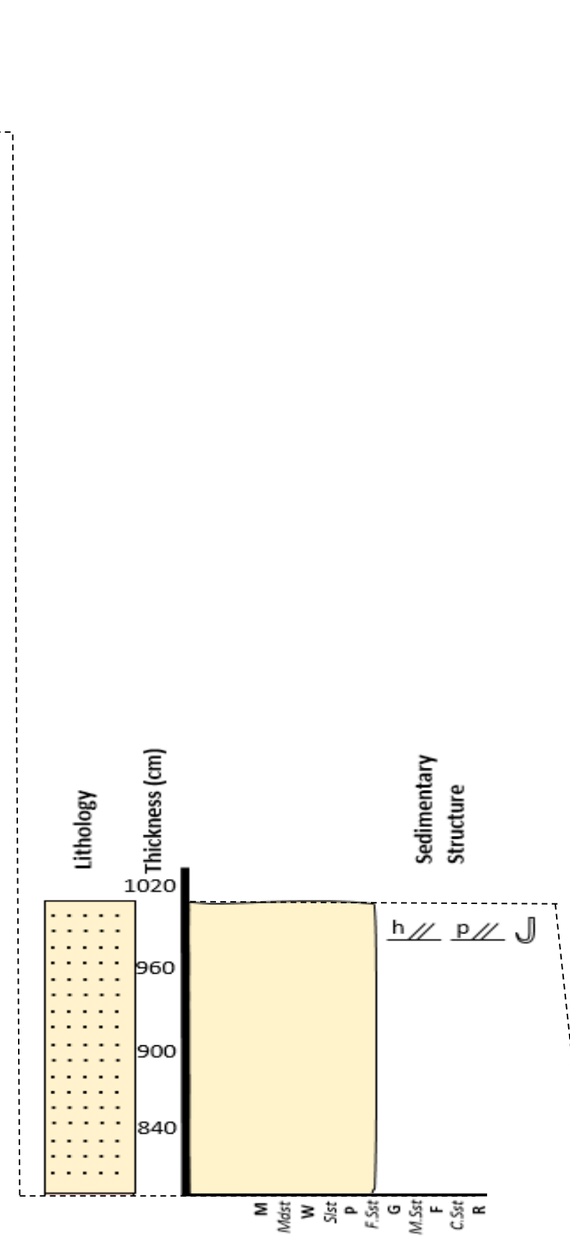


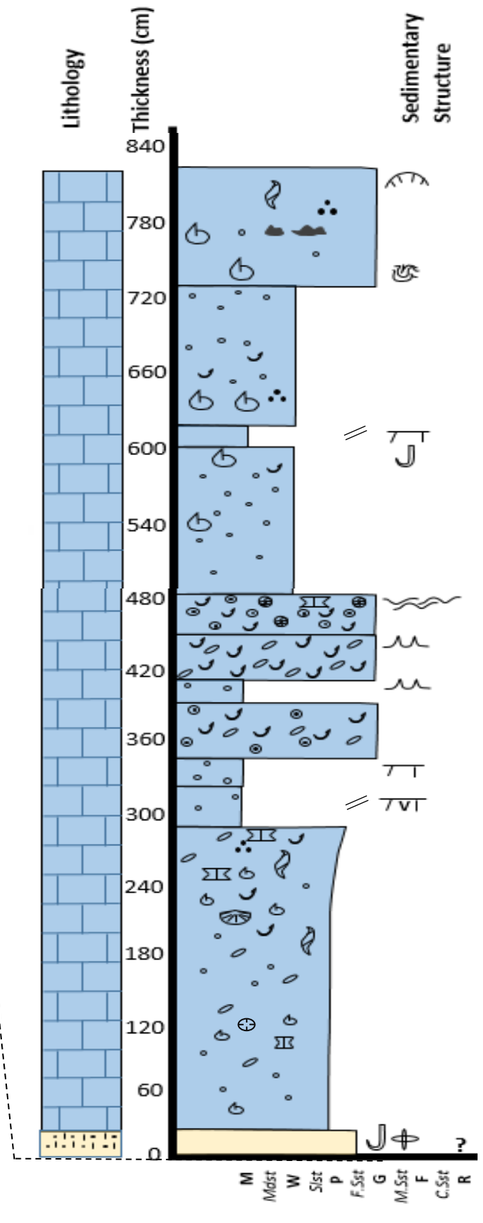


**0 m**

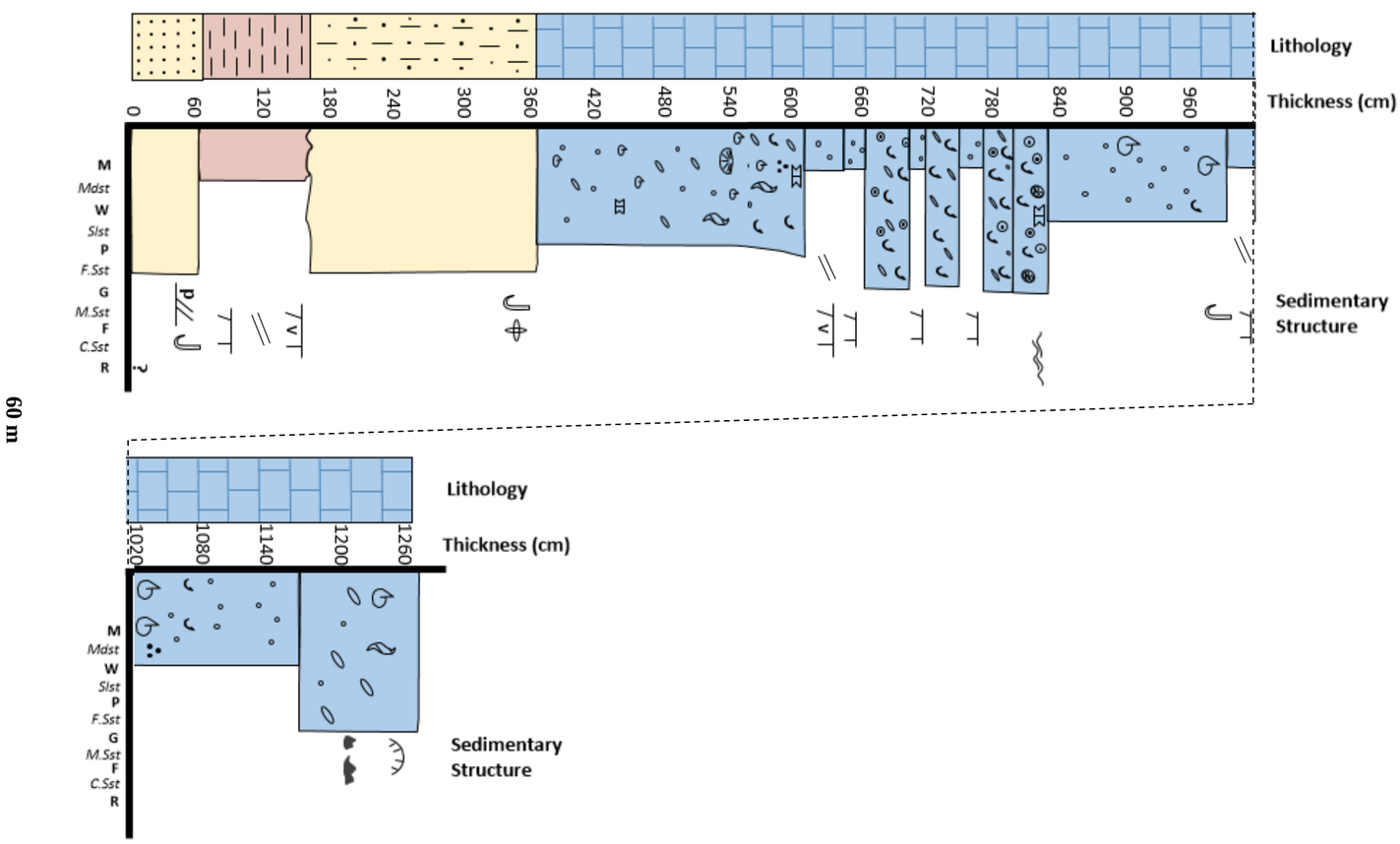
60 m
Lithology
Thickness (cm)
0
60
120
180
240
300
360
420
480
540
600
660
720
780
840
900
960
M
Mdst
W
Slst
P
F.Sst
G
M.Sst
F
C.Sst
R
Sedimentary
Structure
Lithology
Thickness (cm)
1020
1080
1140
1200
1260
Sedimentary
Structure

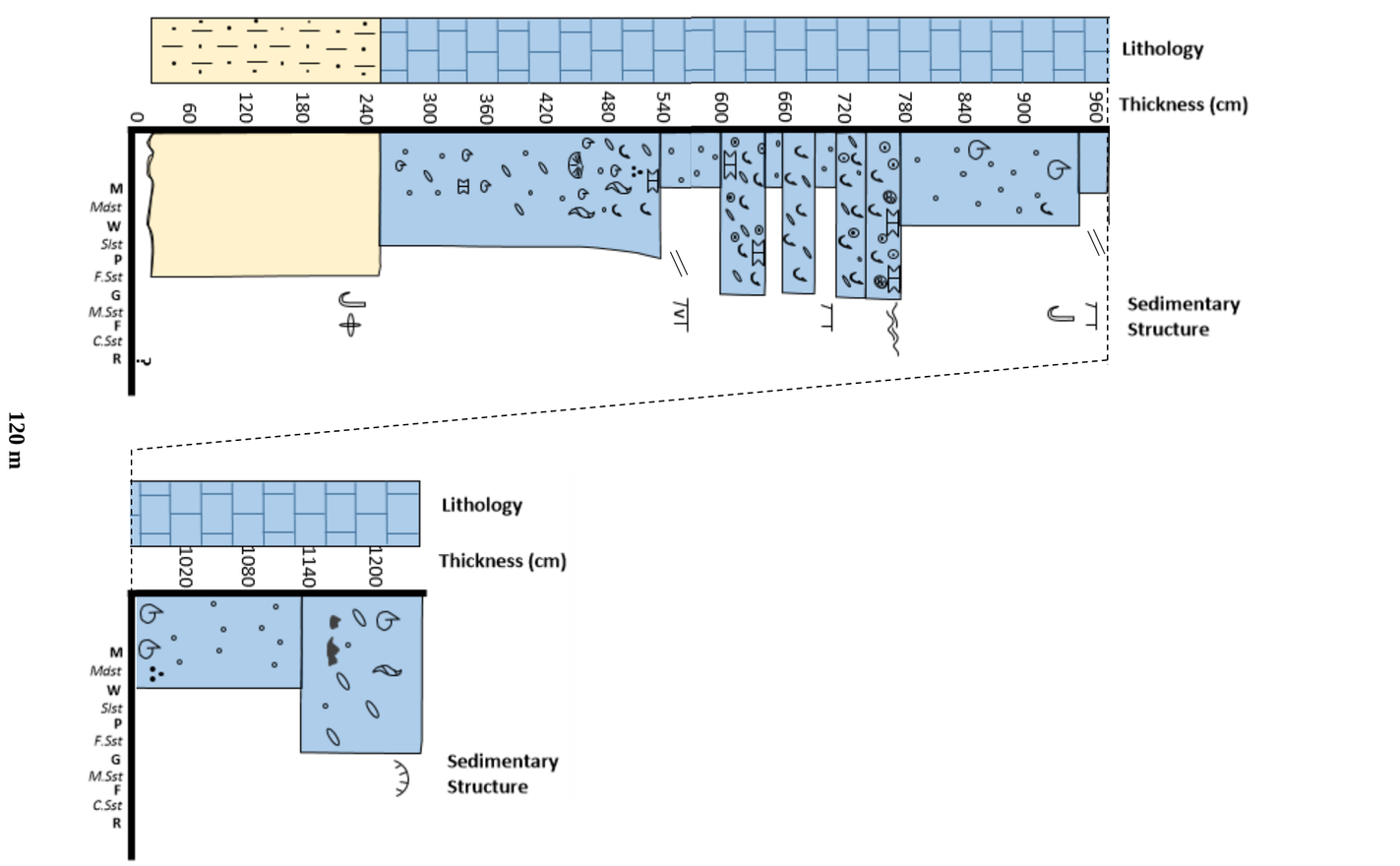
120 m
Lithology
Thickness (cm)
0
60
120
180
240
300
360
420
480
540
600
660
720
780
840
900
960
M
Mdst
W
Slst
P
F.Sst
G
M.Sst
F
C.Sst
R
Sedimentary
Structure
Lithology
Thickness (cm)
1020
1080
1140
1200
Sedimentary
Structure

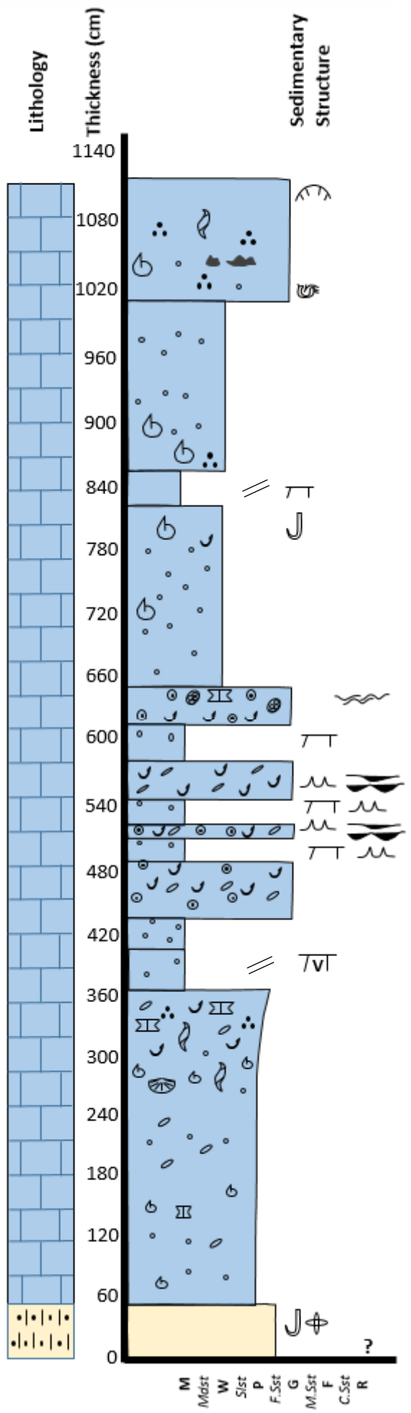
Lithology
Thickness (cm)
Sedimentary Structure
1140
1080
1020
960
900
840
780
720
660
600
540
480
420
360
300
240
180
120
60
0
?
M
Mdst
W
Slst
P
F.Sst
G
M.Sst
F
C.Sst
R

**180 m**

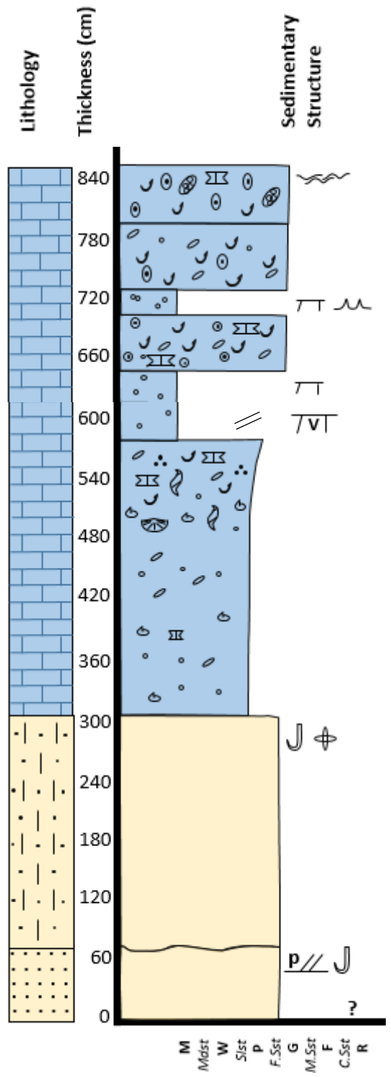
Lithology
Thickness (cm)
Sedimentary Structure
840
780
720
660
600
540
480
420
360
300
240
180
120
60
0
p
?
M
Mdst
W
Slst
P
F.Sst
G
M.Sst
F
C.Sst
R

**230 m**

## Basic Lithology

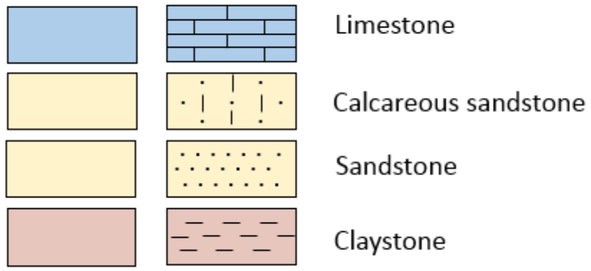


**M:** Mudstone-carbonate

*Mdst:* Mudstone siliciclastic

**W:** Wackestone

*Slst:* Siltstone

**P:** Packstone

*F.Sst:* Fine-grained Sandstone

**G:** Grainstone

*M.Sst*: Medium-grained Sandstone

**F:** Floatstone

*C.Sst*: Coarse-grained Sandstone

**R:** Rudstone

-

## Composition/Texture/Structure

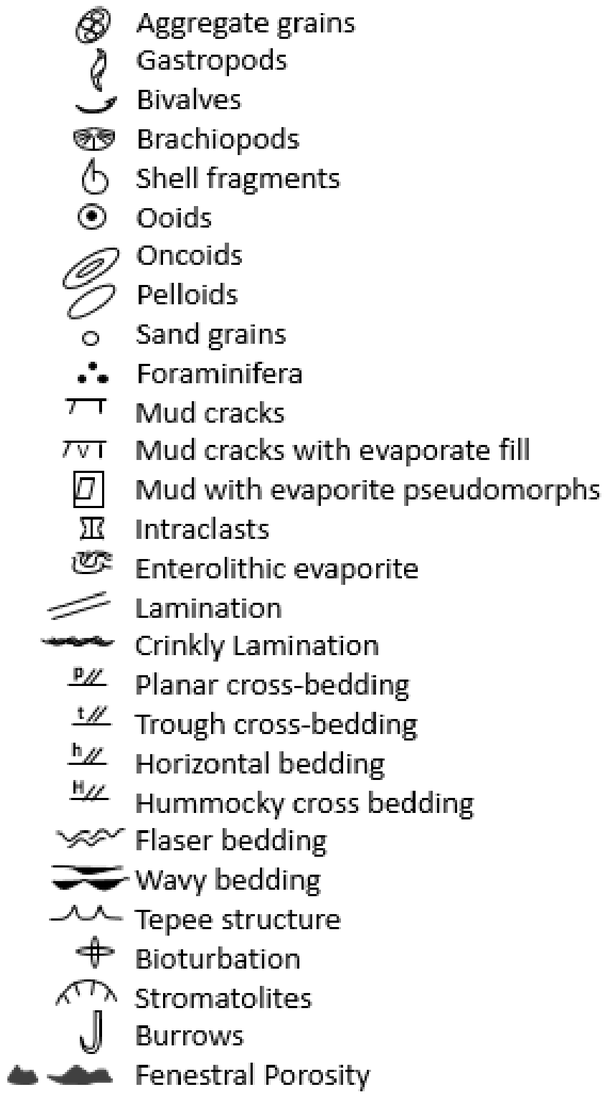

# CHAPTER 5

# POROSITY AND PERMEABILITY CHARACTERIZATION

## 5.1 Introduction

The statistical distribution and correlations of petrophysical parameters such as porosity and permeability give significant insights about reservoir rocks. Spatial distribution of porosity and permeability generally depend on lithology. Each zone and/or layer in a reservoir may provide a distinct set of porosity and permeability values with a characteristic statistical distribution (Saner and Sahin, 1999). Consequently, it may be possible to refine the reservoir zonation and to identify different lithologies using the statistical distributions study (Busch et al., 1987; Jensen et al., 1987).

This chapter presents the statistical analyses of the porosity and permeability, and their relationships. The univariate statistics includes mean, median, standard deviation, coefficient of variation, skewness, and other parameters for each variable. Histograms were constructed to reveal the types of distribution, and investigate the homogeneity of the dataset.

## 5.2 Univariate Statistics

Out of the overall lithofacies assemblage of the Dam Formation in the studied outcrop, 4 lithofacies were considered for porosity and permeability characterization. The results of univariate statistics, and porosity-permeability relationships of these lithofacies are elaborated in the following discussion, besides, the vertical and horizontal permeability correlation.

The datasets consist of 254 porosity and permeability measurements made on core plugs (mostly 1.5" diameter), obtained from samples collected from the Dam Formation outcrop. Only horizontal plugs were used later for petrophysical modeling. The distribution of these samples includes 51 plugs form skeletal oolitic grainstone, 112 plugs from sandy fossiliferous packstone, 50 plugs from burrowed wackestone, and 41 plugs from stromatolite grainstone. The porosity measurements were conducted using TPI-219 Helium porosimeter device, while permeability measurements were conducted using TKA-209 Gas Permeameter device.

The selection criteria of these lithofacies depended on petrographic investigation of different lithofacies, and then selecting of the best reservoir-prone units according to the petrography. In addition to the intention of characterizing the porosity and permeability for different lithofacies which are documented to be potential units in literature. These lithofacies were selected for reservoir properties examination upon the petrographic investigation, following the criteria of Borgomano et al., 2013. According to Dunham classification (Dunham, 1962), the selected lithofacies include, from bottom to top, the

skeletal oolitic grainstone, the sandy fossiliferous packstone, the burrowed wackestone, and the domal stromatolite grainstone.

The results of the comprehensive univariate analyses and graphical representation of the data are summarized and given in the following sections.

### 5.2.1 Univariate statistics of porosity

The univariate analyses of porosity data of the four lithofacies showed homogeneous relationships between the mean and median (Table 5-1), although, no homogeneity were detected in their histograms, except for the skeletal oolitic grainstone (Figure 5-1). These results correspond with the negative skewness of data sets, since the mean is less than the median except for skeletal oolitic grainstone, where the skewness is positively close to zero (observation is symmetrical around the mean) (Figure 5-1A), comparing to the asymmetrical distribution in other lithofacies (Figure 5-1B, C, D). In addition, the mode of the histograms revealed unimodal distribution for each lithofacies (Figure 5-1). Detailed description of univariate spatial distribution of porosity cannot be attained without considering the spreading around the center of dataset. In this context, the standard deviation (SD) of both of the sandy fossiliferous packstone and stromatolite grainstone is higher than that of skeletal oolitic grainstone and burrowed wackestone, respectively. Due to low values of the first two lithofacies, their coefficients of variations (CV) are relatively higher (Table 5-1). However, in all lithofacies, the coefficient of variation is less than 1, indicating that linear geostatistics can be used for the final geostatistical modeling. Besides the skewness, the shape of histograms reflected platykurtic shape in all lithofacies, which indicated by kurtosis less than 3 (flat top

distribution), the only exception is referred to the sandy fossiliferous packstone where higher Kurtosis agrees with the leptokurtic shape, caused by number of high porosity values.

Table 5-1: Summary of the univariate statistical parameters of porosity data

| | Measure of centre | | Measure of location | | Measure of spread | | Measure of shape | | |
|---|---|---|---|---|---|---|---|---|---|
| **Lithofacies** | Mean | Median | Min | Max | SD | Variance | CV | Skewness | Kurtosis |
| **Skeletal oolitic grainstone** | 38.517 | 38.081 | 29.221 | 48.372 | 4.068 | 16.547 | 0.106 | 0.162 | 0.415 |
| **Sandy fossiliferous packstone** | 41.778 | 47.083 | 3.913 | 49.988 | 7.134 | 50.888 | 0.171 | -3.417 | 15.193 |
| **Borrowed wackstone** | 45.916 | 46.899 | 36.699 | 49.984 | 3.345 | 11.191 | 0.073 | -1.022 | 0.303 |
| **Stromatolite grainstone** | 32.702 | 34.572 | 13.597 | 42.708 | 7.501 | 56.265 | 0.229 | -0.850 | 0.065 |

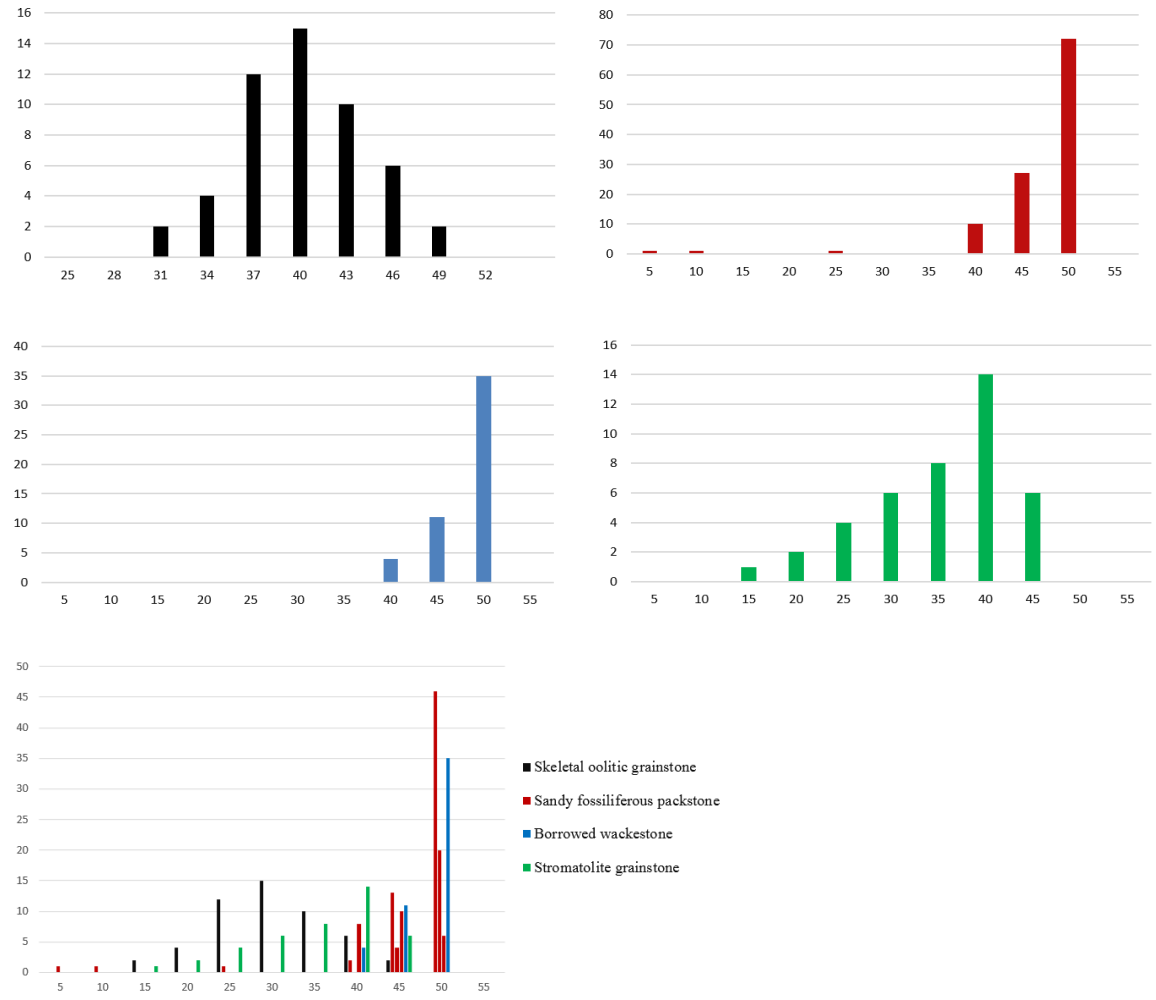


Figure 5-1: Histograms of porosity distribution of the selected lithofacies

### 5.2.2 Univariate statistics of permeability

In contrary to the porosity distribution, permeability data showed more heterogeneity. Permeability distribution showed heterogeneity for the raw permeability data. However, the logarithmic values enhanced the normality of distribution, and this is because the permeability usually appear to be log-normally distributed (Amaefule et al., 1993; Jensen et al., 1997).

The skeletal oolitic grainstone showed separations between the mean and median values which corresponds with the asymmetrical histogram shape (Table 5-2, Figure 5-2A). This is also a result of positive skewness (mean is greater than median). The horizontal permeability distribution showed positive skewness less than that of vertical permeability, this indicates that horizontal permeability data are more heterogeneous (symmetrical distribution around the mean). The wide difference between the maximum and minimum values interpret the higher standard deviation (SD) and consequently, the high variance. This observation corresponds with the relatively high coefficient of variation (CV), which is close to 1 (Table 5-2). It is clear that the non-normality of permeability data is mostly a result of vertical permeability (higher CV and higher skewness). The kurtosis analysis of horizontal permeability histogram showed platykurtic shape (flat top), however, kurtosis of vertical permeability showed leptokurtic (sharp peak).

Regarding the sandy fossiliferous packstone, the permeability measurements exhibit heterogeneous behavior in spite of the large collected data, the difference in sedimentary components of this unit is the cause of difference in permeability. As discussed in the

previous chapter, this lithofacies was divided into three subunits, with skeletal grain size increasing upwards (these subunits represent coarsening upward in grain size distribution). The univariate statistics showed a large separation between the mean and median (Table 5-2), which is reduced by considering logarithm normality of the datasets. Since the mean is greater than the median, the resulting skewness is positive, for all permeability values, indicating the more heterogeneous permeability in this flow direction. This is also confirmed by the leptokurtic shape of histogram (Table 5-2, Figure 5-2). In contrary, the logarithm of permeability of this lithofacies indicated a better distribution (platykurtic, less skewness), and the coefficient of variation for the data sets indicates that non-linear geostatistics can be used (CV>1).

The permeability values of the burrowed wackestone exhibited the least gap between the mean and median of datasets. Permeability patterns of the domal stromatolite grainstone showed a gap between the mean and median which corresponds with the positive skewness where the mean is always greater than the median (Table 5-2). High standard deviation is reasonable outcome of the wide range of dataset. This led to a higher coefficient of variation. Kurtosis of the domal stromatolite grainstone exhibited leptokurtic histogram shape of the logarithm of permeability (Figure 5-2D) while the raw data exhibited platykurtic for horizontal permeability. In contrary to the skeletal oolitic grainstone, this lithofacies showed less heterogeneity of permeability in the vertical direction compared to horizontal direction, in terms of mean to median relationship and standard deviation, this is only applicable for raw dataset (Table 5-2). The Histogram of the permeability distribution showed poor normal distribution (Figure 5-2) which can be attributed to the observable dissimilarity in its basic statistics (Table 5-2, Figure 5-2).

Table 5-2: Summary of the univariate statistical parameters of permeability data

| Lithofacies | Measure of centre | | Measure of location | | Measure of spread | | Measure of shape | | |
|---|---|---|---|---|---|---|---|---|---|
| | Mean | Median | Min | Max | SD | Variance | CV | Skewness | Kurtosis |
| **Skeletal oolitic grainstone** | 274.373 | 184.666 | 17.542 | 915.167 | 231.981 | 53815.142 | 0.845 | 1.214 | 0.923 |
| H | 328.877 | 300.055 | 49.280 | 914.435 | 243.755 | 59416.461 | 0.741 | 0.789 | -0.209 |
| V | 219.870 | 167.135 | 17.542 | 937.604 | 210.398 | 44267.338 | 0.957 | 1.952 | 4.587 |
| **LOG** | 2.270 | 2.266 | 1.244 | 2.972 | 0.415 | 0.172 | 0.183 | -0.388 | -0.347 |
| LOG.H | 2.381 | 2.477 | 1.693 | 2.961 | 0.373 | 0.139 | 0.156 | -0.259 | -1.114 |
| LOG.V | 2.159 | 2.223 | 1.244 | 2.972 | 0.433 | 0.188 | 0.201 | -0.346 | -0.206 |
| **Sandy fossiliferous packstone** | 100.673 | 11.112 | 2.491 | 1297.599 | 202.665 | 41073.117 | 2.013 | 3.315 | 13.607 |
| H | 109.691 | 14.920 | 2.491 | 1297.599 | 234.096 | 54800.923 | 2.134 | 3.473 | 13.892 |
| V | 90.715 | 9.846 | 3.000 | 613.127 | 162.990 | 26565.830 | 1.797 | 2.230 | 4.072 |
| **LOG** | 1.357 | 1.046 | 0.396 | 3.113 | 0.724 | 0.524 | 0.533 | 0.781 | -0.706 |
| LOG.H | 1.380 | 1.174 | 0.396 | 3.113 | 0.722 | 0.522 | 0.523 | 0.850 | -0.497 |
| LOG.V | 1.331 | 0.992 | 0.477 | 2.788 | 0.732 | 0.536 | 0.550 | 0.738 | -0.890 |
| **Borrowed wackstone** | 19.687 | 9.847 | 2.761 | 199.859 | 31.671 | 1003.050 | 1.609 | 4.304 | 21.501 |
| H | 27.983 | 11.988 | 2.761 | 199.859 | 42.929 | 1842.858 | 1.534 | 3.167 | 11.056 |
| V | 11.392 | 8.149 | 3.084 | 48.307 | 10.172 | 103.463 | 0.893 | 2.478 | 6.912 |
| **LOG** | 1.061 | 0.993 | 0.441 | 2.301 | 0.395 | 0.156 | 0.372 | 1.030 | 1.227 |
| LOG.H | 1.176 | 1.079 | 0.441 | 2.301 | 0.450 | 0.203 | 0.383 | 0.799 | 0.489 |
| LOG.V | 0.945 | 0.911 | 0.489 | 1.684 | 0.297 | 0.088 | 0.314 | 0.730 | 0.375 |
| **Stromatolite grainstone** | 213.079 | 109.883 | 0.103 | 1021.019 | 267.935 | 71788.921 | 1.257 | 1.810 | 2.705 |
| H | 363.268 | 273.940 | 11.246 | 1021.019 | 297.132 | 88287.689 | 0.818 | 1.189 | 0.334 |
| V | 54.986 | 32.245 | 0.103 | 376.427 | 83.168 | 6916.843 | 1.513 | 3.521 | 13.811 |
| **LOG** | 1.897 | 2.041 | -0.986 | 3.009 | 0.803 | 0.645 | 0.423 | -1.377 | 3.282 |
| LOG.H | 2.401 | 2.435 | 1.051 | 3.009 | 0.439 | 0.192 | 0.183 | -1.300 | 3.768 |
| LOG.V | 1.367 | 1.508 | -0.986 | 2.576 | 0.761 | 0.579 | 0.557 | -1.760 | 4.691 |

However, the normality of permeability patterns using the log values showed better normal distribution of the data sets. The log-permeability distribution revealed less skewness and less contrast between mean and median, indicating the effect of log-normalization on datasets (Table 5-2, Figure 5-3).

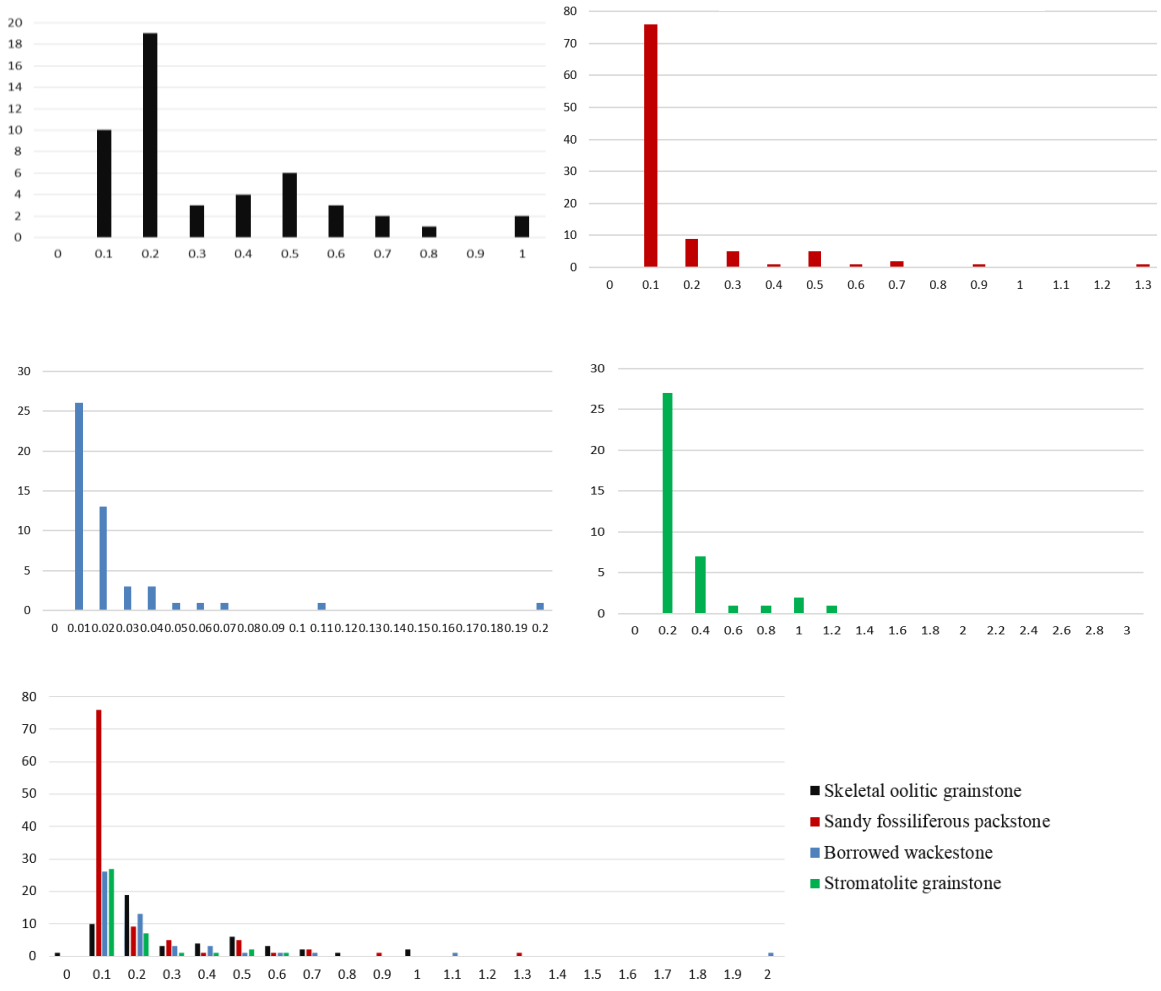


Figure 5-2: Histograms of raw permeability distribution of the selected lithofacies; permeability in Darcy

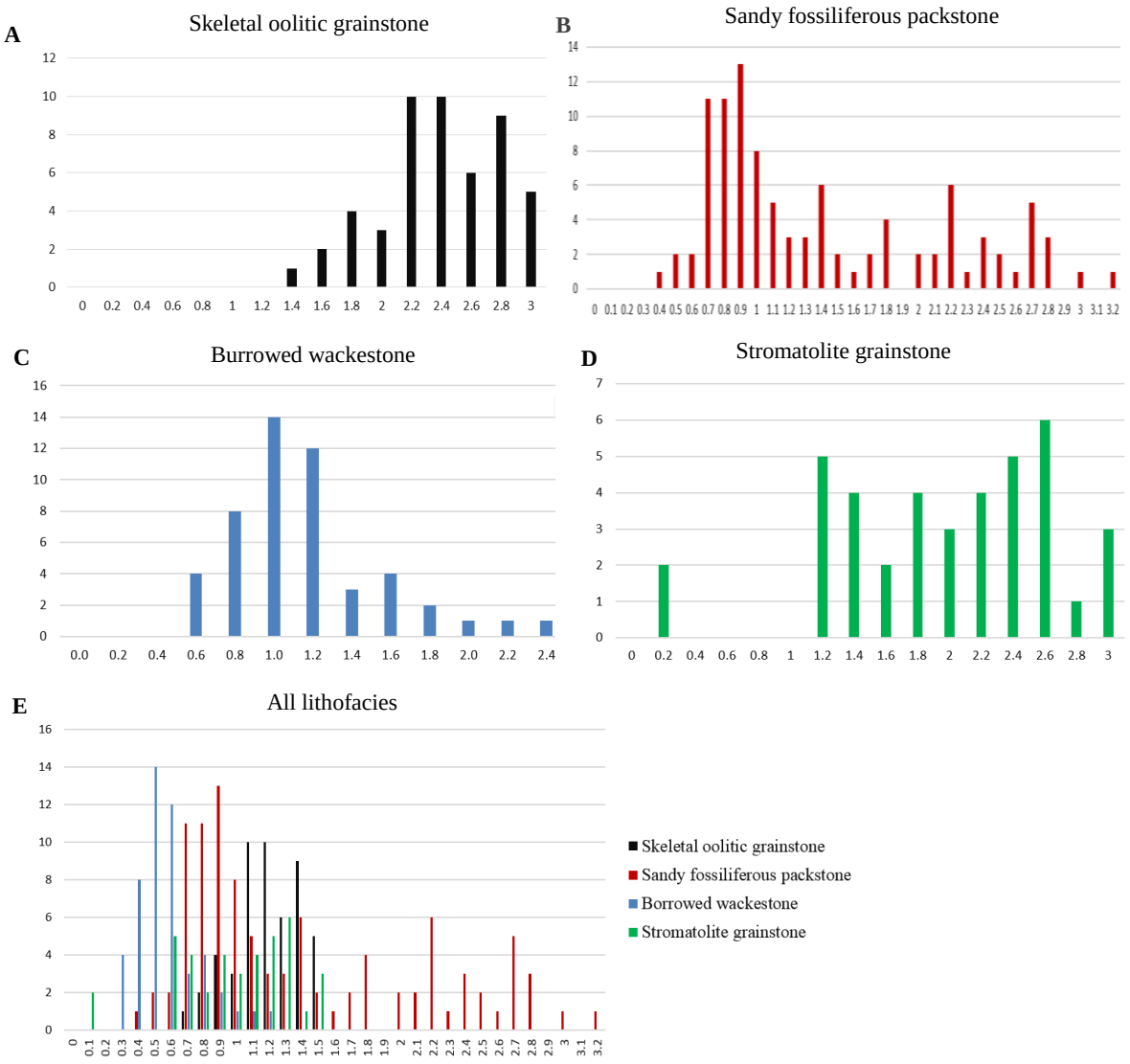


Figure 5-3: Histograms of log-permeability distribution of the selected lithofacies; permeability in millidarcy

## 5.3 Porosity-Permeability Relationship

Carbonate rocks show wide variability in petrophysical properties, such as porosity and permeability, in wide interval of scale. These heterogeneities raised as a result of complex sedimentary and diagenetic processes (Mazzullo and Chilingarian, 1992; Moore, 2001; Mylroie and Carew, 2003).

Porosity-permeability cross plots of the selected lithofacies of the Dam Formation showed weak correlation (Figure 5-4, 5-5), that demonstrates the importance of considering additional factors, other than porosity, for best modeling of the heterogeneous permeability. In this context, many equations considered the importance of size and distribution of pore space (Lucia, 1999).

The regression relationship between permeability and porosity reflects weak dependence relationship, indicated by low $R^2$ values (Figure 5-4). The complex relationship between porosity and permeability is common in carbonate rocks (Ling et al., 2014).

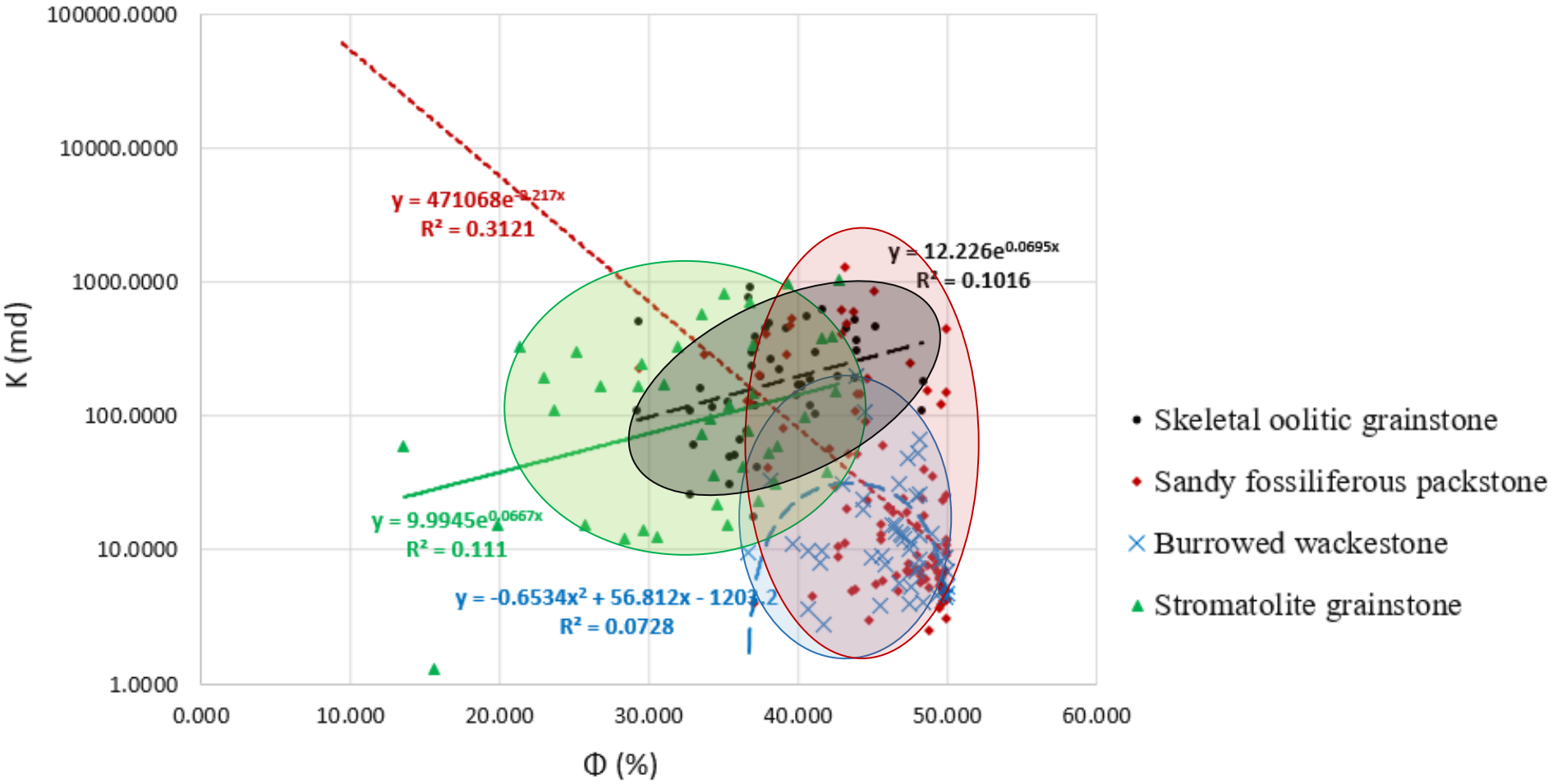


Figure 5-4: Cross-plot of permeability versus porosity for the selected lithofacies of Dam Formation in the studied outcrop

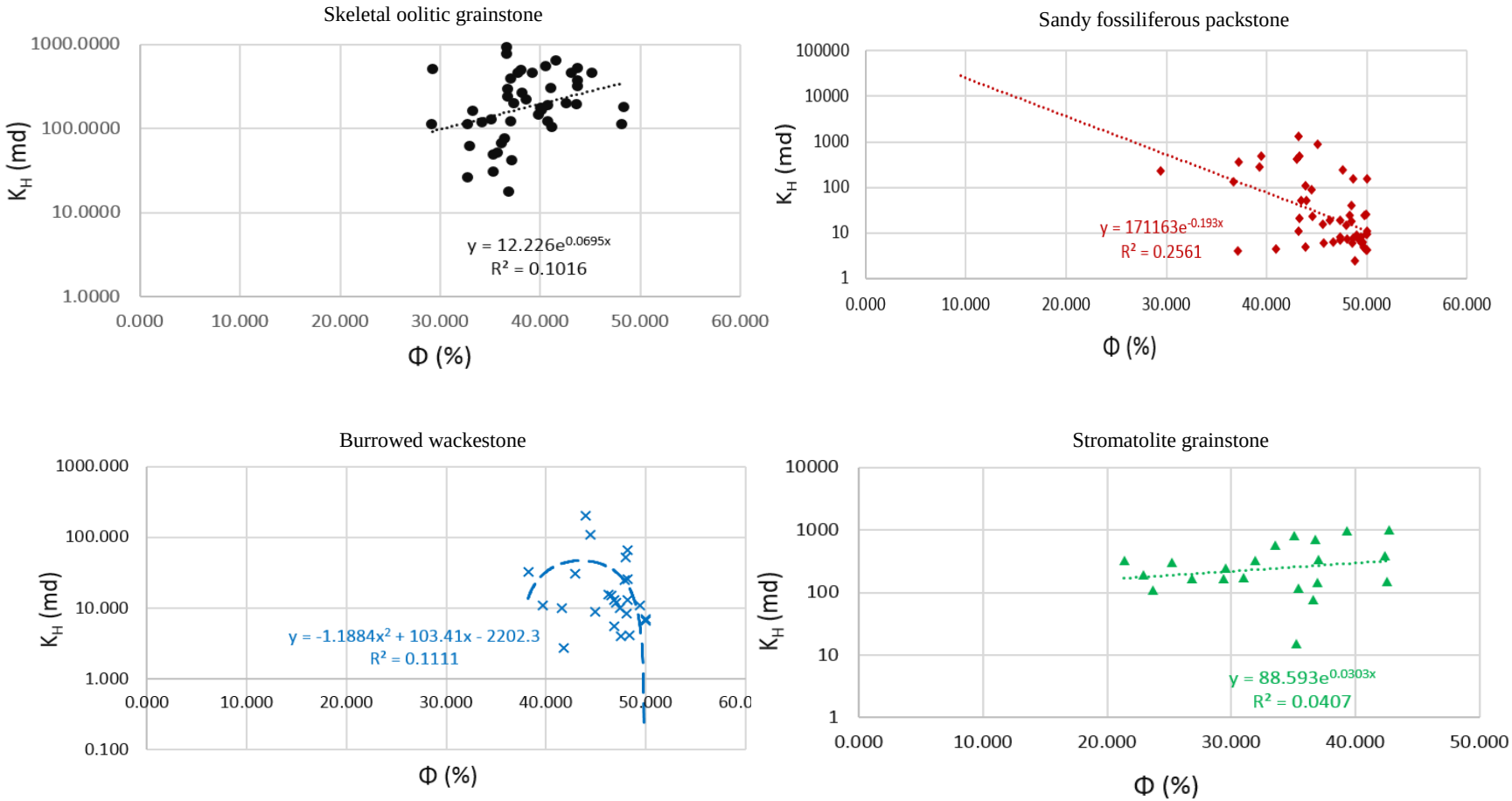


Figure 5-5: Cross-plot of horizontal permeability versus porosity for the selected lithofacies of Dam Formation in the studied outcrop

## 5.4 Permeability Isotropy

The degree of heterogeneity in rock permeability can be expressed by directional permeability measurements in the vertical and horizontal direction (Tiab and Donaldson, 2011). In the study area. The relationship between vertical and horizontal permeability showed good correlation, reflecting the degree of isotropy of flow zones in 2D direction of both of the domal stromatolite grainstone and skeletal oolitic grainstone, compared to the burrowed wackestone and sandy fossiliferous packstone, respectively (Figure 5-6). The weak correlation coefficient of the sandy fossiliferous packstone can be due to the heterogeneous composition of this lithofacies, and distribution of skeletal grains and sand grains along the thick massive body of the packstone (Figure 4-11). In contrary, the homogeneous composition of the oolitic skeletal grainstone and relatively of the stromatolite grainstone illustrates their permeability isotropy.

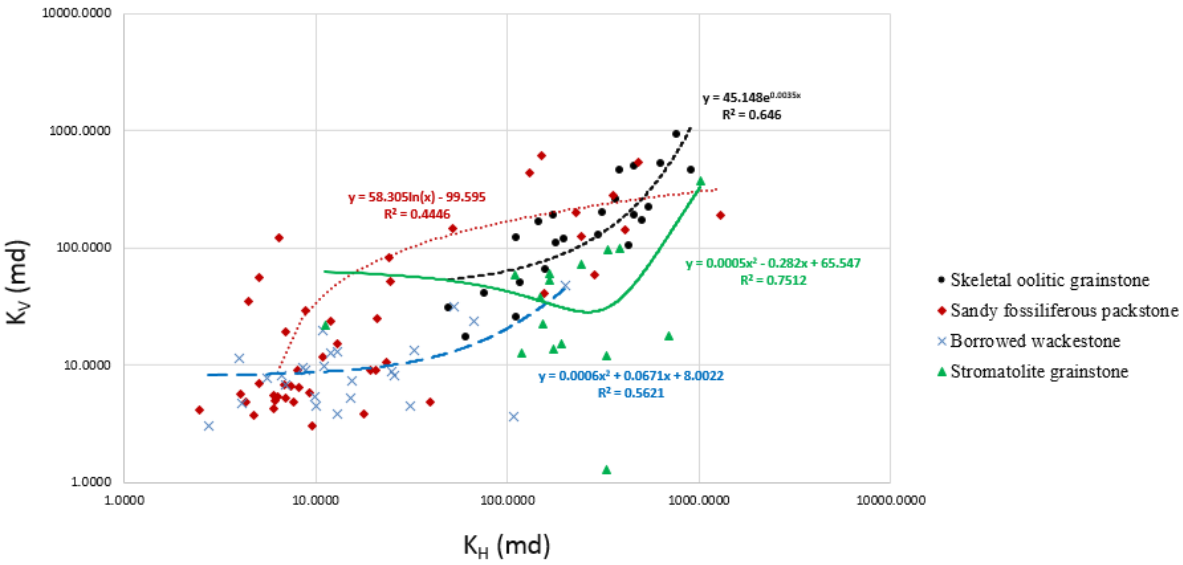


Figure 5-6: Cross-plot of the vertical versus horizontal permeabilities for the selected lithofacies of the Dam Formation in the studied outcrop

## 5.5 Geostatistical Modeling

### 5.5.1 Introduction

One of the tools that are commonly used for better facies and property characterization is simulation of these parameters in three dimensional view, in order to evaluate their distribution along and across the exposure. This part of the chapter talks about modeling of facies and reservoir properties (porosity and permeability) in three dimensional visualization. Petrel 2009® was used for this purpose. The final model was compared to the input data-sets, thus, the produced realizations were ranked against their matching to the input data.

### 5.5.2 Input Data

Since there are two types of models will be produced out of this work, the input datasets included two types. The first is the categorized datasets which belong to the sedimentary facies, and the second dataset is discrete variable, which is assigned to the porosity and permeability datasets. It is important to state that the 3D models of facies, porosity and permeability have been only applied on the main outcrop body (Figure 4-1, Enclosure 4-2), this is because it represents the best exposed, laterally and vertically continuous, and easily-sampled part of the Dam Formation in the study area. The basal skeletal oolitic grainstone was excluded from the 3D models due to its inadequate thickness for vertical variography, bedside the poor exposure of the layers above it. The input data is distributed as conventional measured sections across the two faces of the exposure. Most of the measured sections were taken from the northeastern face (Figure 5-7) due to its

good quality, and the easiness of sampling on this face comparing to the southwestern face. As a result of primary evaluation of facies heterogeneity in outcrop scale, the measured sections were distributed systematically since there is no clear lateral heterogeneity observed along the succession, except minor differences in the thickness.

### 5.5.3 Geometry modeling

The first step in each model is to construct the structural or geometry framework within which any property can be characterized. This framework can latterly act as a validity factor for the subsequent models. In order to construct a solid framework, detailed field measurements were carried out. These measurements includes: 1) exact coordinate location and elevation of each measured section, 2) composition and thickness of each lithofacies or bed, and 3) digitizing of a 2D polygon around the area of interest, based on the real map view of the studies outcrop. Also, a fine grid increment (1mX1m) was selected for surface construction in order to ensure the best geometry model that mimics the real geometry and architecture of the exposure in map view (Figure 5-8).

The geometry model composes of three building blocks:

1- Surfaces “horizons” which represent the top and/or bottom boundaries of the lithofacies or sedimentary packages. The surface can be a boundary between two lithofacies, two depositional environments, or can be a sequence boundary. In the current study, the surfaces were assigned to boundaries between lithofacies.

2- Zones: dividing the succession into intervals based on surfaces construction.

3- Layers: dividing each zones into layers based on field observations, the more the number of layers, the better the resolution of the model.

Due to low diversity of lithofacies representation in the main outcrop body of the study area, seven surfaces (six zones) were adopted for the geometry modeling (Figure 5-8, Table 5-3). Mostly, as in subsurface petroleum fields, the selection criteria of these surfaces should be based on the stratigraphic surfaces or abrupt contacts of different rock properties. However in this study, due to low vertical diversity of the lithofacies and small thickness of the exposure, the selection criteria of these surfaces is influenced by the petrophysical purpose of the research, and the purpose of detailed characterization of porosity and permeability for selected lithofacies. In this context, the stromatolite grainstone was divided into two layers (upper and lower), the burrowed wackestone into two layers (upper and lower), and the sandy fossiliferous packstone into three layers (upper, middle, and lower) (Figure 5-9B). Since this research is targeting lower scale of heterogeneity, gridding of the geometry model followed the requirements of outcrop scale heterogeneity. Accordingly, a fine grid of 0.15m X 0.15m were selected (Figure 5-9A). It is important to mention that the following geometry model is built based on outcrop status, the bottom curvatures don't reflect any geological structure or pinching out of the layers, it just explains the differential talus and eolian sand cover, which led to differences in the lengths of the measured sections around the outcrop in the study area, and then created the curvatures at the bottom of the outcrop model (Figure 5-8, 5-9).

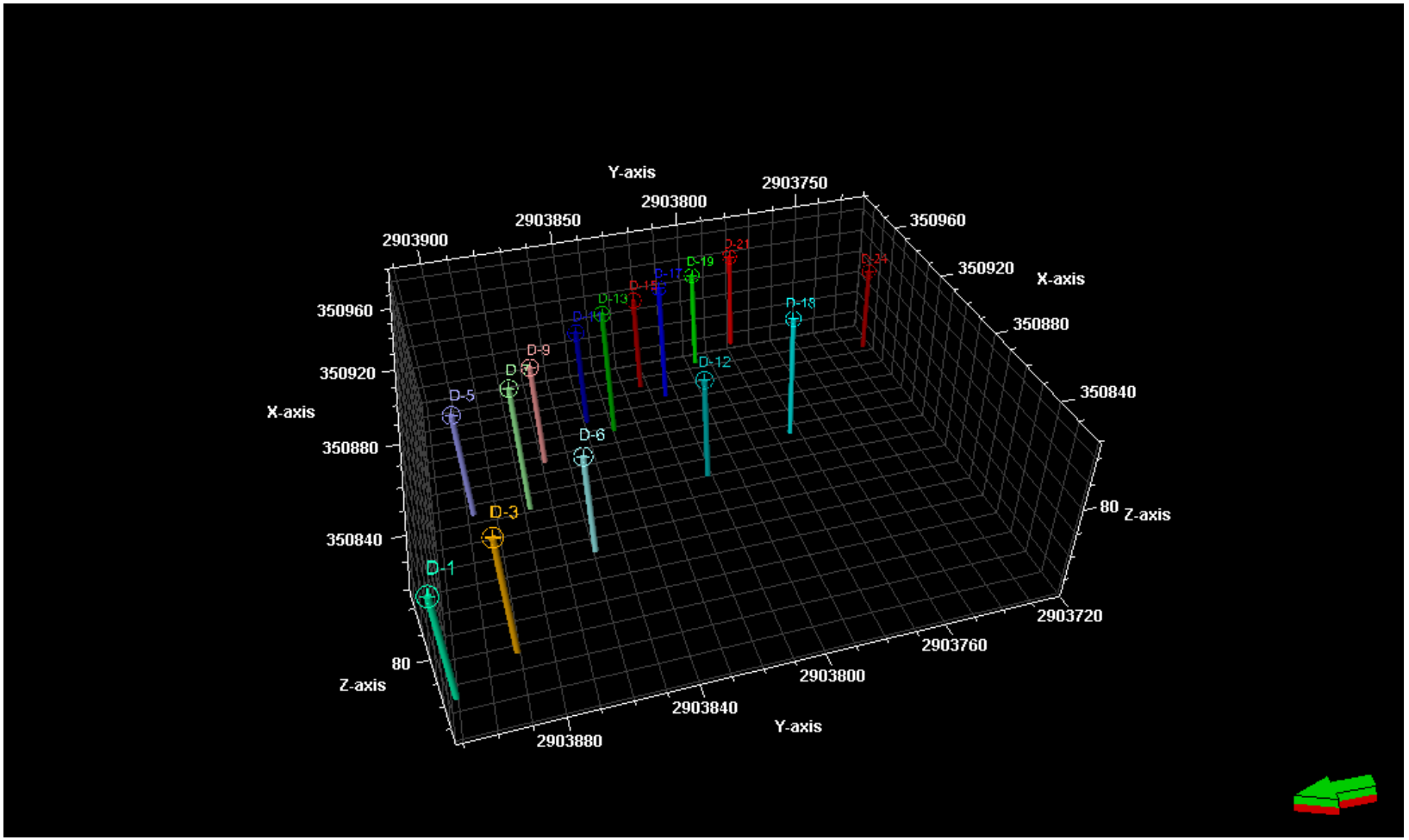


Figure 5-7: Distribution of the 15 measured sections used for structure and facies modeling

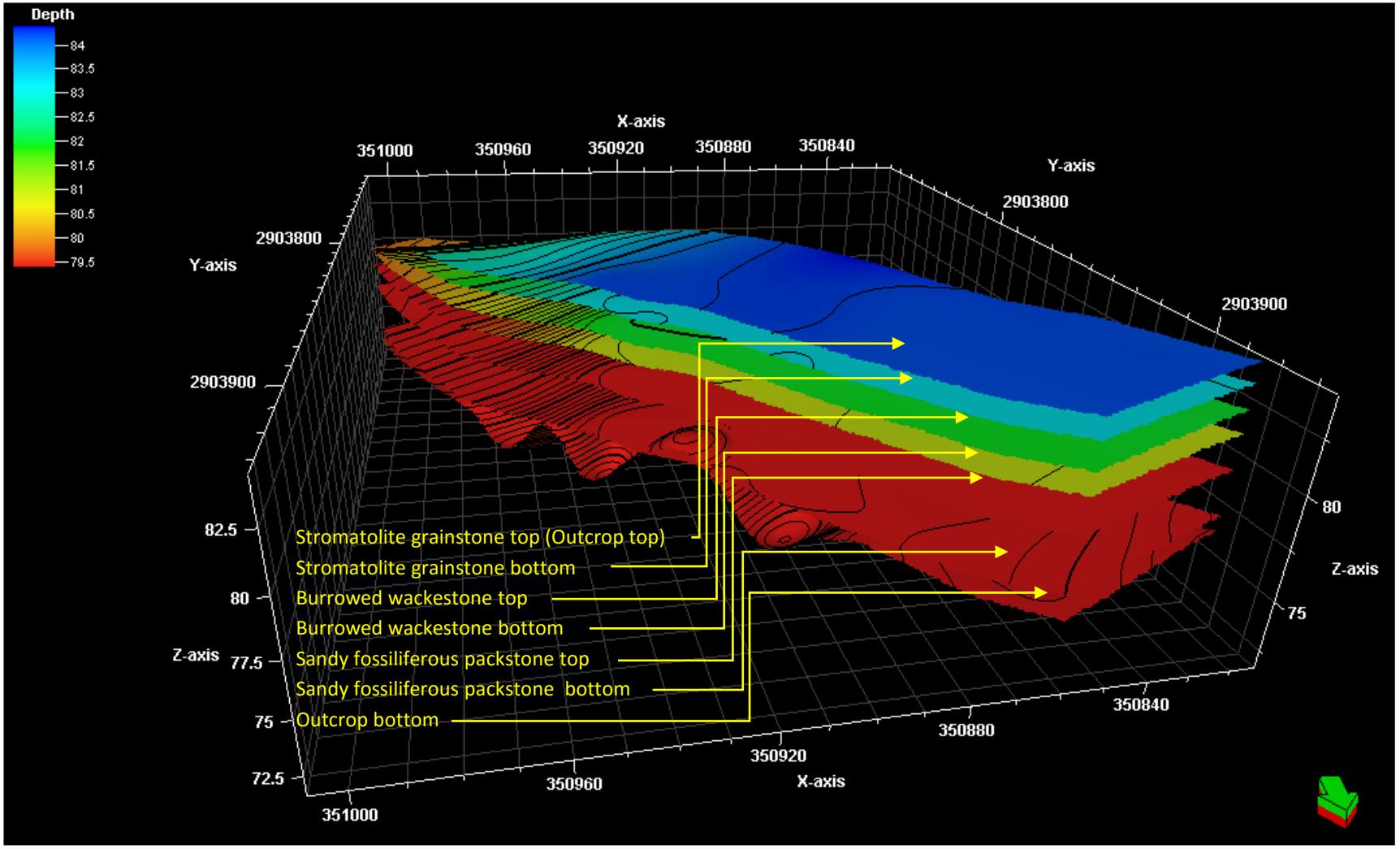


Figure 5-8: 3D view of the seven surfaces (horizons) representing the building framework of the geometry model

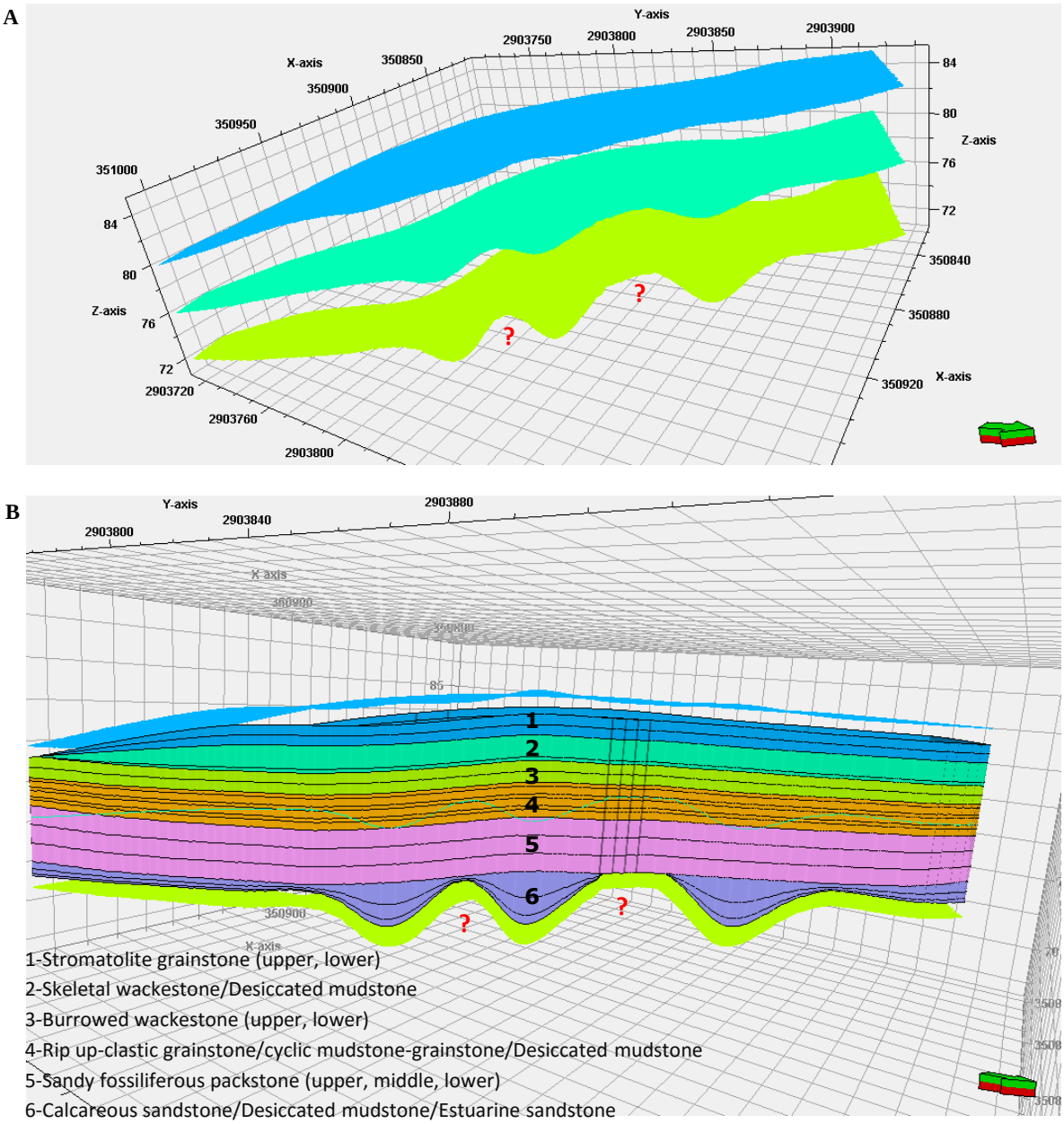


Figure 5-9: A: High-resolution skeleton grid of the study area. B: layering of the vertical succession within each zone

Table 5-3: Distribution of lithofacies layers per zones

| Gridding System | Lithofacies zone | No. of cells | Average thickness (m) | No. of layers per section |
|---|---|---|---|---|
| Zone-1 grid | Stromatolite grainstone | 1306763 | 0.92 | 2 |
| Zone-2 grid | Skeletal wackestone | 717258 | 1.07 | 1 |
| Zone-2 grid | Desiccated mudstone | 1493707 | 0.44 | 3 |
| Zone-3 grid | Burrowed wackestone | 1334550 | 1.01 | 2 |
| Zone-4 grid | Rip up-clastic oolitic grainstone | 618836 | 0.24 | 1 |
| Zone-4 grid | Oolitic peloidal grainstone | 1391033 | 0.31 | 2 |
| Zone-4 grid | Sandy mudstone | 1436256 | 0.18 | 2 |
| Zone-5 grid | Sandy fossiliferous packstone | 2001825 | 2.71 | 3 |
| Zone-6 grid | Calcareous sandstone | 1151774 | 1.34 | 1 |
| Zone-6 grid | Estuarine sandstone | 446804 | 0.48 | 1 |

### 5.5.4 Facies Modeling

The sequential indicator simulation (SIS) was utilized to produce facie model of the lithofacies representation of the main outcrop body in the study area (Figure 5-16A). The conventional field investigations, and the subsequent petrographic analyses revealed a maximum of 10 lithofacies across the main outcrop of the Miocene Dam Formation in the studied outcrop. These lithofacies were distributed into 14 layers across the outcrop. However, for the modeling, some of these lithofacies were further subdivided into two or three beds as mentioned earlier, and this resulted in a maximum of 18 beds (Figure 5-9B). The lowermost lithofacies are not exposed in most of the sections (Figure 5-9B, 5-16A). The facies model represents the framework of the properties modeling. From this model, three of the four selected lithofacies were further modeled for porosity and permeability.

**Indicator Variography of lithofacies**

Experimental indicator semivariograms were constructed for each zone in the study area. These variograms were computed using thickness of each zone in the measured section, and then were up-scaled to the size of the grid cells in the geometry model. The upscaled logs were modeled by sequential indicator simulation (SIS) in a later stage. Since the model is utilizing data distributed in three dimensional view, the variograms were computed in three dimension. These directions includes the major direction along the strike of exposed strata (NW-SE), the minor direction perpendicular to the major direction (NE-SW), and the vertical direction across the outcrop. The experimental semivariograms were examined against the well-known theoretical models (exponential, gaussian, and spherical models) to select the best fit and best variogram parameters for each zone. The best fit was obtained by selecting the spherical model for all lithofacies (Figures 5-10 to 5-15). The experimental semivariograms included the six zones of lithofacies. In general, the semivariograms of major and minor directions are better represented comparing to the vertical semivariogram, this is due to the limited data in vertical direction, which corresponds with limited number of lithofacies in the succession of the main body of outcrop. The anisotropy analysis of these semivariograms showed geometry anisotropy in which there is contrast between major and minor range.

**Zone-1 (stromatolite grainstone)**

The semivariogram of both of the upper and lower stromatolite grainstone showed a good shape, with almost similar sill in both, the major direction (NW-SE) and minor direction (NE-SW). However the sill value is relatively larger in the vertical direction (Figure 5-10).

**Zone-2 (skeletal wackestone and desiccated mudstone)**

In the second zone, the two horizontal variograms are fairly close to each other. The ratio of the major range to the minor range, and the nugget effect are less than that of the stromatolite grainstone zone (Figure 5-11).

**Zone-3 (burrowed wackestone)**

The variogram of burrowed wackestone is poor. The major direction showed flat variogram with almost similar sill and nugget values (Figure 5-12).

**Zone-4 (rip up-clastic grainstone, rhythmite succession and desiccated mudstone)**

Variograms of the rhythmite layering unit showed good shape, with relatively low nugget effect. This zone has a good vertical variability since it is composed of several, thin beds (Figure 5-13).

**Zone-5 (sandy fossiliferous packstone)**

The variogram architecture of the fossiliferous packstone zone is closely similar to that of burrowed wackestone, as both zones were divided into more layers. The only exception is that the sandy fossiliferous packstone has better shape because it was divided into three layers, comparing to only two layers for burrowed wackestone (Figure 5-14).

**Zone-6 (calcareous sandstone, desiccated mudstone and estuarine sandstone)**

Comparing to the variability patterns of the rhythmite mudstone-grainstone, the variogram of the bottom zone showed poor shape in the major direction, with great contrast between the two horizontal ranges. This can be attributed to low representation of these lithofacies along the exposure (Figure 5-15).

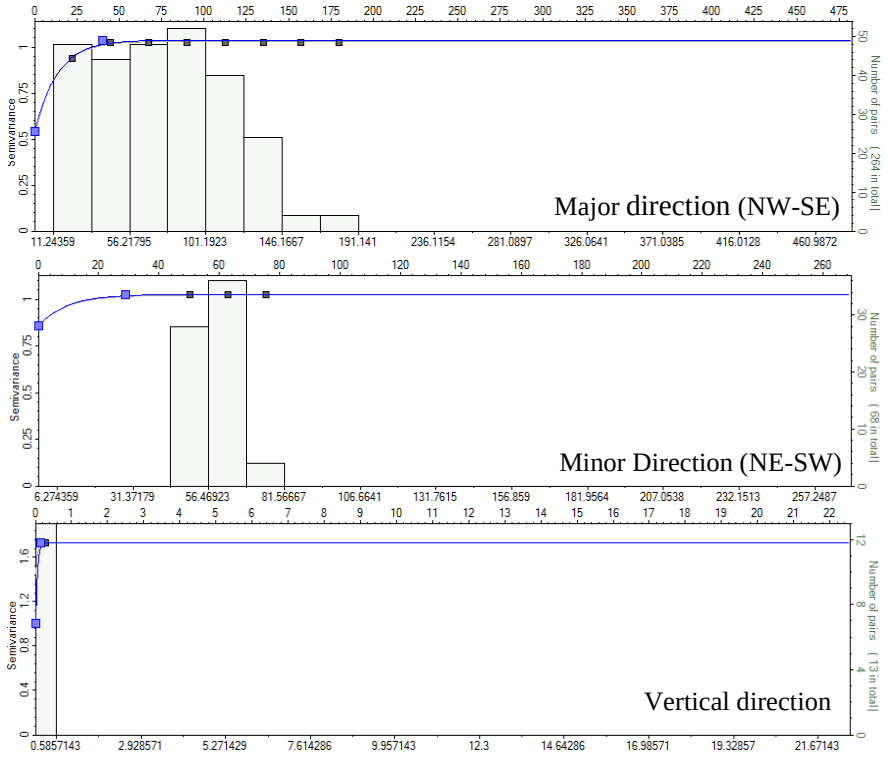


Figure 5-10: Indicator semivariograms of zone-1

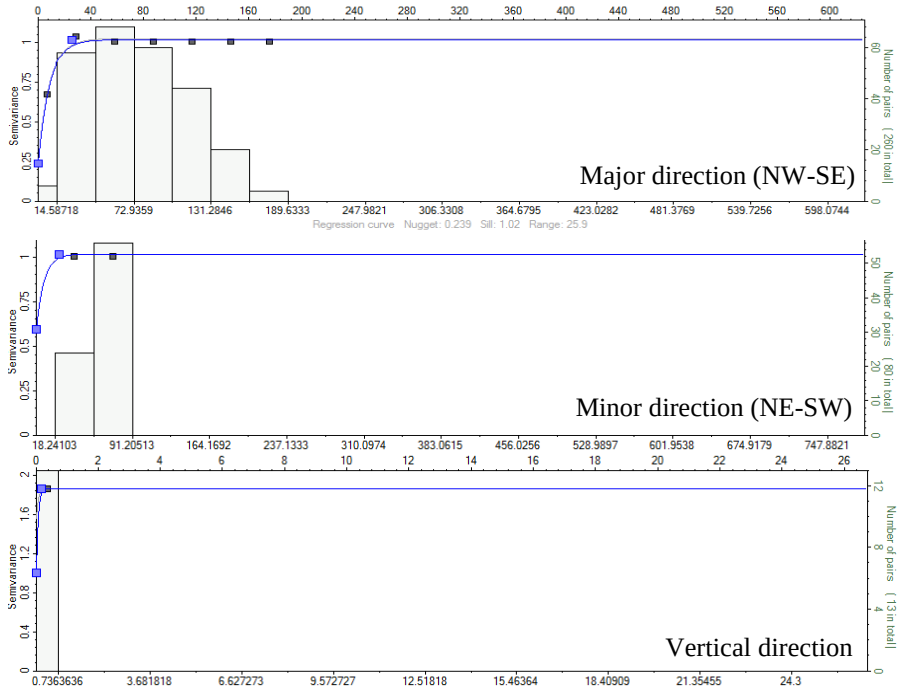


Figure 5-11: Indicator semivariograms of zone-2

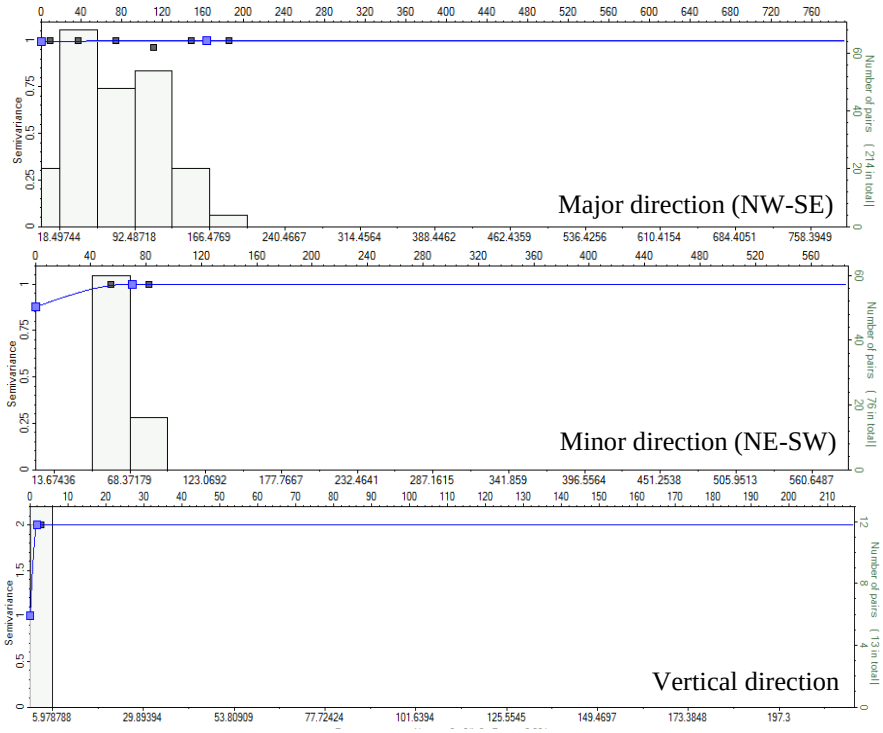


Figure 5-12: Indicator semivariograms of zone-3

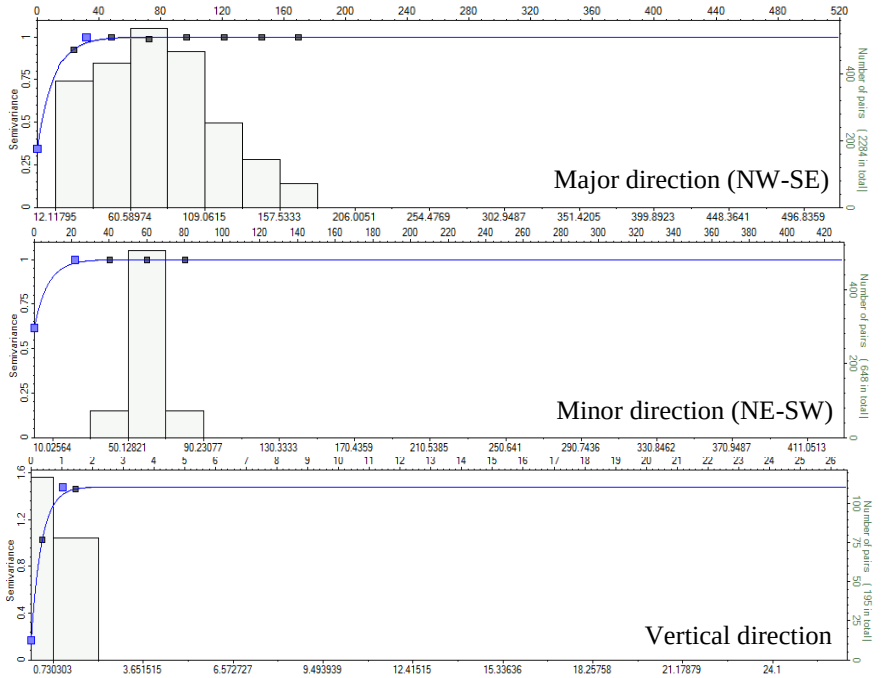


Figure 5-13: Indicator semivariograms of zone-4

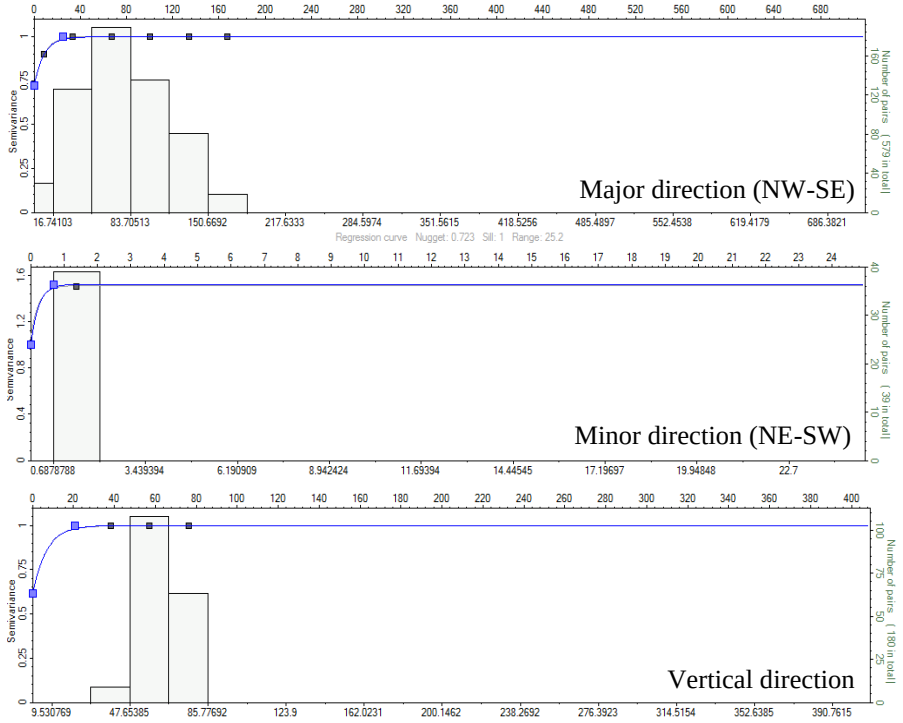


Figure 5-14: Indicator semivariograms of zone-5

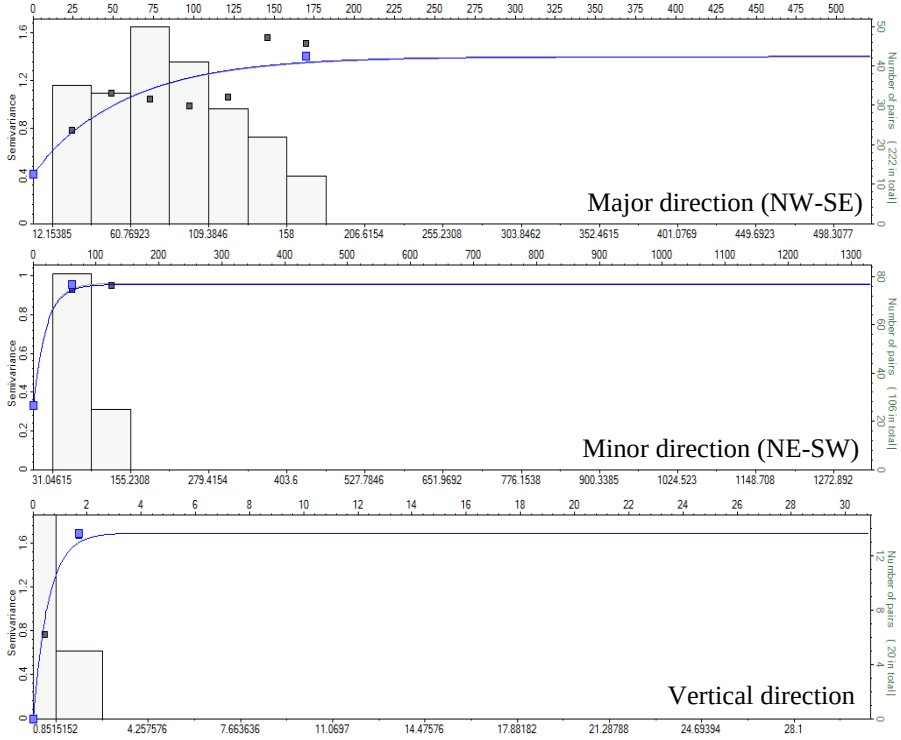


Figure 5-15: Indicator semivariograms of zone-6

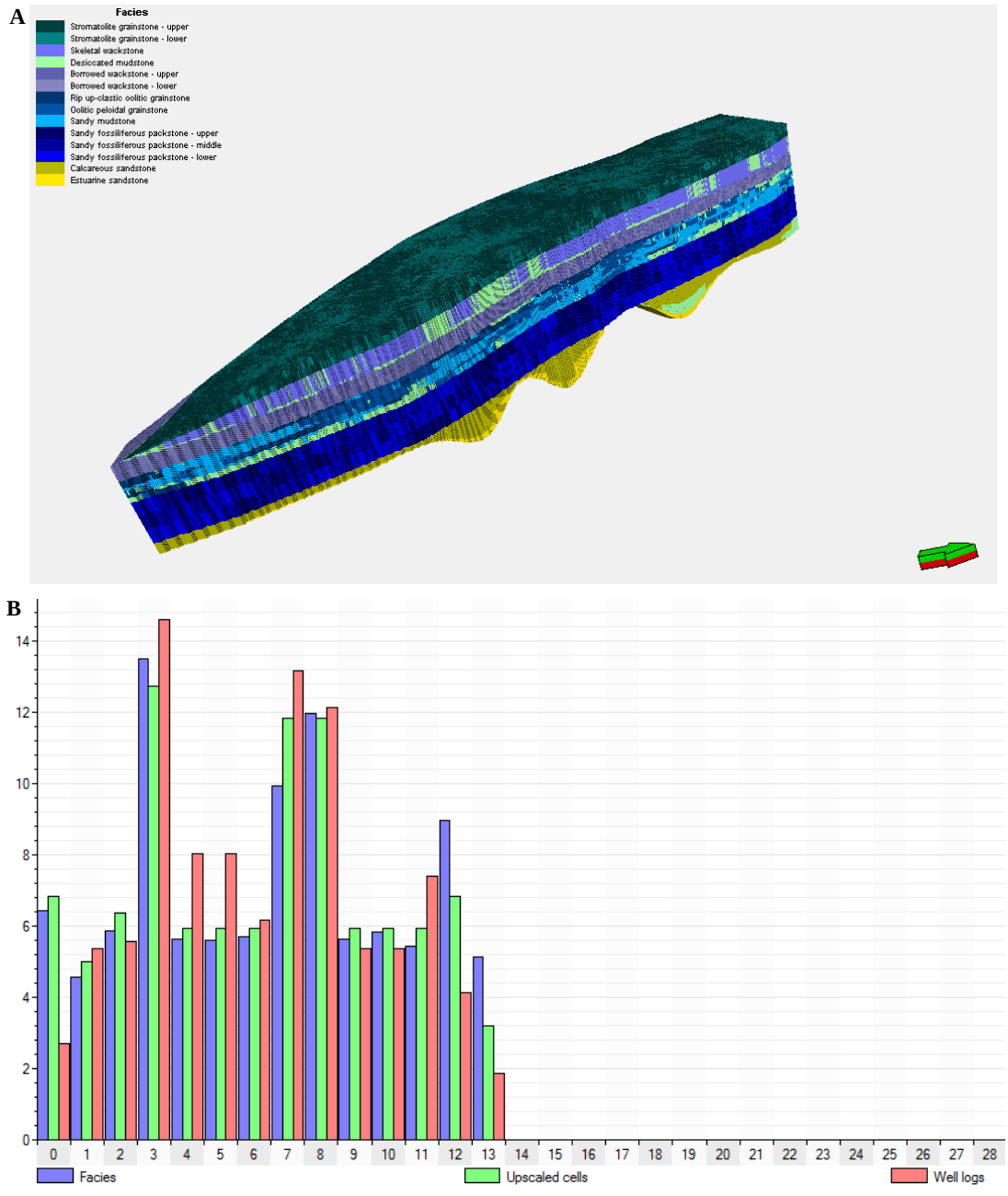


Figure 5-16: A: 3D view of the lithofacies model of the study outcrop. B: Histogram of facies model compared to the input and upscaled facies.

## Validation of the Lithofacies Model

The 3D lithofacies model is based on 15 scattered measured sections. Therefore, it is vital to validate this model in order to examine its applicability for simulation of the real geology of study area. Two methods of validation can be adopted, the quantitative and qualitative. The quantitative method can be attained by comparing the output realizations with the input lithofacies framework, and then ranking those realizations on the basis of their proximity to the input data. In this context, five top-ranked realizations were obtained out of 40 lithofacies realizations. These realizations showed a great match to the upscaling output of input data (Table 5-4, Figure 5-17). Regarding the qualitative validation, the process is based on visual similarity test of input lithofacies to the upscaled lithofacies, and to the model itself. As a result, a good match was observed between the input on one hand, and both of upscaled lithofacies (Figure 5-18A, B), and model view (Figure 5-18C) on the other hand. This validation represents a visualization of the quantitative validation. Better validation can be achieved when comparing the model to the present-day topography, geometry and lithofacies setting. As a result, it was found that the distribution of the seven surfaces of the Dam Formation in the study area is fairly resembled their distribution in outcrop scale (Figure 5-19). Moreover, a better qualitative validation can be attained by direct comparison of the high resolution pictures of the outcrop with the model. This could be accomplished by comparing the least represented lithofacies such as that of Zone 6 (the estuarine sandstone, the desiccated mudstone, and the calcareous sandstone), with the lithofacies model. The results showed an acceptable accordance with the model (Figure 5-20). In addition, comparing these

realizations with each other produced same distribution with fairly same trend between the input, upscaled, and modeled facies (Figure 5-16B, 5-21).

Table 5-4: Summary of simple statistics of the upscaled lithofacies and the top-five ranked realizations

| Ups. / R. | Code | Name | % | Min. | Mean | Max. | Std. |
|---|---|---|---|---|---|---|---|
| **Upscaled Facies** | 0 | Stromatolite grainstone (U) | 6.82 | 0.5 (1) | 0.6 (1.15) | 1.0 (2) | 0.1849 |
| | 1 | Stromatolite grainstone (L) | 5 | 0.5 (1) | 0.5 (1) | 0.5 (1) | 0.01929 |
| | 2 | Skeletal wackestone | 6.36 | 1.0 (1) | 1.1 (1.08) | 1.1 (2) | 0.02442 |
| | 3 | Desiccated mudstone | 12.73 | 0.2 (1) | 0.3 (1.04) | 1.0 (2) | 0.2018 |
| | 4 | Burrowed wackestone (U) | 5.91 | 0.5 (1) | 0.5 (1) | 0.6 (1) | 0.02235 |
| | 5 | Burrowed wackestone (L) | 5.91 | 0.5 (1) | 0.5 (1) | 0.6 (1) | 0.02235 |
| | 6 | Rip up-clastic oolitic grainstone | 5.91 | 0.2 (1) | 0.2 (1) | 0.2 (1) | 0.001919 |
| | 7 | Oolitic peloidal grainstone | 11.82 | 0.4 (1) | 0.4 (1) | 0.4 (1) | 0.003837 |
| | 8 | Sandy mudstone | 11.82 | 0.2 (1) | 0.2 (1) | 0.2 (1) | 0.001919 |
| | 9 | Sandy fossiliferous packstone (U) | 5.91 | 0.9 (1) | 0.9 (1) | 0.9 (1) | 0.005726 |
| | 10 | Sandy fossiliferous packstone (M) | 5.91 | 0.9 (1) | 0.9 (1) | 0.9 (1) | 0.005725 |
| | 11 | Sandy fossiliferous packstone (L) | 5.91 | 0.9 (1) | 0.9 (1) | 0.9 (1) | 0.005726 |
| | 12 | Calcareous sandstone | 6.82 | 0.4 (1) | 0.9 (1.5) | 1.6 (2) | 0.4599 |
| | 13 | Estuarine sandstone | 3.18 | 0.5 (1) | 1.2 (1.75) | 1.6 (2) | 0.4212 |
| **Realiz.30** | 0 | Stromatolite grainstone (U) | 6.82 | 0.5 (1) | 0.6 (1.15) | 1.0 (2) | 0.1849 |
| | 1 | Stromatolite grainstone (L) | 5 | 0.5 (1) | 0.5 (1) | 0.5 (1) | 0.01929 |
| | 2 | Skeletal wackestone | 6.36 | 1.0 (1) | 1.1 (1.08) | 1.1 (2) | 0.02442 |
| | 3 | Desiccated mudstone | 12.73 | 0.2 (1) | 0.3 (1.04) | 1.0 (2) | 0.2018 |
| | 4 | Burrowed wackestone (U) | 5.91 | 0.5 (1) | 0.5 (1) | 0.6 (1) | 0.02235 |
| | 5 | Burrowed wackestone (L) | 5.91 | 0.5 (1) | 0.5 (1) | 0.6 (1) | 0.02235 |
| | 6 | Rip up-clastic oolitic grainstone | 5.91 | 0.2 (1) | 0.2 (1) | 0.2 (1) | 0.001919 |
| | 7 | Oolitic peloidal grainstone | 11.82 | 0.4 (1) | 0.4 (1) | 0.4 (1) | 0.003837 |
| | 8 | Sandy mudstone | 11.82 | 0.2 (1) | 0.2 (1) | 0.2 (1) | 0.001919 |
| | 9 | Sandy fossiliferous packstone (U) | 5.91 | 0.9 (1) | 0.9 (1) | 0.9 (1) | 0.005726 |
| | 10 | Sandy fossiliferous packstone (M) | 5.91 | 0.9 (1) | 0.9 (1) | 0.9 (1) | 0.005725 |
| | 11 | Sandy fossiliferous packstone (L) | 5.91 | 0.9 (1) | 0.9 (1) | 0.9 (1) | 0.005726 |
| | 12 | Calcareous sandstone | 6.82 | 0.4 (1) | 0.9 (1.5) | 1.6 (2) | 0.4599 |
| | 13 | Estuarine sandstone | 3.18 | 0.5 (1) | 1.2 (1.75) | 1.6 (2) | 0.4212 |

| Ups. / R. | Code | Name | % | Min. | Mean | Max. | Std. |
|---|---|---|---|---|---|---|---|
| **Realiz.7** | 0 | Stromatolite grainstone (U) | 6.21 | 0.0 (1) | 0.6 (1.39) | 1.1 (2) | 0.2736 |
| | 1 | Stromatolite grainstone (L) | 4.77 | 0.0 (1) | 0.6 (1.27) | 1.1 (2) | 0.2531 |
| | 2 | Skeletal wackestone | 5.88 | 0.0 (1) | 0.8 (1.38) | 1.3 (2) | 0.4454 |
| | 3 | Desiccated mudstone | 11.18 | 0.0 (1) | 0.5 (1.3) | 1.8 (6) | 0.3956 |
| | 4 | Burrowed wackestone (U) | 5.6 | 0.3 (1) | 0.7 (1.33) | 1.2 (2) | 0.2573 |
| | 5 | Burrowed wackestone (L) | 5.62 | 0.3 (1) | 0.7 (1.33) | 1.2 (2) | 0.2573 |
| | 6 | Rip up-clastic oolitic grainstone | 5.17 | 0.2 (1) | 0.4 (1.28) | 1.8 (6) | 0.1998 |
| | 7 | Oolitic peloidal grainstone | 11.6 | 0.2 (1) | 0.5 (1.73) | 1.8 (6) | 0.2947 |
| | 8 | Sandy mudstone | 11.94 | 0.2 (1) | 0.5 (1.65) | 1.8 (6) | 0.2963 |
| | 9 | Sandy fossiliferous packstone (U) | 5.37 | 0.8 (1) | 1.2 (1.26) | 3.3 (3) | 0.4964 |
| | 10 | Sandy fossiliferous packstone (M) | 5.96 | 0.8 (1) | 1.2 (1.32) | 3.3 (3) | 0.5464 |
| | 11 | Sandy fossiliferous packstone (L) | 5.49 | 0.8 (1) | 1.2 (1.28) | 3.3 (3) | 0.516 |
| | 12 | Calcareous sandstone | 8.92 | 0.0 (1) | 0.7 (1.73) | 2.6 (3) | 0.4646 |
| | 13 | Estuarine sandstone | 6.29 | 0.0 (1) | 0.9 (1.81) | 3.2 (3) | 0.7433 |
| **Realiz.16** | 0 | Stromatolite grainstone (U) | 6 | 0.0 (1) | 0.6 (1.38) | 1.1 (2) | 0.2768 |
| | 1 | Stromatolite grainstone (L) | 4.98 | 0.0 (1) | 0.6 (1.3) | 1.1 (2) | 0.2525 |
| | 2 | Skeletal wackestone | 5.7 | 0.0 (1) | 0.9 (1.38) | 1.4 (2) | 0.4404 |
| | 3 | Desiccated mudstone | 13.8 | 0.0 (1) | 0.5 (1.38) | 1.8 (6) | 0.3753 |
| | 4 | Burrowed wackestone (U) | 5.62 | 0.3 (1) | 0.7 (1.33) | 1.2 (2) | 0.2578 |
| | 5 | Burrowed wackestone (L) | 5.59 | 0.3 (1) | 0.7 (1.33) | 1.2 (2) | 0.2572 |
| | 6 | Rip up-clastic oolitic grainstone | 5.71 | 0.2 (1) | 0.4 (1.34) | 1.8 (6) | 0.2059 |
| | 7 | Oolitic peloidal grainstone | 10.49 | 0.2 (1) | 0.5 (1.62) | 1.8 (6) | 0.2882 |
| | 8 | Sandy mudstone | 10.91 | 0.2 (1) | 0.5 (1.62) | 1.8 (6) | 0.2909 |
| | 9 | Sandy fossiliferous packstone (U) | 5.58 | 0.8 (1) | 1.2 (1.27) | 3.3 (3) | 0.5094 |
| | 10 | Sandy fossiliferous packstone (M) | 5.78 | 0.8 (1) | 1.2 (1.32) | 3.2 (3) | 0.5331 |
| | 11 | Sandy fossiliferous packstone (L) | 5.46 | 0.8 (1) | 1.2 (1.26) | 3.2 (3) | 0.5052 |
| | 12 | Calcareous sandstone | 8.64 | 0.0 (1) | 0.8 (1.7) | 3.1 (3) | 0.5163 |
| | 13 | Estuarine sandstone | 5.74 | 0.0 (1) | 0.7 (1.54) | 3.3 (3) | 0.6461 |

| Ups./ R. | Code | Name | % | Min. | Mean | Max. | Std. |
|---|---|---|---|---|---|---|---|
| **Realiz.21** | 0 | Stromatolite grainstone (U) | 6.4 | 0.5 (1) | 0.6 (1.15) | 1.0 (2) | 0.1849 |
| | 1 | Stromatolite grainstone (L) | 4.58 | 0.5 (1) | 0.5 (1) | 0.5 (1) | 0.01929 |
| | 2 | Skeletal wackestone | 6.03 | 1.0 (1) | 1.1 (1.08) | 1.1 (2) | 0.02442 |
| | 3 | Desiccated mudstone | 12.55 | 0.2 (1) | 0.3 (1.04) | 1.0 (2) | 0.2018 |
| | 4 | Burrowed wackestone (U) | 5.61 | 0.5 (1) | 0.5 (1) | 0.6 (1) | 0.02235 |
| | 5 | Burrowed wackestone (L) | 5.6 | 0.5 (1) | 0.5 (1) | 0.6 (1) | 0.02235 |
| | 6 | Rip up-clastic oolitic grainstone | 5.2 | 0.2 (1) | 0.2 (1) | 0.2 (1) | 0.001919 |
| | 7 | Oolitic peloidal grainstone | 11.69 | 0.4 (1) | 0.4 (1) | 0.4 (1) | 0.003837 |
| | 8 | Sandy mudstone | 12.07 | 0.2 (1) | 0.2 (1) | 0.2 (1) | 0.001919 |
| | 9 | Sandy fossiliferous packstone (U) | 5.73 | 0.9 (1) | 0.9 (1) | 0.9 (1) | 0.005726 |
| | 10 | Sandy fossiliferous packstone (M) | 5.54 | 0.9 (1) | 0.9 (1) | 0.9 (1) | 0.005725 |
| | 11 | Sandy fossiliferous packstone (L) | 5.55 | 0.9 (1) | 0.9 (1) | 0.9 (1) | 0.005726 |
| | 12 | Calcareous sandstone | 9.68 | 0.4 (1) | 0.9 (1.5) | 1.6 (2) | 0.4599 |
| | 13 | Estuarine sandstone | 3.76 | 0.5 (1) | 1.2 (1.75) | 1.6 (2) | 0.4212 |
| **Realiz.3** | 0 | Stromatolite grainstone (U) | 6.59 | 0.0 (1) | 0.7 (1.42) | 1.1 (2) | 0.2793 |
| | 1 | Stromatolite grainstone (L) | 4.39 | 0.0 (1) | 0.6 (1.24) | 1.1 (2) | 0.2428 |
| | 2 | Skeletal wackestone | 6.2 | 0.0 (1) | 0.9 (1.38) | 1.3 (2) | 0.4259 |
| | 3 | Desiccated mudstone | 12.29 | 0.0 (1) | 0.5 (1.32) | 1.8 (6) | 0.3727 |
| | 4 | Burrowed wackestone (U) | 5.59 | 0.3 (1) | 0.7 (1.33) | 1.2 (2) | 0.2571 |
| | 5 | Burrowed wackestone (L) | 5.63 | 0.3 (1) | 0.7 (1.34) | 1.2 (2) | 0.2579 |
| | 6 | Rip up-clastic oolitic grainstone | 5.61 | 0.2 (1) | 0.4 (1.31) | 1.8 (6) | 0.2026 |
| | 7 | Oolitic peloidal grainstone | 10.68 | 0.2 (1) | 0.5 (1.63) | 1.8 (6) | 0.2895 |
| | 8 | Sandy mudstone | 12.07 | 0.2 (1) | 0.5 (1.72) | 1.8 (6) | 0.3272 |
| | 9 | Sandy fossiliferous packstone (U) | 5.57 | 0.8 (1) | 1.2 (1.28) | 3.2 (3) | 0.5102 |
| | 10 | Sandy fossiliferous packstone (M) | 5.57 | 0.8 (1) | 1.2 (1.29) | 3.3 (3) | 0.5226 |
| | 11 | Sandy fossiliferous packstone (L) | 5.68 | 0.8 (1) | 1.2 (1.28) | 3.2 (3) | 0.5137 |
| | 12 | Calcareous sandstone | 8.42 | 0.0 (1) | 0.8 (1.57) | 2.6 (3) | 0.4361 |
| | 13 | Estuarine sandstone | 5.7 | 0.0 (1) | 0.6 (1.45) | 1.6 (3) | 0.4483 |

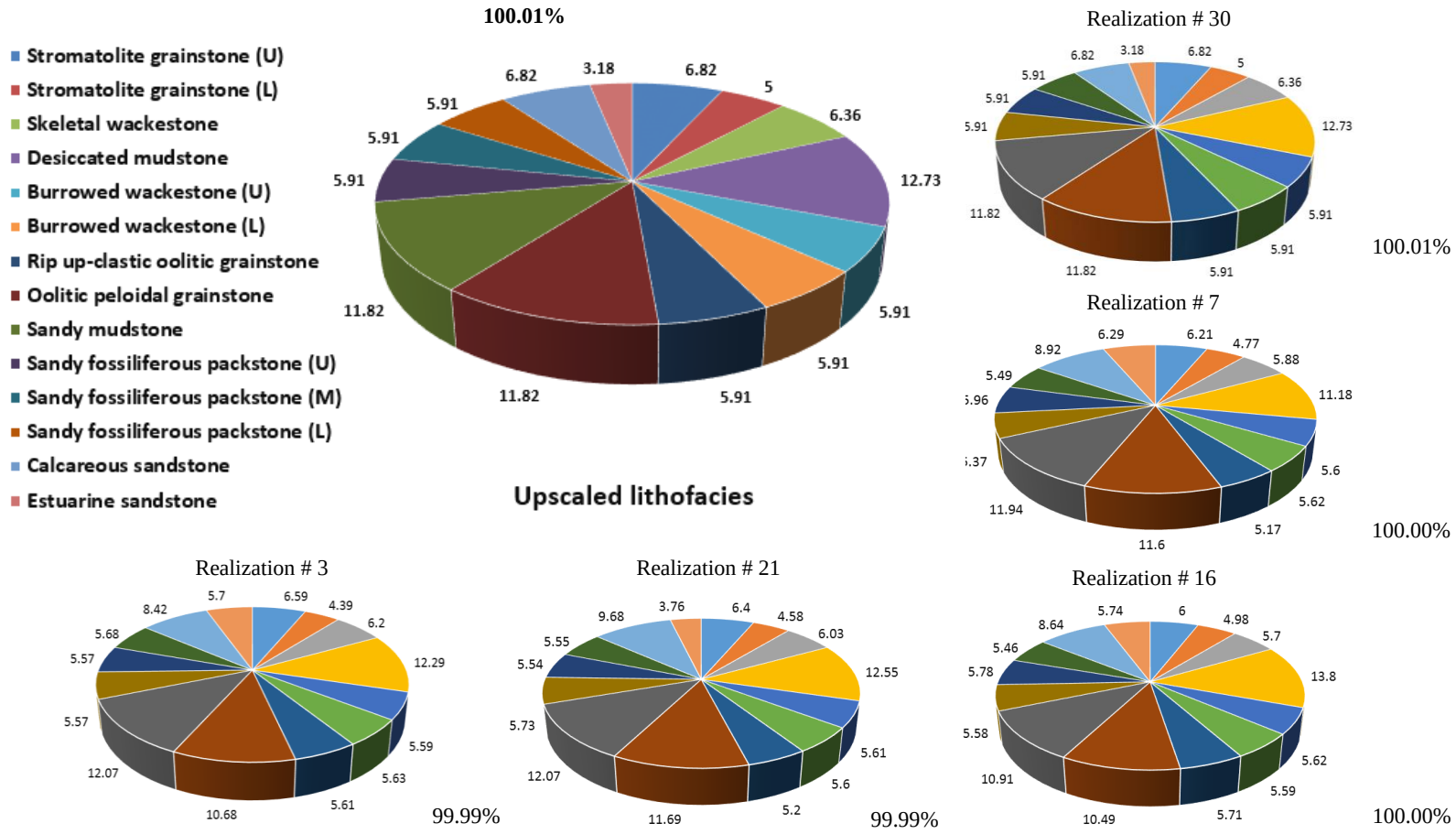


Figure 5-17: Top 5-ranked lithofacies realizations compared with the upscale lithofacies percentages of the input datasets

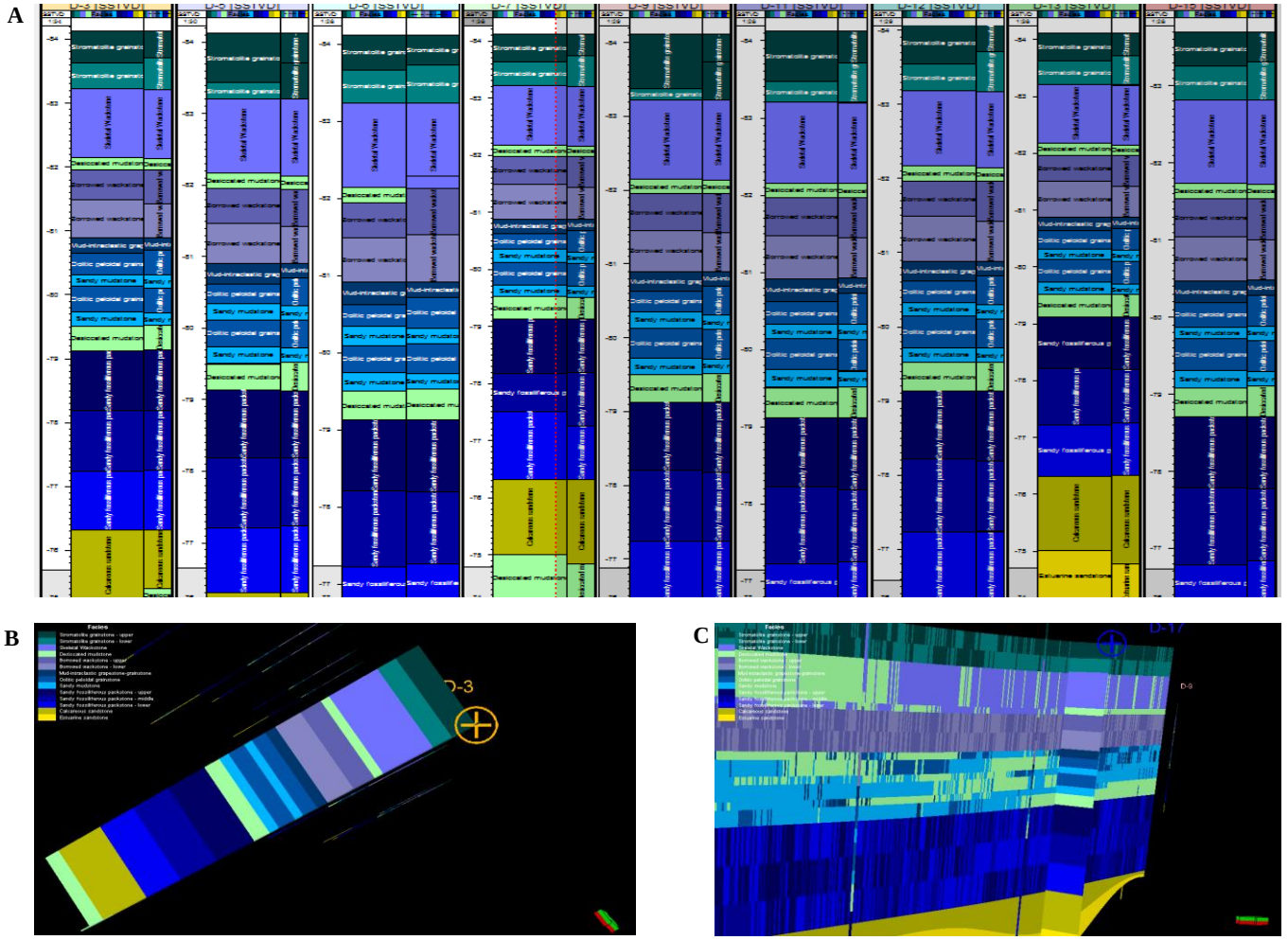


Figure 5-18: Qualitative facies model validation: A: Lithofacies of selected measured sections compared to their upscaled lithofacies, B: In model view. C: Validating model cross section with the input lithofacies

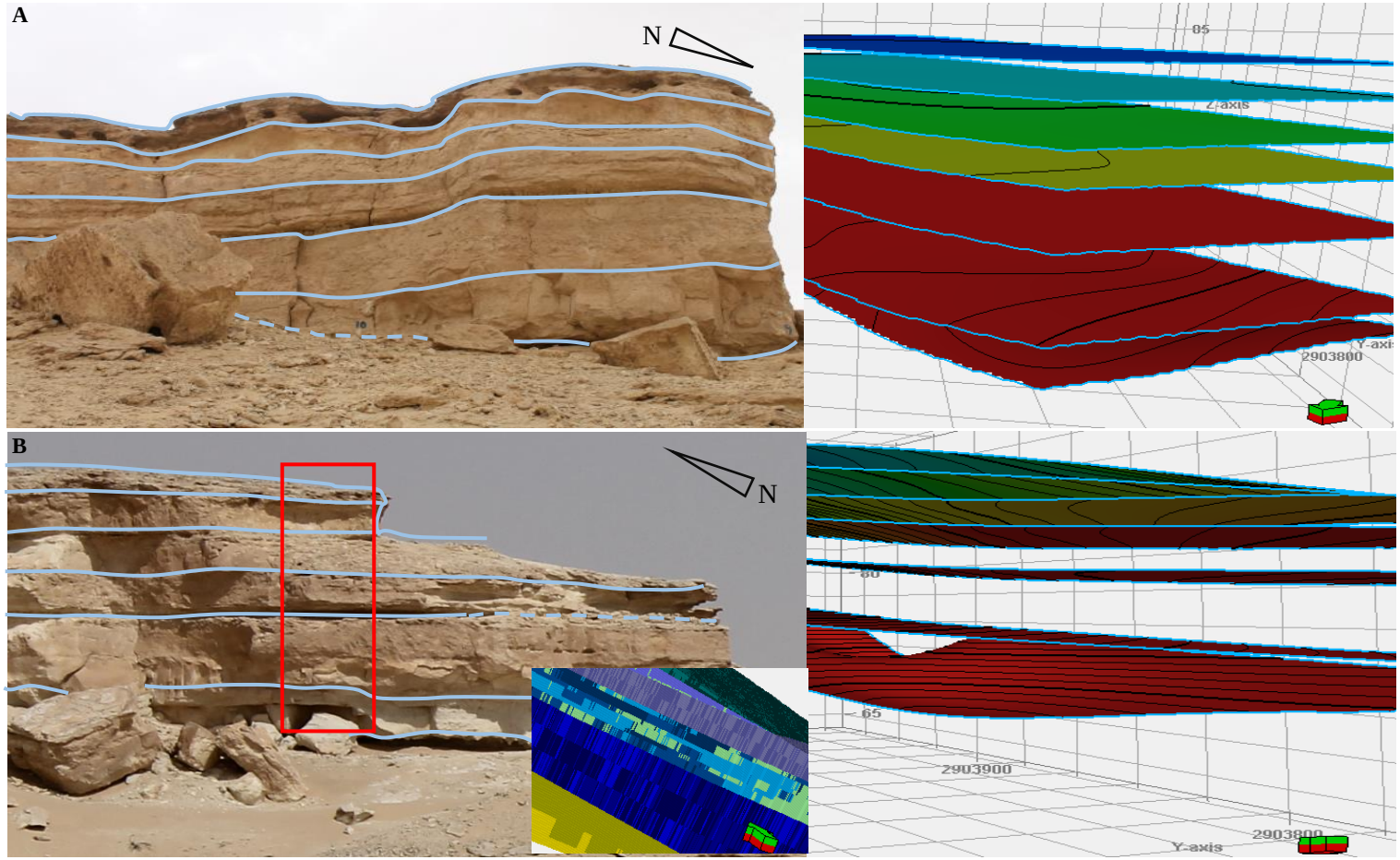


Figure -19: Comparing outcrop with the geometry model: surfaces of lithofacies zones in the northwestern part (A), and southeastern part (B) of outcrop compared to their equivalent surfaces in geometry model

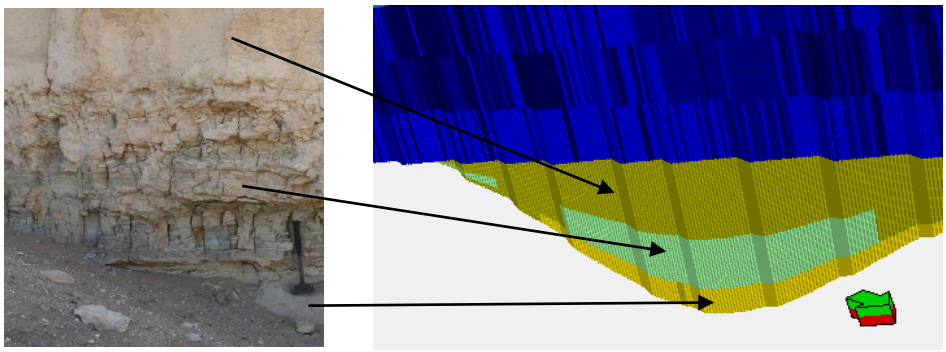

Figure 5-20: Comparing the real outcrop facies distribution with the facies model: outcrop view compared with a slice from lithofacies model. Outcrop photo was used for model validation. The lithofacies includes, from bottom to top, the estuarine sandstone, desiccated mudstone, and calcareous sandstone.

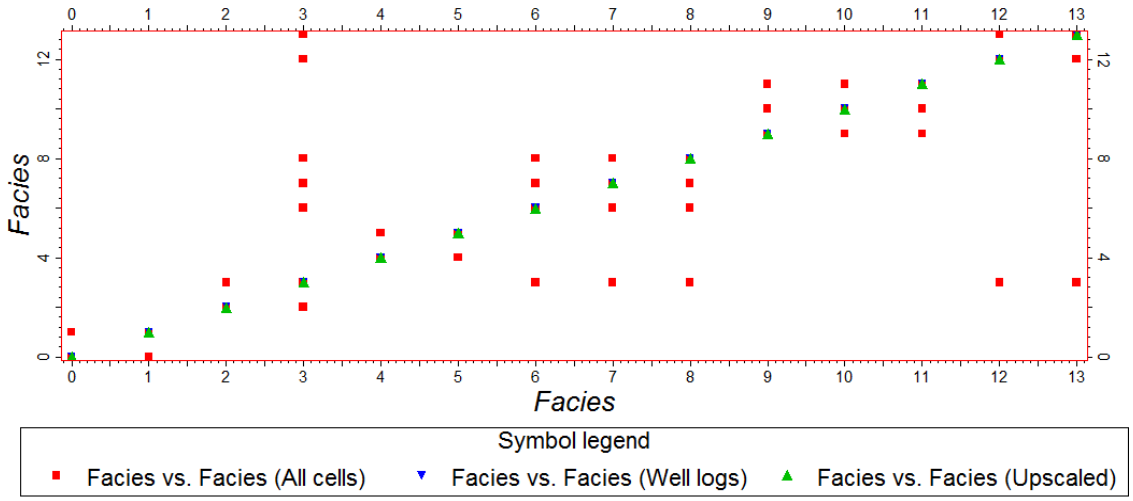


Figure 5-21: Cross-correlation between two realizations showing distribution of fair trend to the input and upscaled lithofacies

### 5.5.5 Property Modeling

The second modeling task of this study was the sequential gaussian simulation (SGS). Since the sedimentary facies is the main factor that controls the distribution of porosity

and permeability (Sahin et al., 1998), these parameters are expected to vary with facies over short distances. The property modeling of this research includes 3D porosity and permeability models represented in 40 realizations of each. As mentioned earlier, three zones of interest were targeted in the SGS; those are, from bottom to top, the sandy fossiliferous packstone, burrowed wackestone, and stromatolite grainstone. As indicated in the lithofacies modeling, these three lithofacies were subdivided into three layers (for the sandy fossiliferous packstone), and two layers (for each of the burrowed wackestone and the stromatolite grainstone). This subdivision was motivated by the need of acquiring better vertical variability behavior, so, each of the measured sections contains seven readings of each of porosity and permeability. Three models have were; one for the porosity (Figure 5-28), and two for both of the raw permeability (Figure 5-29), and the log-transformed permeability (Figure 5-30).

**Variography of Property models**

Experimental semivariograms were constructed for the selected zones in the studied outcrop. These models were calibrated by theoretical models for best fitting, and the Gaussian model was selected as the best fit for both of the porosity and permeability semivariograms. These semivariogram were clearly affected by the number of data, and do not express clear theoretical variogram model neither for porosity, nor for permeability, particularly in vertical direction, and is associated with high nugget effect in most cases. However, an acceptable model representations were obtained, with honoring to the input data. Isotropy analysis showed geometry anisotropy attributed to the contrast between major and minor ranges (Figure 5-22 to 5-27).

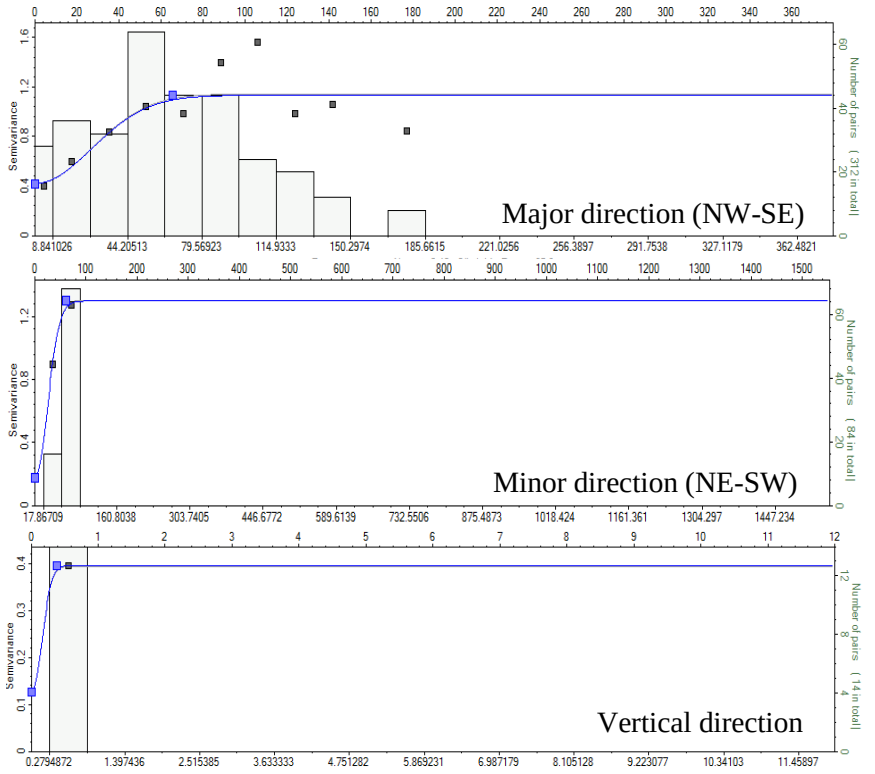


Figure 5-22: Porosity semivariograms of Zone-1

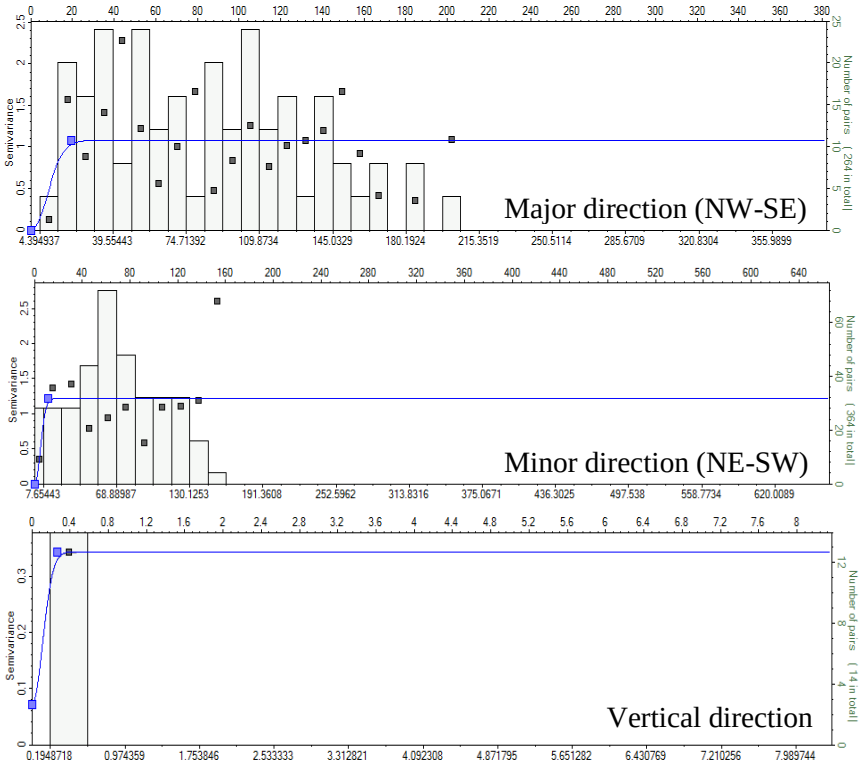


Figure 5-23: Porosity semivariograms of Zone-3

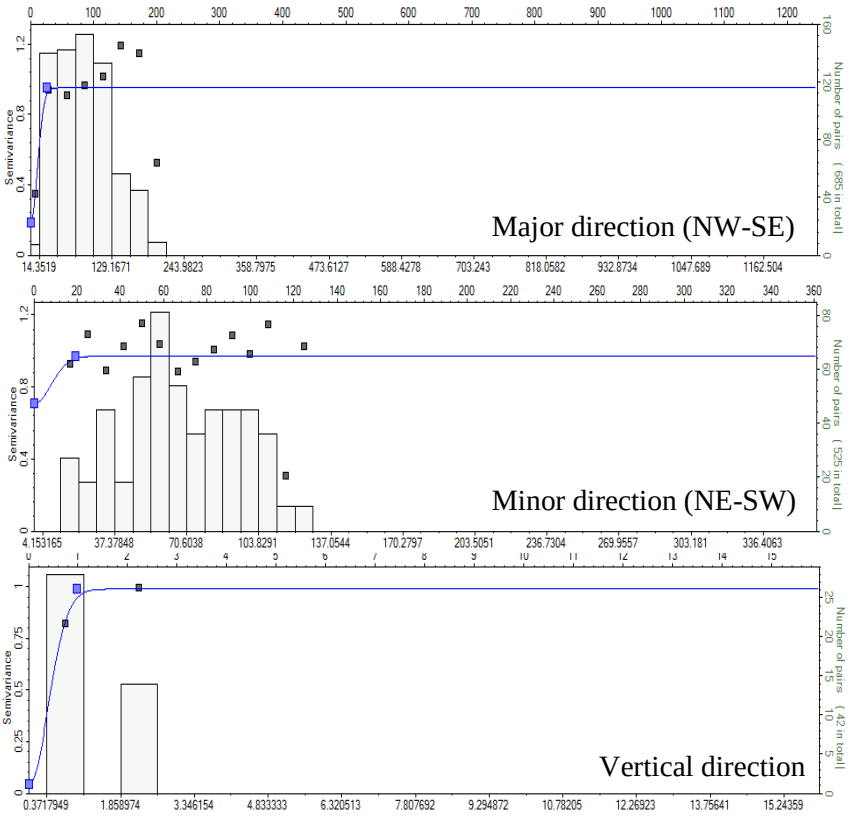


Figure 5-24: Porosity semivariograms of Zone-5

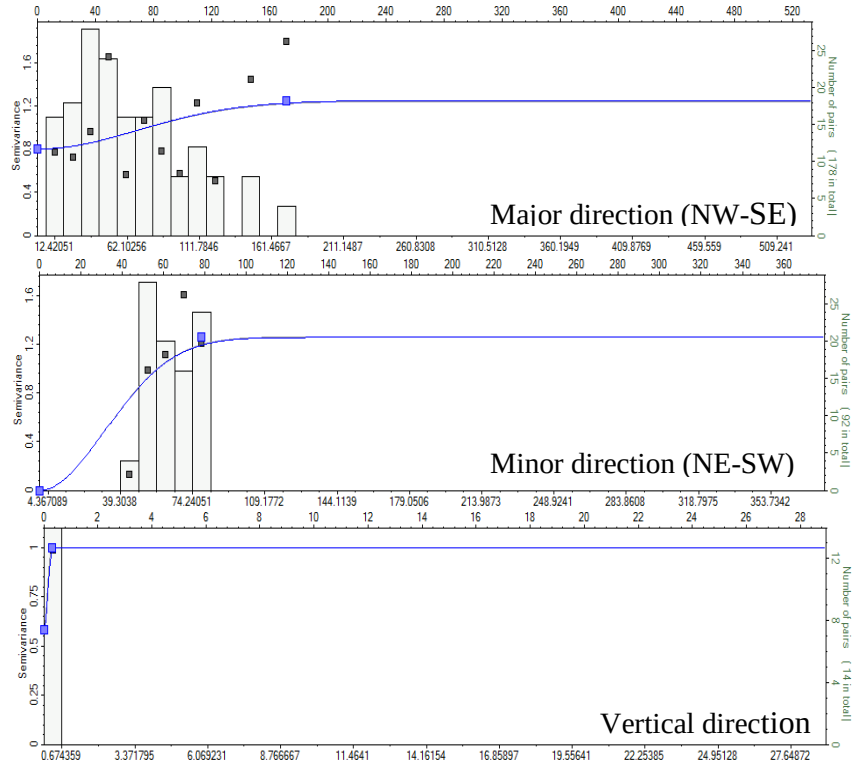


Figure 5-25: Permeability semivariograms of Zone-1

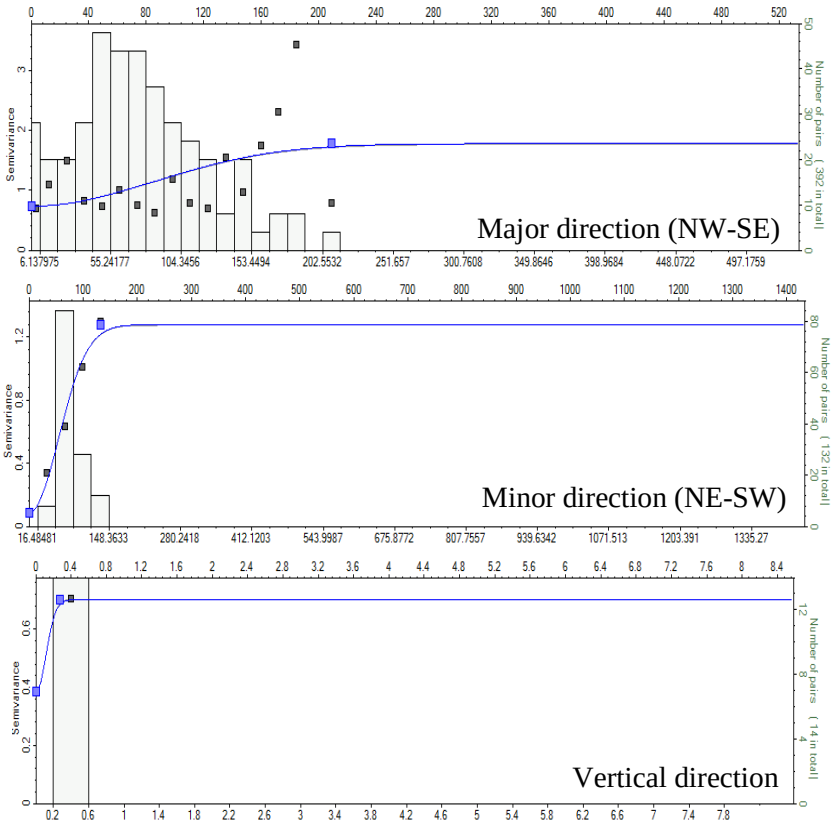


Figure 5-26: Permeability semivariograms of Zone-3

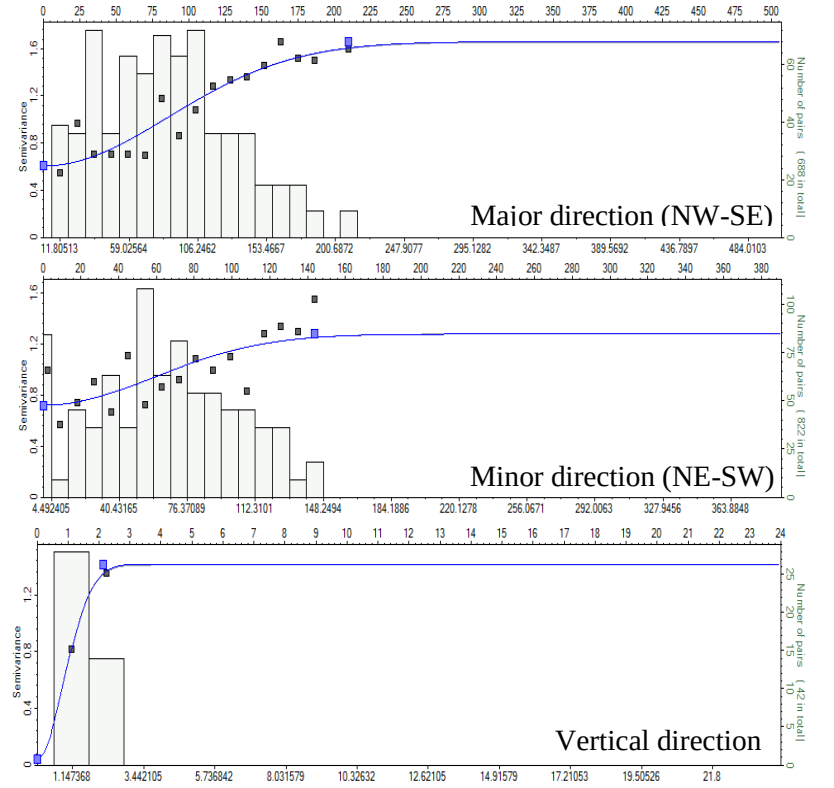


Figure 5-27: Permeability semivariograms of Zone-5

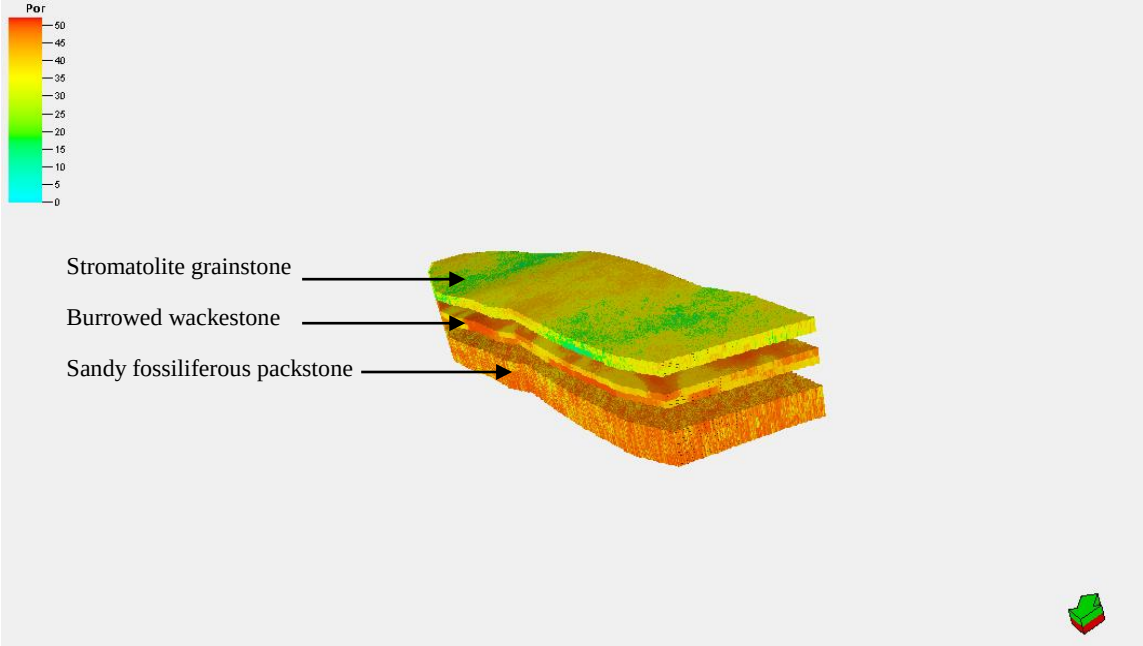


Figure 5-28: 3D view of porosity model of the three zones of interest in the studied outcrop

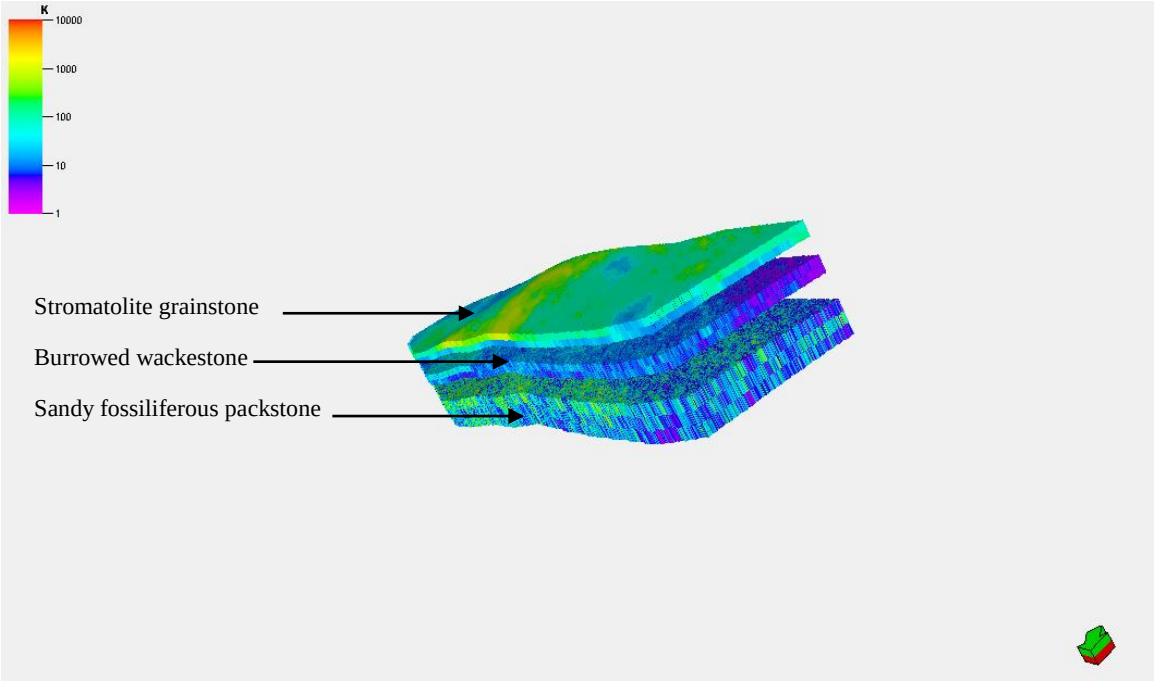


Figure 5-29: 3D view of raw permeability model of the three zones of interest in the studied outcrop

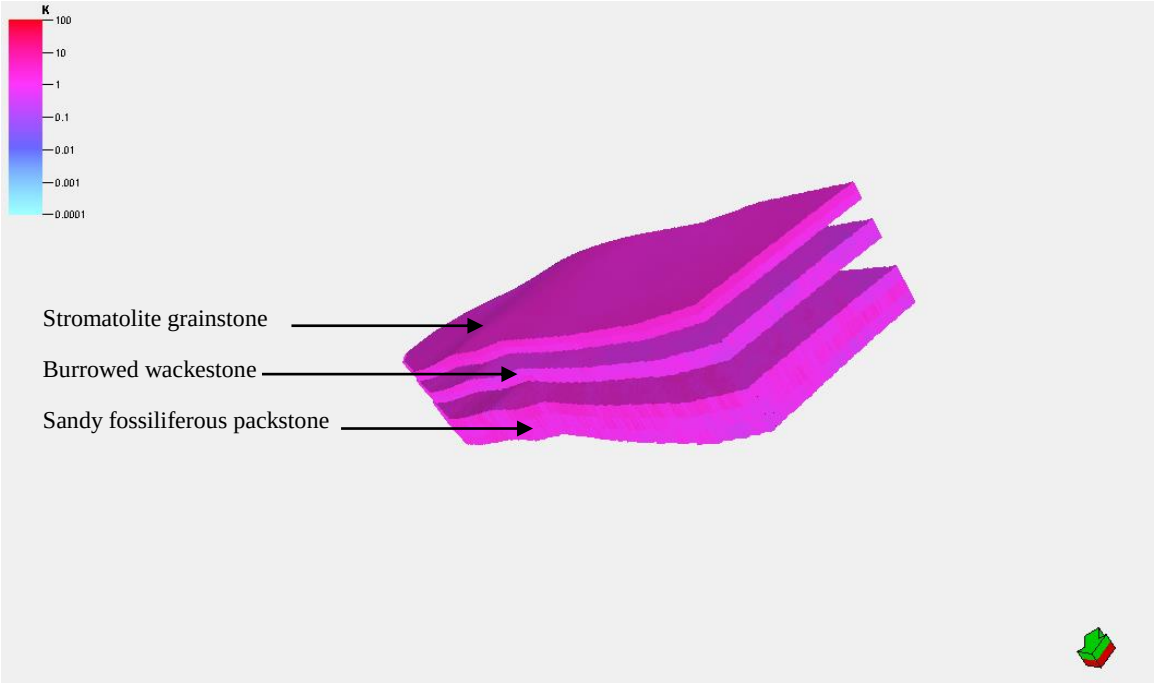


Figure 5-30: 3D view of log-transformed permeability model of the three zones of interest in the studied outcrop

**Validation of the 3D property Models**

The technique used for property model validation is similar to that used for the facies model. Qualitatively, A slice from each model was correlated to input data in the nearest measured section, to show whether the model had honored and respected the input data or not. The validation test illustrated that models of the porosity (Figure 5-28), raw permeability (Figure 5-29), and log transformed-permeability (Figure 5-30) respected their input data (Figure 5-31). In addition, the histograms of the property models revealed agreement to that of input datasets (Figure 5-32). The five top-ranked property models showed same distribution of input datasets (Figure 5-33).

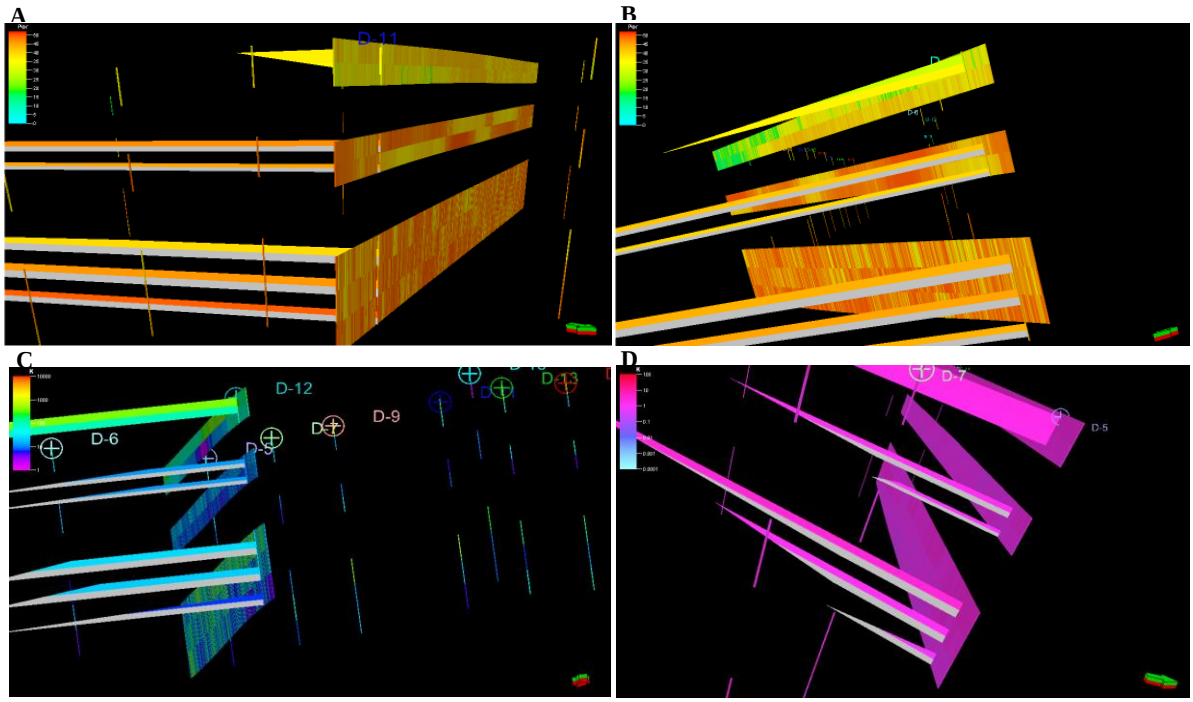


Figure 5-31: Qualitative validation of the property models by comparing the input data with models of porosity (A) and (B), raw permeability (C), and log transformed-permeability (D)

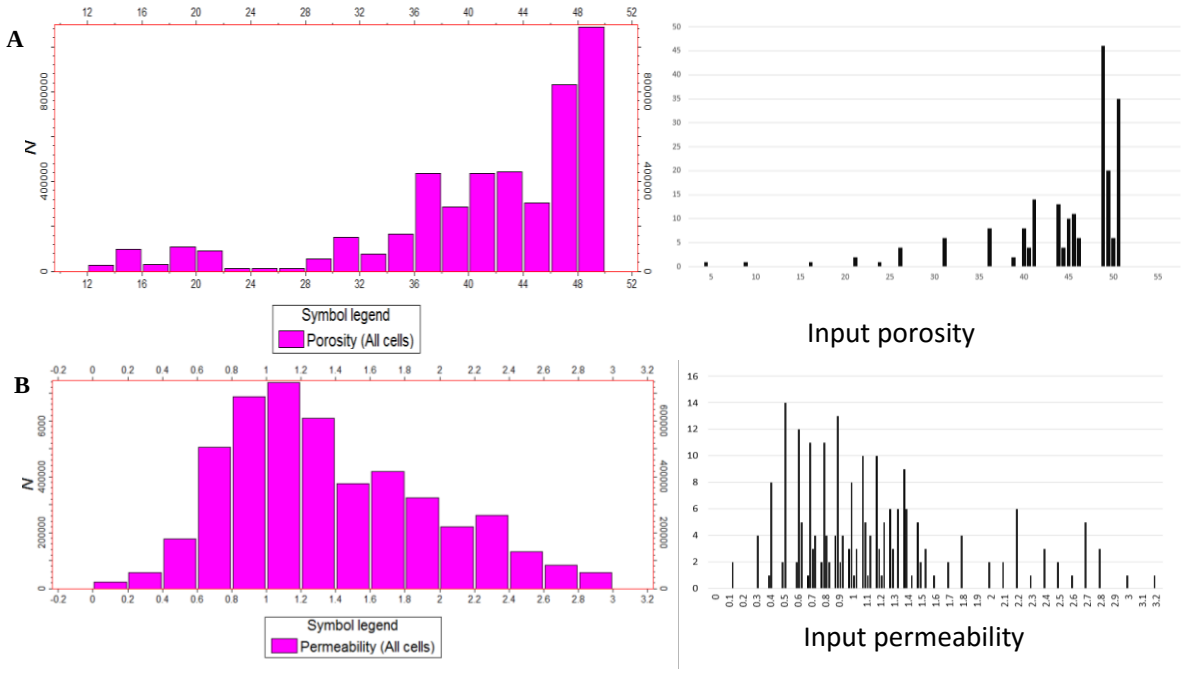


Figure 5-32: Histogram validation of the property models: A: histogram of porosity model, and B: histogram of log transformed-permeability model, compared with their input datasets

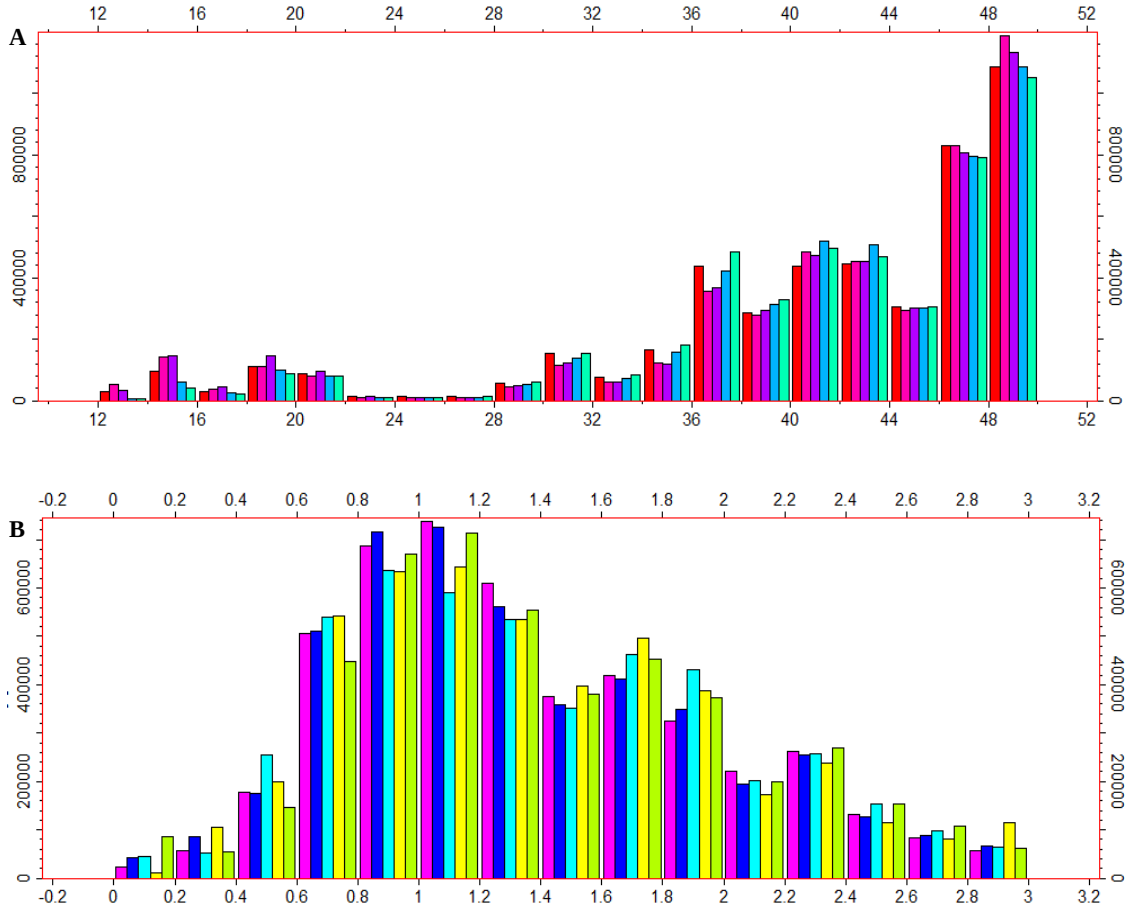


Figure 5-33: Validation of property realizations showing the top-five ranked realizations of the porosity (A), and log transformed-permeability (B) as indicated by different colors in each

## 5.6 Controls on Porosity and Permeability

Understanding of facies and property variation patterns is an important aspect for better quantitative and qualitative evaluation. However, it is more important to investigate the controls behind these variations in order to introduce at least a possible scenario of reservoir heterogeneity that might be applicable in similar setting. Dam Formation was deposited in tidally-influenced shallow marine environment, as indicated in literature and by different field and laboratory observations in the current study. This heterolithic environment led to the deposition of different lithofacies in relatively small thickness of sedimentary succession. As shown in the facies model, this spatial heterogeneity took place even within same unit. The property model was based on detailed investigations of three different lithofacies, which belong to different zones in shallow marine environment. This depositional contrast triggers variations in the lithofacies properties such as porosity and permeability. Beside the primary depositional porosity, the detailed petrographic inspection and SEM imaging showed that porosity enhancement is mainly caused by dissolution of lime mud and skeletal fragments, channel porosity (non-fabric selective), and leaching (Figure 5-34). In contrast, the porosity reduction factors include poor sorting, micrite filling, and rarely-occurred blocky calcite filling (Figure 5-34). On the other hand, permeability was also influenced more or less by same controls. The poor sorting besides the intensive random scattering of siliclastic grains such as quartz played an important role in the random distribution of permeability data set especially in the sandy fossiliferous packstone where quartz influx occurs intensively. In addition, the poor sorting of the skeletal grains surprisingly enhanced the permeability in upper part of

the sandy fossiliferous packstone. The burrowed wackestone is also affected by different siliciclastic influx and micritization. Regarding other lithofacies, no anomalous contrast were found except in some parts of the skeletal oolitic grainstone and stromatolite grainstone corresponding with zones of cross bedding, and the tangential surfaces of algal mats respectively, in contrary, the dis-connectivity of the fenestral and vuggy pores of the stromatolite grainstone may interpret its permeability reduction (Figure 5-34).

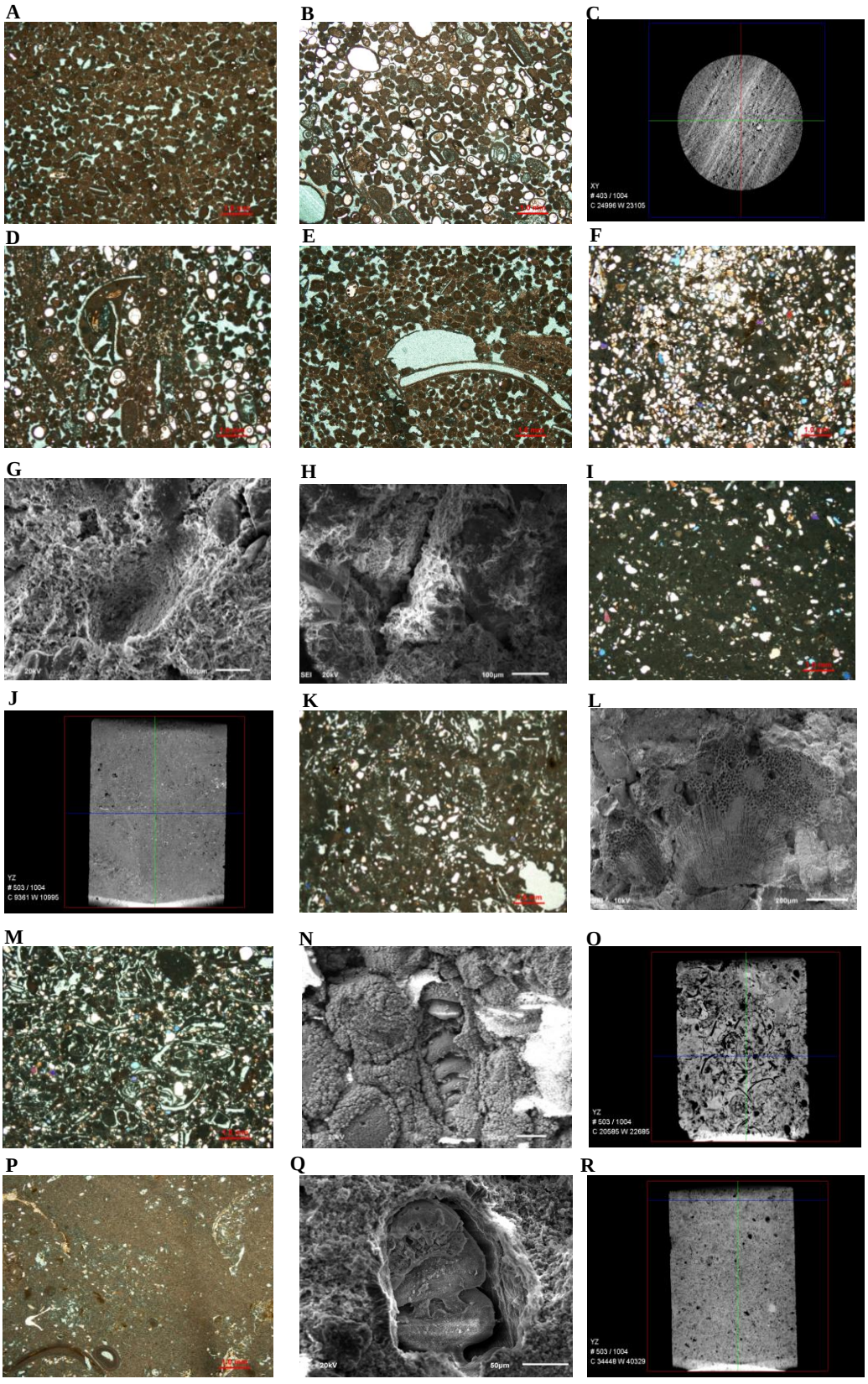
A
B
C
XY
# 403 / 1004
C 24996 W 23105
D
E
F
G
20kV
100µm
H
SEI 20kV
100µm
I
J
YZ
# 503 / 1004
C 9361 W 10995
K
L
10kV
200µm
M
N
O
YZ
# 503 / 1004
C 20585 W 22685
P
Q
20kV
50µm
R
YZ
# 503 / 1004
C 34448 W 40329

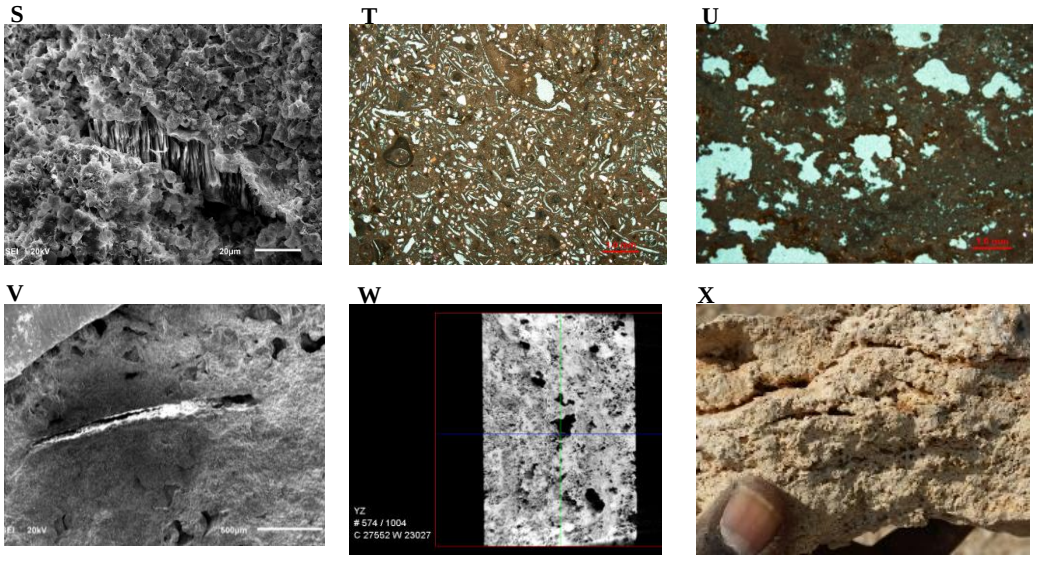


Figure 5-34: Controls on porosity and permeability shows different factors as indicated by field observations, petrography, SEM images, and Micro CT scan:

A, B, C, D, E: Skeletal oolitic grainstone showing intergranular, blocky calcite filling, permeability enhancement via bedding planes, moldic porosity

F, G, H, I, J: Lower sandy fossiliferous packstone showing wide range of siliciclastic influx and micritization which affect the petrophysical parameters, micritization affected even the packstone texture. Leaching porosity, channel porosity (non-fabric selective), and dispersed micro-vuggy porosity in the plug scale

K, L, M, N, O: Upper sandy fossiliferous packstone showing moldic porosity, leaching, intraskeletal porosity in uniserial forams and coral reef fragments, heterogeneous porosity in core plug scale

P, Q, R, S, T: Burrowed wackestone showing intensive micritization which affected the wackestone texture, abandoned porosity around Rotalid Sp., micro-vugs in core plug, mud infilling borrows might reduce the permeability

U, V, W, X: Domal stromatolite grainstone showing fenestral porosity, blocky calcite in a bivalve mold, inter-laminae pathways which might enhance the permeability

# CHAPTER 6

# CONCLUSION AND RECOMMENDATION

The Miocene Dam Formation was targeted to investigate the reservoir properties (porosity and permeability) within its lithofacies framework. The study was applied on one outcrop in Al-Nasbiyah Area in Eastern Saudi Arabia. The lithofacies Framework construction revealed a mixed siliciclastic-carbonate deposits with dominance of carbonate representation. Detailed lithofacies study resulted in 21 different lithofacies, including two sandstone lithofacies, quartz grains are sparse in most of carbonate lithofacies. The sedimentary structures, stacking patterns, and petrographic investigations of the lithofacies indicated that Dam Formation was deposited in a shallow marine tidal flat environment, enough saline water to allow the partial deposition of evaporite minerals associated with supra-tidal lithofacies especially in the top of the succession. The shallow marine setting of Miocene Dam Formation was also indicated by presence of different species of benthic foraminifera. The detailed petrophysical investigations targeted the porosity and permeability in four lithofacies in the studied outcrop. These lithofacies were selected on the basis of petrographic analysis, and the common carbonate reservoir textures in the literatures, besides the inapplicability of proper sampling plan for further geostatistical studies as a result of inadequate bed thickness, and the eolian and talus coverage. The selected lithofacies included, from bottom to top, skeletal oolitic grainstone, sandy fossiliferous packstone, burrowed wackestone, and stromatolite grainstone, at the top of the studied outcrop. According to the field and laboratory

observations of whole lithofacies, the visual porosity classification showed that Dam Formation is dominantly characterized by secondary porosity and less primary intergranular porosity. The dominant secondary porosity includes vuggy and leaching, intragranular and intraparticle, moldic, shelter, channel (non-fabric selective), and fenestral porosity. These results were also confirmed by SEM and Micro CT scanning. Detailed laboratory tests for porosity and permeability were conducted on plugs collected from the selected lithofacies. The cross-relationship between porosity and permeability showed poor relationships of all lithofacies due to poorly-sorted composition. Although the post-depositional processes have enhanced the porosity, the permeability is quite heterogeneous. This heterogeneity was detected in the univariate statistics, represented in poor histogram shapes and discordant descriptive statistics comparing to that of porosity datasets. However the log-normalization of permeability population showed better normal distribution. This study showed that 2D permeability relationships are fair to good for the selected lithofacies, which reflect fair to good charging properties. Geostatistical modeling represented the core of this study. 3D models were generated for lithofacies, porosity and permeability. As mentioned earlier, many reasons have banned applicability of detailed modeling and characterization of the whole succession of Miocene Dam Formation in the study area. Accordingly, the lithofacies model was conducted for the best three-dimensional exposure of the outcrop, the main outcrop body. Therefore, 10 lithofacies were modeled by indicator simulation for facies modeling. Among these lithofacies, porosity and permeability were modeled for only three lithofacies. 15 vertical measured sections were utilized to insure 3D modeling of the lithofacies around the exposure. The 3D lithofacies model revealed a little observable lateral and vertical

variability for the 40 produced realizations, however the most heterogeneity was observed in the cyclic mudstone-grainstone zone, since this zones contains larger number of layers. As a result of model ranking, five top-ranked realizations were selected, based on honoring test to the input data. Comparing the upscaled lithofacies to that of the input lithofacies showed good correlation, the matter that can validate the resulting models. In addition, the descriptive statistics of the lithofacies realizations, to high extent, matched the input lithofacies. 40 property models were generated for each of porosity and permeability datasets, the input data includes vertical measurements along 14 measured sections. The vertical sampling were arranged, from top to bottom, as following: 1- stromatolite grainstone (2 samples/section), 2- burrowed wackestone (2samples/sections), and 3- sandy fossiliferous packstone (3 samples/section). As expected, the variogram of property distribution showed poor shape in vertical direction. This can be a resultant of the few number of samples per each section, which was attributed to the thickness of selected lithofacies, in addition to other technical reasons about accessibility and sampling. However, the resulting 3D models exhibited accepted representations for facies properties, and honoring the input data in their locations. Same like lithofacies models, top-five ranked realizations were adopted on the basis of their honoring test to the input data. For further validation, the cross correlation of these realizations showed same distribution.

Finally, the following are recommended for future researches:

- Application of same research procedures, with higher-resolution sampling strategy, on other outcrops in the study area and other localities in Eastern Saudi

Arabia. This could offer a larger scale of heterogeneity in facies and reservoir quality and architecture.

- Detailed and regional lithofacies investigation can provide a basis of correlation between these deposits and subsurface Miocene reservoir in Eastern Arabian Peninsula, and Iran.
- In any future local or regional modeling, LiDAR is recommended for geometry model, since it can save time and effort in model construction.
- Further detailed petrophysical analyses for porosity and permeability can enhance the understanding of their relationships in such carbonate textures, and also may build a solid correlation that can be used for prediction purposes.
- Since siliciclastic composes an observable percentage in the study area, so, investigating the geochemistry and provenance of sandstone influx in Dam Formation is vital, besides its effect on reservoir quality.

## REFERENCES:


[1] Abu-Zeid, M., and Khalifa, H., 1983. Sedimentological and paleoenvironmental aspects of the Miocene succession in Jebel Nakhash, Qatar, Arabian Gulf. Neues Jahrbuch fur Geologie und Palaontologie Monatshefte, v. 7, p. 334-399.

[2] Adams J. E, Frenzel H. N., 1950. Capitan barrier reef, Texas and New Mexico. J Geol 58:289–312.

[3] Ahr, W. M., 2011. Geology of carbonate reservoirs: the identification, description and characterization of hydrocarbon reservoirs in carbonate rocks. John Wiley & Sons, pp. 120.

[4] Al-Enezi, S. S., 2006. Comparison of Recent and Miocene foraminifera from Eastern Saudi Arabia. Master of Science Thesis, King Fahd University of Petroleum and Minerals.

[5] Al-Husseini, M. I., 2000. Origin of the Arabian Plate Structures: Amar Collision and Najd Rift. GeoArabia, v. 5, no. 4, 527-542.

[6] Alkhaldi, F., 2009 (unpub.). Controls on Hierarchy of Miocene Buildups within a High Resolution Cycle Stratigraphic Framework of Dam Formation, Lidam Area, Saudi Arabia, Geology Master Thesis, KFUPM Main Library, KFUPM.

[7] Al-Khalifah, F. A., Abdullatif, O.M., and Makkawi, M. H. 2004. Sedimentology and geostatistical modeling of Quwarah Member, Qasim Formation: Paleozoic sandstone reservoir outcrop analog, Saudi Arabia. 6th Middle East Geosciences Conference, GEO 2004. GeoArabia, Abstract, v. 9, no. 1, p. 30.

[8] Alnazghah, M. H., Bádenas, B., Pomar L., Aurell M., Morsilli M., 2013. Facies heterogeneity at Interwell - scale in a carbonate ramp, Upper Jurassic, NE Spain, Marine and Petroleum Geology 44 (2013) 140 – 163.

[9] Amaefule, J. O., Altunbay, M., Tiab, D., Kersey, D. G., and Keelan, D. K., 1993. Enhanced reservoir description: using core and log data to identify hydraulic (flow) units and predict permeability in uncored intervals/wells. In SPE Annual Technical Conference and Exhibition. Society of Petroleum Engineers.

[10] Al-Saad, H., and Ibrahim M. I., 2002. Stratigraphy, micropalaeontology, and palaeoecologyof the Miocene Dam Formation, Qatar. GeoArabia, v. 7, no. 1, p. 9-28.

[11] Bellen, R. C., Van Dunnington, H. V., Wetzel, R., and Morton, D., 1959. Lexique Stratigraphiquw Internal Asie. Iraq. Intern Geol. Conger. Comm. Stratigr, 3, Fasc. 10a, 333p.

[12] Bohling, G. 2005. Introduction to Geostatistics and Variogram Analysis, C&PE 940, Kansas Geological Survey.

[13] Bohling, G., 2005. Kriging, C&PE 940, Kansas Geological Survey.

[14] Bohling, G., 2005. Stochastic Simulation and Reservoir Modeling Workflow, C&PE 940, Kansas Geological Survey.

[15] Borgomano, J., Masse J. P., Fenerci-Masse M., Fournier, F., 2013. Petrophysics of Lower Cretaceous Platform Carbonate Outcrops in Province (SE France): Implication for Carbonate Reservoir Characterization, Journal of Petroleum Geology, Vol. 36(1), January 2013, pp 5–42.

[16] Borgomano, J. R. F., Fornier, F., Viseur, S., and Rijkels, L., 2008. Stratigraphic well correlations for 3-D static modelling of carbonate reservoirs. AAPG Bull, 92 (6), 789-824.

[17] Busch, J. M., Fortney, W. G., and Berry, L. N., 1987. Determination of lithology from well-logs by statistical analysis: SPE Formation Evaluation, December 1987, p. 412-418.

[18] Cavelier, C. 1970. Geologic Description of the Qatar Peninsula (Arabian Gulf). Government of Qatar Publication, Department of Petroleum Affairs, p. 39.

[19] Clark, I., 2001. Practical Geostatistics Course Notes, Internet source: http://www.kriging.com/PG1979/PG1979.pdf

[20] Davis, J. C., 2002. Statistics and Data Analysis in Geology. 3rd edition, John Wiley and Sons, New York, USA.

[21] Davis Jr, R. A., and Dalrymple, R. W., 2011. Principles of tidal sedimentology. Springer Science & Business Media.

[22] Dercourt, J., Gaetanu, M, Vrielynk, B., Barrier, E., Biju-Duval, B., Brunet, M. –F, Cadet, J. P., Crasquin, S., Sandulescu, M., (Eds), 2000. Atlas Peri-Tethys. Palaeogeographical Maps CCGM / CGMW, Paris: 24 maps and explanatory notes: I–XX, 269 p.

[23] Dickson, J.A.D., 1966. Carbonate identification and genesis as revealed by staining. Journal of Sedimentary Petrology, 36, 491-505.

[24] Dixon W. J. and Massey F. J., 1951. Introduction to Statistical analysis, New York: McGraw-Hill.

[25] Dunham, R. J., 1962. Classification of carbonate rocks according to depositional texture. Memoir 1-American Association of Petroleum Geologists, 108-121.

[26] Eltom, H., Abdullatif, O., Makkawi, M., and Abdulraziq, A., 2014. Characterizing and modeling the Upper Jurassic Arab-D reservoir using outcrop data from Central Saudi Arabia. GeoArabia, 19, 53-84.

[27] Eltom, H., Makkawi, M., Abdullatif, O., and Alramadan, K., 2012. High-resolution facies and porosity models of the upper Jurassic Arab-D carbonate reservoir using an outcrop analogue, central Saudi Arabia, Arab J Geosci DOI 10.1007/s12517-012-0708-1, Springer, Saudi Society for Geosciences.

[28] Felletti F., 2004. Statistical modelling and validation of correlation in turbidites: an example from the Tertiary Piedmont Basin (Castagnola Fm., Northern Italy). Marine and Petroleum Geology 21 (2004) 23–39.

[29] Flugel, E., 2010. Microfacies of Carbonate Rocks: Analysis, Interpretation, and Application. 2nd Edition, 2010 (with a contribution by Axel Munnecke), Springer-Verlag Berlin Heidelberg.
[30] Frykman, P., 2001. Spatial Variability in Petrophysical properties in Upper Maastrichtian Chalk Outcrop at Steven Klint, Denmark, Marine and Petroleum Geology 18(2001) 1041-1062.
[31] Goovaerts, P. 1997. Geostatistics for Natural Resources Evaluation. Applied Geostatistics Series. xiv + 483 pp. New York, Oxford: Oxford University Press.
[32] Harris, P.M., 2010. Delineating and quantifying depositional facies patterns in carbonate reservoirs: insight from modern analogs. AAPG Bulletin 94, p. 61-86
[33] Haq and Alqahtani, 2005. Phanerozoic cycles of Sea Level Change on the Arabian Platform, Jurassic-Neogene Arabian Platform Cycle Chart, Geoarabia, Vol. 10, No. 2, 127-160.
[34] Hewaidy, A., 1991. Contribution to the stratigraphy of Miocene sediments in Qatar. Middle East Research Center, Ain Shams University, Egypt, Earth Science Series, v. 5, p. 160-170.
[35] http://www.coretest.com/
[36] Irtem, O., 1986. Miocene Tidal Flat Stromatolites of the Dam Formation, Saudi Arabia, Arabian Journal of Science and Engineering, v. 12, no. 2, p.145 - 153.
[37] Isaaks, E. H., and Srivastava, R. M., 1989. An Introduction to Applied Geostatistics, Oxford University Press Inc., New York, USA.
[38] Jassim S. Z., and Goff, J. C., 2006, Geology of Iraq, Dolin Publishing, Prague and Moravian Museum, Brno, Czech Republic, First Edition, 2006.
[39] Jennings Jr. J. W., Ruppel S. C., and Ward W. B., 2000. Data and Modeling of Fluid-Flow Effects in Carbonate Outcrops, SPE Reservoir Eval. & Eng. 3 (4), pp. 292-303.
[40] Jensen, J. L., Hinkley, D. V., and Lake, L. W., 1987. A statistical study of reservoir permeability: distributions, correlations, and averages: SPE Formation Evaluation, December 1987, p. 461-468.
[41] Jensen, J. L., Lake L W., Corbett P. W. M., and Goggin D. J., 1997. Statistics for petroleum engineers and geoscientists (Vol. 2). Gulf Professional Publishing, p. 76.
[42] Kendall C. G. and Warren J., 1987. A review of the origin and setting of tepees and their associated fabrics. Sedimentology 34:1007–1027.
[43] Khalifa, H., and Mahmoud M., 1993. New occurrence of algal stromatolites and benthonic foraminifera from the Miocene of Al-Nikhsh area, southwest Qatar Peninsula: implication on their palaeoenvironmental meaning. Arabian Gulf Journal of Science Research, v. 11, no. 3, p. 325–338.
[44] Koehrer, B. S., Heymann, C., Prousa, F., Aigner, T., 2010. Multiple-scale facies and reservoir quality variations within a dolomite body – Outcrop analog study

from the Middle Triassic, SW German Basin, Marine and Petroleum Geology 27 (2010) 386–411.

[45] Konert, G., Afifi, A.M., Al-Hajri, S.A., and Droste, H.J. 2001. Paleozoic Stratigraphy and Hydrocarbon Habitat of the Arabian Plate. GeoArabia, v. 6, no. 3, p. 407-442.

[46] Koop, W. J., and Stoneley, R., 1982. Subsidence history of the Middle East Zagros Basin, Permian to Recent. Philosophical Transactions of the Royal Society, London, Series A, v. 305, p. 149–168.

[47] Krumbein, W. C., and Pettijhon, F. J., 1961. Manual of Sedimentary Petrology: New York, Appleton-Century-Crofts, 549 p.

[48] Labourdette, R., Crumeyrolle, P., Remacha, E., 2008. Characterisation of dynamic flow patterns in turbidite reservoirs using 3D outcrop analogues: example of the Eocene Morillo turbidite system, south-central Pyrenees, Spain, Mar Pet Geol 25:255–270.

[49] Leonide, P., Borgomano, J., Masse, J- P., and Double, T. S., 2012. Relation between stratigraphic architecture and multi-scale heterogeneities in carbonate platforms: The Barremian–lower Aptian of the Monts de Vaucluse, SE France, Sedimentary Geology 265 (2012) 87–109.

[50] Lindsay, R.F. and Hughes, G.W., 2010. Saudi Arabian Jurassic outcrop Reservoir equivalents. A Pictorial Review. The Oil Drop V 22, issue 02, P. 6 -11.

[51] Ling, H. E., Lun, Z. H. A. O., Jianxing, L. I., Ji, M. A., Ruilin, L. U. I., Shuqin, W. A. N. G., and Wenqi, Z. H. A. O., 2014. Complex relationship between porosity and permeability of carbonate reservoirs and its controlling factors: A case study of platform facies in Pre-Caspian Basin. Petroleum Exploration and Development, 41(2), 225-234.

[52] Lucia, F. J., 1999. Carbonate reservoir characterization: an integrated approach. Springer Science & Business Media, 1-27.

[53] Masse, J.-P., 1995. Lower Cretaceous biostratigraphy of southern France. A reference for Mesogean correlations. Revista Mexicana de Ciencias Geológicas, 12, 236-256.

[54] Matheron, G., 1967. Kriging or Polynomial Interpolation Procedures? CIMM Transactions, 70, pp 240-244.

[55] Mazzullo S. J. and Chilingarian G. V., 1992. Diagenesis and origin of porosity. Developments in Petroleum Sciense, 30, 199-270.

[56] Meyer, F. O., Price R. C., Al-Ghamdi I. A., Al-Goba I. M, Al-Raimi S. M., Cole J. C., 1996. Sequential stratigraphy of outcropping strata equivalent to Arab-D reservoir, Wadi Nisah, Saudi Arabia. GeoArabia 1:435–456.

[57] Misra, D., Schatzinger R. A., Cil M., Wheeler J. R., and Jill Fite M., 1998. An Assessment of Lateral Variability of Geological Parameters Using Modal and Geostatistical Analysis of Outcrop Analoug, Society of Petroleum Engineers (SPE

49280), Annual Technical Conference and Exhibition, New Orleans, Louisiana, 27-30 Sep. 1998.

[58] Moore C. H., 2001. Carbonate Reservoirs, Porosity Evolution and Diagenesis in a Sequence Stratigraphic framework. Developments in Sedimentology, 55, Elsevier, Amsterdam.

[59] Mylroie J. E. and Carew J. L., 2003. Karst development on carbonate islands, Speleogenesis and Evolution of Karst Aquifers, 1, 21

[60] Palermo, D., Aigner, T., Nardon, S., Blendinger, W., 2010. Three-dimensional facies modeling of carbonate sand bodies: outcrop analog study in an epicontinental basin (Triassic, southwest Germany). AAPG Bulletin 94, 475 - 512.

[61] Powers, R. W., Ramirez, L. F., Redmond, C. D., and Elberg, E. L. Jr., 1966. Geology of the Arabian Peninsula - Sedimentary Geology of Saudi Arabia. US Geological Survey Professional Paper, v. 560- D, Washington, DC.

[62] Pratt BR., 2002. Tepees in peritidal carbonates: origin via earthquake- induced deformation, with example from the Middle Cambrian of western Canada. Sed. Geol 153:57–64.

[63] Prazak, J., 1974. Stratigraphy and paleontology of the Miocene of Western Desert, W. Iraq. Manuscript report, GEOSURV, Baghdad.

[64] Reineck H. E., and Singh I. B., 1980. Depositional sedimentary environments, 2nd edn. Springer, New York, 551p.

[65] Sahin A., Ghori, S. G., Ali, A. Z., El-Sahn, H. F., Hassan, H. M., and Al-Sanounah, A., 1998. Geological Controls of Variograms in a Complex Carbonate Reservoir, Eastern Province, Saudi Arabia, Mathematical Geology, Vol. 30, No. 3, 309-322.

[66] Saner, S., and Sahin, A., 1999. Lithology and zonal porosity-permeability the Arab-D reservoir, Uthmaniyah field, Saudi Arabia: AAPG Bull., vol. 83, no. 2, p. 230-243.

[67] Sarma D. D., 2009. Geostatistics with Application in Earth Sciences, Second Edition, Springer, Capital Publishing Company, 2009, p. 81.

[68] Steineke, M., and Koch, T. W., 1935. Geological Reconnaissance of the Coastal Plain of Hasa Province, Northeastern Saudi Arabia. Arabian Oil Company, Dhahran, Saudi Arabia (unpublished).

[69] Senger R. K., Kerans C., Ferris M., and Fogg G. E., 1992. Geostatistical/Geological Permeability Characterization of Carbonate Ramp Deposits in Sand Andres Outcrop, Algerita Escarpment, New Mexico. SPE 23967. Permian Basin Oil and Gas Recovery Conference, Midland, Texas, March 18-20, 1992.

[70] Shinn, E. A., 1983. Tidal flat environment. In Carbonate depositional environments. Vol. 33, pp. 171-210.

[71] Shinn, 1968b, Practical significance of birds eye structures in carbonate rocks: Jour. Sed. Petrology. v. 38, no. 1, p. 215-223.

[72] Tayyib M. A., 2007 (unpub.). Depositional Setting Impact on the Portland Cement Production Quality of the Dam Formation, Saudi Arabia, Geology Master Thesis, KFUPM.

[73] Thralls, W. H., & Hasson, R. C., 1956. Geology and oil resources of eastern Saudi Arabia. In Intern. Geol. Cong. 20th, Mexico. Symposium sobre Yacimentos de Petroleoy Gas (Vol. 2, pp. 9-32).

[74] Tiab, D., and Donaldson, E. C., 2004. Petrophysics: Theory and Practice of Measuring Reservoir Rock and Fluid Transport Properties, second edition with a new material, Elsevier, Gulf Professional Publishing, 2004.

[75] Tleel, J. W., 1973. Surface geology of Dammam Dome, Eastern Province, Saudi Arabia. Bulletin of American Association of Petroleum Geologists, v. 57, no. 3, p. 558-576.

[76] Torsæter, O., and Abtahi, M., 2000. Experimental Reservoir Engineering Laboratory Work Book, Department of Petroleum Engineering, Norwegian University of Science and Technology and Applied Geophysics.

[77] Warrlich, G., Bosence, D., Waltham, D., Wood, C., 2008. 3D stratigraphic forward modelling for analysis and prediction of carbonate platform stratigraphies in exploration and production. Marine and Petroleum Geology 25, 35 - 58.

[78] Ye Zhang, Y., 2011. Introduction to Geostatistics, Course Notes, Department of Geology & Geophysics, University of Wyoming, draft date January 12, 2011.

[79] Ziegler, M. A., 200konert1. Late Permian to Holocene Paleofacies Evolution of the Arabian Plate and its Hydrocarbon Occurrences. GeoArabia. V. 6, p. 445-504.

# VITAE

Abdallah Abdelkarim Hassan Abdelkarim
Bachelor degree in Geology, University of Khartoum, 2008
Master degree in Geology, KFUPM, 2015
Address: Dhahran, Saudi Arabia / Khartoum, Sudan

Email*: abdalla_haji@yahoo.com*

Professional Participation:

- Participated in the 10th International Conference of Saudi Society for Geosciences, Dhahran, Saudi Arabia, 2013, and Geo 2014, Manama, Bahrain.
- Conference presentation in the 11th International Conference of Saudi Society for Geosciences, Riyadh, Saudi Arabia, May 2015.
- Conference poster presentation in the 77th EAGE Conference and Exhibition, Madrid, Spain, June 2015.